Acoustic Analysis in Small-scale Rotating Detonation Engines

Hannah Shipman

A thesis
submitted in partial fulfillment of the
requirements for the degree of

Masters of Science in Aeronautics and Astronautics

University of Washington
2025

Committee:
Carl Knowlen
Robert Bridenthal

Program Authorized to Offer Degree:
Department of Aeronautics and Astronautics

University of Washington

Abstract

Acoustic Analysis in Small-scale Rotating Detonation Engines

Hannah Shipman

Chair of the Supervisory Committee:
Carl Knowlen
Department of Aeronautics and Astronautics

Rotating detonation engines (RDEs) have been at the forefront of cutting-edge research for the last few decades due to their potentially high thrust-to-weight ratio, compact size and ease of manufacturability. RDEs are typically annular designs in which a detonation wave spins around a cylindrical annular region. However, recent research shows that coreless RDEs, an innovative design with the inside core removed, hold promise for small-scale RDEs in particular.

In this work acoustic analysis is carried out on two sizes of smale-scale RDEs, of 10 mm and 25 mm outer diameter, in both hollow and annular configurations. The resulting operating modes and frequencies are compared with recent experimental data obtained using both H_2-O_2 and CH_4-O_2 gaseous propellant mixtures. Additionally, as-yet-unpublished data for the 10 mm configuration with heated propellant is analyzed and reported, and recommendations for prospective work to further establish the acoustic modes and mechanisms of RDEs are given.

Contents

§1.1 Copyright page 2

§1.2 Abstract 3

§1.3 Dedication 7

§1.4 List of Figures 8

§1.5 List of Tables 12

§1.6 Nomenclature 13

2 Introduction **15**

§2.1 Introduction to Coreless RDEs 15

§2.1.1 RDE Naming Conventions 17

§2.1.2 Annular RDE Design 18

§2.1.3 Coreless RDE Design 19

§2.2 Literature Review 20

§2.2.1 Prior research: UW RDE work 26

3 Methods **29**

§3.1 Description of UW Rotating Detonation Engine Laboratory 30

§3.1.1 Experimentation Run Sequence 35

§3.1.2 10 mm RDE Description 35

§3.1.3 25 mm RDE Description 39

§3.2 Physics of Detonation and Acoustics in RDEs 42

§3.2.1 Physics of Detonation Waves in RDEs 42

§3.2.2 Acoustic Modes in RDEs 49

§3.3 Initial Experimentation 58

4 Results 61

§4.1 Acoustic Analysis in Hollow RDEs 62

§4.1.1 Frequency Determination 62

§4.1.2 Temperature Determination 63

§4.1.3 Pressure and Additional Variables 67

§4.1.4 10 mm RDE: H_2 Frequency Results and Discussion 69

§4.1.5 10 mm RDE: CH_4 Frequency Results and Discussion 80

§4.1.6 25 mm RDE: CH_4 Frequency Results and Discussion 89

§4.1.7 Temperature Comparison Across Hollow RDE Cases 95

§4.2 Acoustic Analysis in Annular RDEs 104

§4.2.1 10 mm RDE: 2 mm Gap 105

§4.2.2 25 mm: 3 mm Gap 106

§4.2.3 25 mm: 5 mm Gap 108

§4.2.4 25 mm: 7 mm Gap 110

§4.2.5 Discussion of Annular Mode Results 111

5 Overview and Conclusion 115

§5.1 Summary of Findings 116

§5.2 Discussion of Findings 118

§5.3 Recommendations for Future Research 120

§5.4 Conclusion 124

Bibliography **125**

§1.3 Dedication

The author thanks her department, her colleagues in the University of Washington Graduate and Professional Student Senate (GPSS), and her fellow graduate students for their support.

The author also thanks her family and friends (you know who you are!) for their unconditional rallying together in support of the author's undertaking of this career milestone.

Special mentions: Carl Knowlen, for his mentorship; Stanzin, for your constancy, comforts, and also all the cooking; and Shuba Murthy, for proving that separation is no obstacle to achieving our dreams together.

§1.4 List of Figures

1. Annular RDE detonation wave sketch .... Fig. 2.1
2. Pressure contours in a hollow RDE .... Fig. 2.2
3. UW RDE experimental test facility .... Fig. 3.1
4. Laboratory control system and flow handling .... Fig. 3.2
5. Propellant flow handling diagram .... Fig. 3.3
6. Pre-detonator flow handling and control system .... Fig. 3.4
7. Details of the 10 and 25 mm RDEs .... Fig. 3.5
8. 10 mm injector face .... Fig. 3.6
9. 10 mm plenum details .... Fig. 3.7
10. 10 mm fuel and oxidizer injection system .... Fig. 3.8
11. Exploded view of the 10 mm RDE design details .... Fig. 3.9
12. 25 mm injector face .... Fig. 3.10
13. 25 mm plenum details .... Fig. 3.11
14. Exploded view of the 25 mm RDE design details .... Fig. 3.12
15. 25 mm experiment operation pictures .... Fig. 3.13
16. 25 mm experiment operation with annular gap of 3 mm .... Fig. ??
17. 25 mm experiment operation with annular gap of 5 mm .... Fig. ??
18. 25 mm experiment operation with annular gap of 7 mm .... Fig. ??

19. PGC, Brayton, Humphrey cycle .... Fig. 3.14

20. ZND model diagram .... Fig. 3.15

21. Pressure vs. volume diagram .... Fig. 3.16

22. Transverse modes pressure contours .... Fig. 3.17

23. Transverse modes pressure and velocity contours .... Fig. 3.18

24. Hollow 10 mm H_2-O_2, a_{CJ} and D_{CJ} vs. experimental data .... Fig. 4.1

25. 10 mm H_2-O_2, ϕ vs. spin speed .... Fig. 4.2

26. 10 mm H_2-O_2, trend line of experimental data vs. predicted 1T, 1R mode Fig. 4.3

27. 10 mm H_2-O_2, data vs. transverse frequencies .... Fig. 4.4

28. Run 53 Spectrogram .... Fig. 4.5

29. Run 53 Power spikes .... Fig. 4.6

30. Run 55 Spectrogram .... Fig. 4.7

31. Run 55 Power spikes .... Fig. 4.8

32. Run 60 Spectrogram .... Fig. 4.9

33. Run 60 Power spikes .... Fig. 4.10

34. 10 mm CH_4-O_2, a_{CJ} at $p = 3$ bar .... Fig. 4.11

35. 10 mm CH_4-O_2, trend line of experimental data vs. predicted 1T, 1R modes .. Fig. 4.12

36. 10 mm CH_4-O_2, data vs. transverse frequencies .... Fig. 4.13

37. Run 22 Spectrogram . . . . Fig. 4.14

38. Run 22 Power spikes . . . . Fig. 4.15

39. Run 59 Spectrogram . . . . Fig. 4.16

40. Run 59 Power spikes . . . . Fig. 4.17

41. Run 144 Spectrogram . . . . Fig. 4.18

42. Run 144 Power spikes . . . . Fig. 4.19

43. 25 mm CH_4-O_2, data vs. transverse frequencies with heated fuel data . . . Fig. 4.20

44. 10 mm CH_4-O_2, spin speed with normalized D_{CJ} . . . . Fig. 4.21

45. 10 mm CH_4-O_2, spin speed . . . . Fig. 4.22

46. 25 mm CH_4-O_2, experimental data vs. predicted 1T, 1R modes . . . . Fig. 4.23

47. 25 mm CH_4-O_2, data vs. transverse frequencies . . . . Fig. 4.24

48. 10 mm H_2-O_2, temperature sweep ($T = 300$ K) . . . . Fig. 4.25

49. 10 mm H_2-O_2, temperature sweep ($T = 500$ K) . . . . Fig. 4.26

50. 10 mm H_2-O_2, temperature sweep ($T = 800$ K) . . . . Fig. 4.27

51. 10 mm H_2-O_2, temperature sweep ($T = 1200$ K) . . . . Fig. 4.28

52. 10 mm H_2-O_2, temperature sweep ($T = 1400$ K) . . . . Fig. 4.29

53. 10 mm H_2-O_2, temperature sweep ($T = 1000$ K) with a_{CJ} . . . . Fig. 4.30

54. 10 mm H_2-O_2, temperature sweep across constant $\phi = 1.15$ . . . . Fig. 4.31

55. 10 mm CH_4-O_2, temperature sweep ($T = 300$ K) . . . . Fig. 4.32

56. 10 mm CH_4-O_2, temperature sweep ($T = 500$ K) .... Fig. 4.33

57. 10 mm CH_4-O_2, temperature sweep ($T = 800$ K) .... Fig. 4.34

58. 10 mm CH_4-O_2, temperature sweep ($T = 1200$ K) .... Fig. 4.35

59. 10 mm CH_4-O_2, temperature sweep across constant $\phi = 1.15$ .... Fig. 4.36

60. 25 mm CH_4-O_2, temperature sweep ($T = 300$ K) .... Fig. 4.37

61. 25 mm CH_4-O_2, temperature sweep ($T = 500$ K) .... Fig. 4.38

62. 25 mm CH_4-O_2, temperature sweep ($T = 800$ K) .... Fig. 4.39

63. 25 mm CH_4-O_2, temperature sweep ($T = 1200$ K) .... Fig. 4.40

64. 25 mm CH_4-O_2, temperature sweep across constant $\phi = 1.15$ .... Fig. 4.41

65. 10 mm annular RDE, H_2-O_2, with gap size 2 mm, transverse modes ..... Fig. 4.42

66. 10 mm annular RDE, CH_4-O_2, with gap size 2 mm, transverse modes ... Fig. 4.43

67. 25 mm annular RDE with gap size 3 mm, experiment vs. transverse modes Fig. 4.44

68. 25 mm annular RDE with gap size 3 mm, counter-rotating waves .... Fig. 4.45

69. 25 mm annular RDE with gap size 5 mm, experiment vs. transverse modes Fig. 4.46

70. 25 mm annular RDE with gap size 5 mm, counter-rotating waves .... Fig. 4.47

71. 25 mm annular RDE with gap size 5 mm, experiment vs. transverse modes with mass flux values .... Fig. 4.48

72. 25 mm annular RDE with gap size 7 mm, experiment vs. transverse modes Fig. 4.49

73. 25 mm annular RDE, comparison across gap sizes, select transverse modes Fig. 4.53

74. 25 mm annular RDE with gap size 3 mm, all transverse modes ....Fig. 4.50

75. 25 mm annular RDE with gap size 5 mm, all transverse modes ....Fig. 4.51

76. 25 mm annular RDE with gap size 7 mm, all transverse modes ....Fig. 4.52

§1.5 List of Tables

1. Table 3.1: Combustor port locations in the 10 mm RDE
2. Table 3.2: Combustor port locations in the 25 mm RDE
3. Table 3.3: Gap widths in the 25 mm annular RDE
4. Table 3.4: Fuels used per RDE size and configuration
5. Table 4.1: Stand-off distances per RDE configuration
6. Table 4.2: Percent difference between CEA and REFPROP reactant sound speeds
7. Table 4.3: Bessel function roots used in calculations for hollow RDEs
8. Table 4.4: Example frequency results at $\phi = 0.8$ in the 10 mm hollow RDE on H_2-O_2
9. Table 4.5: Example frequency results at $\phi = 1.15$ in the 10 mm hollow RDE on H_2-O_2
10. Table 4.6: Example frequency results at $\phi = 1.8$ in the 10 mm hollow RDE on H_2-O_2
11. Table 4.8: Example frequency results at $\phi = 0.8$ in the 10 mm hollow RDE on CH_4-O_2
12. Table 4.7: Multiples of the 1R frequency in the 10 mm hollow RDE on H_2-O_2

13. Table 4.9: Example frequency results at $\phi = 1.15$ in the 10 mm hollow RDE on CH_4-O_2
14. Table 4.10: Example frequency results at $\phi = 1.8$ in the 10 mm hollow RDE on CH_4-O_2
15. Table 4.11: Multiples of the 1R frequency in the 10 mm hollow RDE on CH_4-O_2
16. Table 4.12: Example frequency results at $\phi = 0.8$ in the 25 mm hollow RDE on CH_4-O_2
17. Table 4.13: Example frequency results at $\phi = 1.15$ in the 25 mm hollow RDE on CH_4-O_2
18. Table 4.14: Example frequency results at $\phi = 1.8$ in the 25 mm hollow RDE on CH_4-O_2
19. Table 4.15: Multiples of the 1R frequency in the 25 mm hollow RDE on CH_4-O_2

§1.6 Nomenclature

a	Sound speed (reactant)
a_{CJ}	Sound speed (product) in the Chapman-Jouguet detonation model
c_p	Specific heat at constant pressure
c_v	Specific heat at constant volume
D_{CJ}	Detonation speed in the Chapman-Jouguet detonation model
f, f_{mnq}	Frequency, dependent on the tangential, radial and longitudinal modes

– J_n	Bessel function of the first kind
– m	Radial mode number
– $\dot{m}$	Mass flow rate
– n	Tangential mode number
– p	Pressure within the RDE
– q	Longitudinal mode number
– Q, q'	Total heat addition, local heat addition
– S	Wave speed, generalized
– w	Wave count (experimentally determined; here $w = 1, 2, 3$)
– Y_n	Bessel function of the second kind
– α_{mn}	m^{th} root of $\frac{dJ_n}{dr} = 0$
– κ_{mn}	m^{th} root of $\frac{d}{dr}(J_n Y_n) = 0$; related to the Hankel functions
– γ	Heat capacity ratio: c_p/c_v
– λ	Wavelength
– ϕ	Fuel-to-oxidizer equivalence ratio
– Ψ	Mass flux

Chapter 2

Introduction

In this thesis we will cover the fundamentals of rotating detonation wave theory, a brief overview of RDE development (both annular and coreless), and the University of Washington test facilities and relevant previous work. We will carry out an acoustic analysis on both the 25 and 10 mm engine configurations. Next, we compare the performance results of coreless and annular configurations of 25 mm and 10 mm RDEs with multiple gap sizes. We will also compare 10 mm data with and without heated propellants along with the respective acoustic analyses. To conclude, we will discuss future research steps and provide recommendations for advancing the work of coreless RDE studies.

§2.1 Introduction to Coreless RDEs

Rotating Detonation Engines (RDEs) are a promising new technology. In contrast to the now-standard turbine-based rocket engine design, RDEs offer a simpler construction (including a lack of moving parts), a different thermodynamic cycle based on pressure gain combustion, and higher thermodynamic efficiency parameters such as a higher specific impulse. Applications include terrestrial power generation, stand-alone rocket engines and performance-boosting add-ons to new and existing rocket engine designs (e.g. the 2025

Pratt & Whitney/Raytheon/RTX design [1]). Another recent (2022-2023) test was carried out by NASA for potential use in future interstellar missions, designed with a 3D-printed copper alloy able to withstand the high heat transfer rates of the engine internals [2, 3, 4]. Additionally, JAXA in collaboration with several Japanese institutes including Nagoya University has successfully tested an RDE in actual vacuum and microgravity conditions (2022) [5].

Detonation-based engines have been studied for many years, and while so far they remain underdeveloped for practical applications, tests such as those cited above show a definitive increase in progress. Although detonation waves are more thermodynamically efficient at producing thrust from a given amount of fuel than the more commonly applied deflagration cycles, the inherently complex physics involved have hindered the development of practical applications of detonation-based thrusters such as RDEs. Gaining a better understanding of the transient wave behavior within RDEs allows for a expanded design possibilities to facilitate applying these engines in practical uses.

Acoustic analysis has implications for RDE performance, since it is as imperative to control the dominant frequency modes in RDEs as it is in turbine engines. However, many of the wide-band passive damping controls used in deflagration engines are unsuitable for use in RDEs, since passive damping is designed to eliminate all nonlinearities in engine frequency while RDEs rely on the nonlinear process of detonation to run [6]. Ensuring smooth flow along the upstream flow lines is one example of such controls that can be used in RDEs; this was the motivation for the “eigenfrequency analysis” (that is, acoustic frequency analysis akin to that described in Sec. §3.2.2) using COMSOL Multiphysics software completed by Pritschau et al.[6, 7]. In a similar vein, this study derives an analytical engine frequency formula which is carried out using MATLAB and plotted in

Excel to obtain predicted RDE operating modes with corresponding engine-level frequencies [8, 9].

§2.1.1 RDE Naming Conventions

Notation of RDEs varies widely in the literature, starting with the designation of “engine” (RDE) or “combustor” (RDC). Literature review shows that RDC studies tend to focus on parameters such as the detonation dynamics in the combustor itself, as opposed to RDE studies that examine thrust generated or flow fields aft of the combustor exit, usually in combination with nozzles of various types [10, 11]. Additionally, the acronym RDRE (where the second R stands for rocket) is used to specify that the engine propellant system is designed to be run from fuel and oxidizer tanks carried onboard a rocket, rather than only carrying the fuel as air-breathing RDEs do [12, 13].

The UW RDE test rig is more properly called an RDRE and/or RDC, because the research is focused on the combustor itself with no nozzle attachment (RDC) and because the experiment is run by injecting both fuel and oxidizer, as in a rocket engine application (RDRE). This argument notwithstanding, the acronym RDE has been chosen for use throughout this study for its generality and simplicity of use.

Additionally, the two configurations of RDEs referred to in this study have various naming conventions, including annular (cylindrical outer body with solid inner core inserted into the engine) and hollow or coreless (cylindrical outer body with no core, i.e. a cylindrical cavity). The latter are occasionally referred to as simply “cylindrical” (the counterpart to annular) or with the alternative distinction of center-bodiless (CBL) versus center-body (CB or annular) RDEs [14, 15]. Again for simplicity of notation, the terms annular and hollow will be primarily used in this work.

Finally, the small-scale RDEs studied in this thesis had combustor outer diameters of 10 mm and 25.4 mm. In this work, the two sizes are referred to as the 10 mm RDE and the 25 mm RDE, respectively, with the analysis results segregated by the sizing and the primary fuel type in the engine.

§2.1.2 Annular RDE Design

The combustion process in an RDE employs continuously spinning detonation waves within a cylindrical or annular combustion region. The older and more widespread design is the annular configuration, typically in the form of two concentric cylinders closed on one end, with the other end open to allow the exhaust to exit the engine. The inner cylinder is known as the core, and may be solid or internally-cooled. Also, the core may be either flat-ended or equipped with nozzles such as an aerospike nozzle, which offers atmospheric pressure compensation (for example, see Schwer and Johnson [16]). Typical operating propellants for RDEs are gaseous fuels, although liquid fuels including kerosene have also been successfully utilized [17]. Common fuels include hydrogen, methane and ethylene, with oxygen, air or nitrous oxide serving as the oxidizer.

The propellant is injected into the gap or hollow and a detonation wave is excited, which simultaneously compresses and heats the fuel to autoignition conditions. The combustion of the fuel then sustains the detonation as it rapidly progresses tangentially around the gap. In an annular RDE, fuel and oxidizer are injected into the annulus at impinging angles between $0° - 90°$ axial offset. For simplification, Fig. 2.1 shows a 0° offset, although non-zero offsets promote propellant mixing for higher performance characteristics. Here the rotating detonation wave is clearly visible with the leading shock, combustion region (induction and reaction zones), fill region of injected unburned

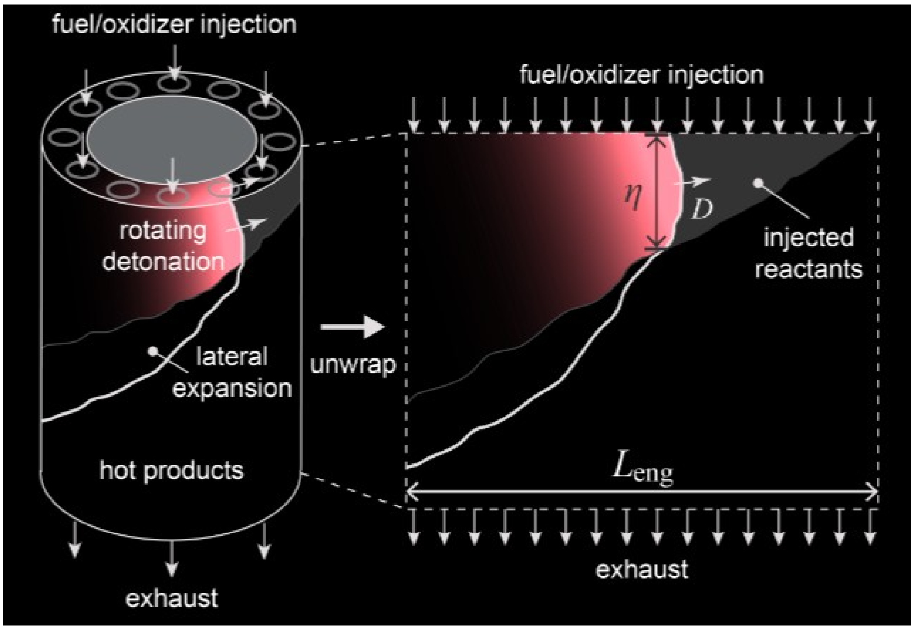

Figure 2.1: Sketch of an RDE with 1-wave operation ($w = 1$) within an annular gap. Reproduced from [18].

reactants, and post-detonation expansion region. The velocity of the shock front is often cited as a percentage of a_{CJ}, the Chapman-Jouguet (product) sound speed, and/or D_{CJ}, the Chapman-Jouguet detonation speed; typically, $a_{\mathrm{CJ}} \approx 50\%\ D_{\mathrm{CJ}}$.

§2.1.3 Coreless RDE Design

RDEs can also be operated without the core, and are known as coreless, hollow, cylindrical or even "center-bodiless (CBL)" RDEs. Primarily since 2011 when Ye et al. numerically demonstrated the feasibility of coreless engine, coreless RDEs have been studied alongside annular RDEs, for the potential benefits of less mass (due to the core removal) and to avoid performance losses associated with deterioration of the inner cores [19]. For small RDEs less then 30 mm in diameter (or sizes significantly smaller than the "typical, 150 mm diameter RDE," per Dechert et al. [20]), the volume-to-surface ratio in annular configurations is greatly increased. At the high temperature gradients in the engine interior, this means that the cores in annular RDEs are much more likely to degrade, resulting in decreasing performance over the lifetime of the RDE. With small RDEs in particular, degradation has been shown to occur with run times of approximately 1 second [21, 22]. Moreover, although there may be performance losses in coreless engines depending on experimental conditions, on the whole research has shown coreless configurations to be roughly equivalent in parameter performance [16, 23]. This makes coreless engines attractive for a wide variety of small and/or low-thrust rocket engine applications.

For a visual example of a coreless RDE, Fig. 2.2 presents a computational fluid dynamics simulation of the pressure contours in a hollow engine. The time is measured in microseconds, μs, from the pre-detonator blast that starts the detonation wave. The shock waves reverberate through the hollow combustor, and eventually settle to a steady-state operation with the curved detonation wave front (arrow 1 in the lower right-hand frame), along with the oblique shock wave and additional secondary detonation wave fronts (arrows 2 and 3 in the same frame). Note that unlike annular designs, hollow detonation waves do not necessarily propagate close to the wall. This makes it challenging to characterize the detonation wave operation [24].

§2.2 Literature Review

Rotating detonation engines were first proposed around 1950–‘60, when rocket engine design was under rapid development as part of the Cold War race to the moon. Initial proposals of using detonation waves as an efficient thermodynamic cycle capable of mitigating the combustion instabilities that plagued rocket engine designs came from Zeldovich [25] (published in Russian in 1940), and initial experimentation was carried out by Nicholls et al. in 1957 with hydrogen-oxygen gaseous propellant [26].

Pulsed detonation engines (PDEs), running via pulsed detonation combustion (PDC),

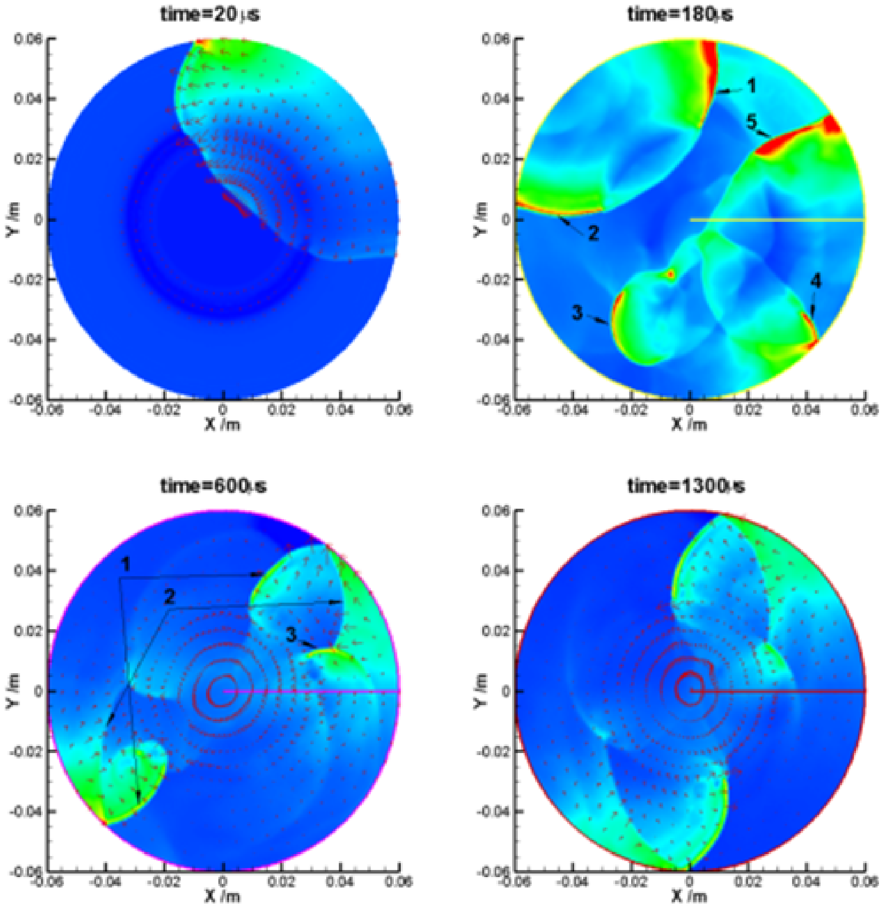

Figure 2.2: CFD-created pressure contours in a hollow RDE (from [19]).

were proposed by Nicholls as pressure gain devices intended to increase the efficiency of internal rocket combustion and suppress combustion instabilities [26, 27]. In a PDE, typically gaseous propellants are injected near the closed end of the combustion chamber (often composed of one or more tubes); a detonation cycle is initiated and propagated down the combustion chamber, and the exhaust exits out the tube's open end, which may or may not be equipped with a nozzle. That cycle is then operated at frequencies of 1–200 Hz [28]. PDEs have also been studied, for instance, by Heiser and Pratt in hopes of creating a practical model for various proposed applications [29]. However, it was realized early on that the PDE presented significant drawbacks due to the discontinuous thrust production, highly unsteady exit flow velocities, the challenges of high-frequency operation and integration into existing turbine rocket models [28, 30].

In 1964 Erpenbeck performed the first linear stability analysis on a perturbed detonation shock front [31]. USA-based research continued through the next several decades studying PDCs, detonations and shock waves by turns. In 1972, NASA published an extensive paper titled "Liquid Propellant Rocket Combustion Instabilities" that summarized all the data gained from the development of the rocket engines of that era and formed a comprehensive base for conducting further testing on fluid-based combustors from "conventional" turbine engines to pulse guns and explosives. It specifically pinpointed several prominent types of instabilities, including high, low and intermediate frequency instabilities, and highlighted the few known methods of damping and frequency control [32].

Research on shock and detonation waves continues today, using a mix of conventional methods with newer experimentation methods as they become available. Ram projectiles propelled by detonation waves in a ram accelerator have been photographed in situ at both the University of Washington and Hiroshima University [33]. Nakayama (2012) studied shock waves in a curved rectangular channel to determine wave propagation and optimum radius of curvature for a generalized detonation wave in a nearly 2D experimental channel. The analysis technique involved layering the photographs taken during the experiment and measuring the success of the wave [34]. This research produced edifying results, even though it does not capture all aspects of the critical 3D wave nature of RDE detonation waves.

On the Soviet/Russian side of research, shock waves and specifically detonation waves were studied by Voitsekhovskii ("Stationary Detonations" in 1959, additionally in 1960, 1963) as the first spinning detonation wave expert. Spinning detonation is similar to the rotating wave concept, except in spinning detonation the detonation waves travel axially along the length of the tube (which is typically much longer than an RDE) rather than remaining attached near the injection front plate [24, 35].

Bykovskii, another prominent detonation/shock wave contemporary expert, published work starting in 1980, 1981 studying specifically cylindrical geometries. In 1994, 1996 (and 2006 [36], 2015) he published research on annular RDEs. His 1997 seminal paper, however, showed the critical attribute of pressure gain with detonation and proved the use of O_2-enriched air/nitrogen combinations with H_2, CH_4, and liquid fuels (all previously unsuccessful mixtures) in a partially enclosed disk-shaped chamber [17]. Further studies on the disk-shaped or "plane-radial" rotating detonation combustion region, with exhaust toward either the center or the periphery, have been carried out by Bykovskii in 2016, 2019 and by Paxson in 2020 [37].

While the detonation-based designs described above are similar to the hollow RDE concept, coreless RDE research began to rise after CFD simulation results were produced by a 2011 study at Peking University which showed the feasibility of coreless RDE operation [19]. In the US, development of coreless engines grew rapidly at locations such as the University of Washington (see Section §2.2.1), the Air Force Research Laboratory [15, 20, 38], the University of Cincinnati [6, 39, 40], and the University of Alabama–Huntsville [21, 41]. Institutions in China including Peking University [11, 42], National University of Defense Technology [43] and others [44] and in Japan such as Yokohama National University [45] and Nagoya University [46] have performed extensive studies on coreless engines. There have also been multi-national collaborative efforts performed, such as the following intriguing results from a Japan-USA cross-national partnership. Sawada et al. (a research group compiled from a total of 4 Japanese institutes, two US universities, and the Japanese Aerospace Exploration Agency) investigated a coreless engine prototype with a unique helical sidewall design that demonstrated control over the direction of the detonation wave propagation and also created measurable torque generation [47]. The torque generation was noted as an additional potential source of generated energy, apart from the traditional method of energy generation using the engine exhaust to create steam-powered turbine rotation. Last, proving control over the direction of detonation wave propagation is critical for any application that places turbines in the engine exhaust for energy capture.

Another multi-lab effort produced comparative study using the same 76 mm annular RDE with a 5 mm gap width, performed by researchers at Purdue, the Air Force Research Laboratory (AFRL), University of Alabama–Huntsville (UAH) and UW. The informative study was designed to test the similarities in RDE run conditions across varying laboratory infrastructures [27].

Various propellant combinations have been tried in RDEs, starting with Bykovskii's innovative work mentioned above. Now-common fuel options include hydrogen (H_2), as the most reactive option with the smallest detonation cell size, methane (CH_4) and ethylene for gaseous fuels, with kerosene, RP_2 or gasoline for liquid fuel combinations [48, 49]. Common oxidizers include oxygen (O_2, as LOX or GOX), nitrous oxide (N_20), or air, depending primarily on the intended individual use cases; the latter are sometimes enriched with oxygen to enhance performance. A list of successful propellant combinations is offered in Anand and Gutmark, 2019, as part of a comprehensive review of current RDE research [24]. Gaseous fuel is primarily intended for rocket engine applications that leave the atmosphere, where the fuel and oxidizer tanks are usually carried along with the rocket; however, cryogenic or liquid fuel may also be used for this purpose. Liquid oxygen is used in cryogenic applications, but maintaining the requisite cryogenic temperatures during application use is difficult and leads inevitably to some loss of fuel due to boil-off and evaporation. Liquid fuel for RDEs, however, may in some cases be more efficient: exciting research by Ishihara et al. suggests that using liquid fuel (tested with LC_2H_4-GO_2, liquid ethane-gaseous oxygen) reduces parasitic deflagrative burning in RDEs, a known performance loss mechanism especially prevalent in hollow engines [50]. CH_4-O_2 or methane-air mixtures are typically used in larger combustors, due to the larger cell sizes and better operating characteristics [51]. This feature is seen in the results analyzed in this study as well [13]. On the other hand, as noted by Xu et al., the high detonability of H_2-O_2 plays a large part in its common use in smaller RDEs [52].

Recent research has expanded on application-oriented experimental testing [5], isolation of detonation wave-specific phenomena [34, 53, 54] and more realistic simulations of RDEs, with the addition of Laval nozzles (also called converging-diverging nozzles) being investigated by several as a preparatory step toward integrating RDEs into typical existing rocket designs [11, 44, 43, 51]. Some relevant findings include the following: that the addition of Laval nozzles reduced performance except in near-vacuum test environments [44], that Laval nozzles with too small a contraction ratio decrease thrust output [51], and that the location of injection rings in a hollow RDE conclusively affects the pressure gain and thus the engine efficiency. On the last point, it was confirmed that radial propellant injection strengthens the high-frequency tangential instability noted in turbine-based rocket engine to promote the rotating detonation wave that is characteristic of RDEs. In addition, it was found that injection rings should be located close to the walls of the cylindrical chamber to achieve the highest pressure within the RDE [43].

Cooling the RDE is also an important consideration. At least one study has tested sidewall propellant injection in a small-scale coreless RDE, finding that the sidewall injection was effective in reducing heat flux to the chamber wall [55].

§2.2.1 Prior research: UW RDE work

There is a substantial body of work previously completed at the University of Washington. This includes initial RDE work starting with Heath (2015, [56]), who explored the question of wave direction in an effort to enhance engine stability using twelve equally spaced spark plugs placed at radial locations around an annular RDE. It was found that the diameter-to-gap ratio was of much greater importance than initially predicted, i.e. that detonation cell size was of prime importance, and that the actual direction of the detonation wave affected the engine performance very little. Testing continued with six spark plugs in an effort to promote varying numbers of detonation wave fronts, which resulted in conclusive evidence that the mass flow rate, $\dot{m}$, has a direct impact on the number of detonation waves, and that steady-state operation will establish as many waves as necessary to consume the available mixed propellant without the need for external forcing via phased sparking [57]. Ongoing investigations into annular RDEs continued with nearly yearly publications 2017 through 2019 [57, 58, 59, 60, 61], 2023 [62, 63], 2024 [22, 64, 65] and 2025 [13].

Of special interest to this work are the thorough investigation of wave dynamics and harmonics by Koch [66] and the extensive data set produced in 2023 by Mundt [21, 62] and Roberts [63, 65], respectively, which composed the bulk of the data used for comparison in this study.

Koch found that the detonation waves of RDEs are not, as 1D detonation wave theory states, independent of each other. This is because the mass flow-dependent parameters of fill time and induction zone length (i.e. mixing zone length) behind a leading detonation wave provide a communication pathway for the wave speed to vary directly with the number of detonation waves consuming the incoming fuel. It was proven that DWs are mode-locked into limit cycles based on these parameters, and will recombine or dissociate via bifurcation whenever the fill height behind the detonation wave increases beyond the minimum fill height needed to sustain the wave [59]. Bifurcations are a well-studied event in mathematics, and the experimentally validated harmonics of detonation waves are well-matched to the mathematically-based theory laid out by Koch. While Koch proved detonation waves do interact on local scales as well as participating in engine-level dynamics, which solved one mystery of detonation wave operations, he resolved only a subset of the local-scale interactions. The harmonics or acoustics of the RDE as a whole are a much larger question, and were left unanswered by this initial work.

Mundt produced studies comparing multiple parameters in two sizes of small RDEs (10 mm and 25.4 mm), both hollow and annular, with annular gap sizes varying from 2-5 mm wide and propellant combinations of both H_2-O_2 and CH_4-O_2 [62, 21]. While Mundt's work provided good comparative analysis for the data presented in the works cited above, he was not able to make use of the full dataset gathered; instead, data was primarily categorized and reported according to equivalence ratio similarities. The remainder of the data has been under continued investigation, published in part [67, 13], and further extrapolated here for such parameters as engine frequency (acoustics) and calculated detonation wave speeds.

Roberts, on the other hand, focused on simulating the length of the pre-ignition propellant tubes to study the parameters of mixedness on engine performance [63]. He found that longer approach tubes allowed for better overall mixedness and thus higher fuel efficiency (less waste), in theory improving RDE performance. It was therefore shown that mixedness is a parameter of some importance to the engine performance; however, qualitative methods to evaluate how and exactly what effects mixedness has on performance were not developed. While the remainder of Roberts' work is not directly applicable to the bulk of this thesis, some of the comparative data published in his paper as well as the lab description and experimental set-up are relevant to this study.

Chapter 3

Methods

This Chapter relies on the work of comparison between 10 mm and 25 mm RDEs, operated with both coreless and various annular gap widths, the derivation of an acoustic analysis for these RDEs, and a description of the 10 mm RDE run with heated propellant. With the exception of the heated propellant data, much of the initial testing data for these configurations has been previously reported, as noted in Section §2.2.1. However, to more fully understand the physics of detonation waves and the properties of the accompanying acoustic wave with the RDE chamber, an acoustic analysis has been performed and compared to the initial data obtained experimentally.

In Section §3.1, the UW RDE lab is described, including the instrumentation used, experiment run order, and the dimensions of the combustors used. For example, the 10 mm and the 25 mm RDEs exhibited slight differences in construction due to the size variance. Specifics of these differences are discussed in Sections §3.1.2, §3.1.3.

Section §3.2.1 gives an overview of the relevant physics of detonation waves and acoustics in RDEs. It also covers the previous experimentation completed at the University of Washington Rotating Detonation Engine Laboratory.

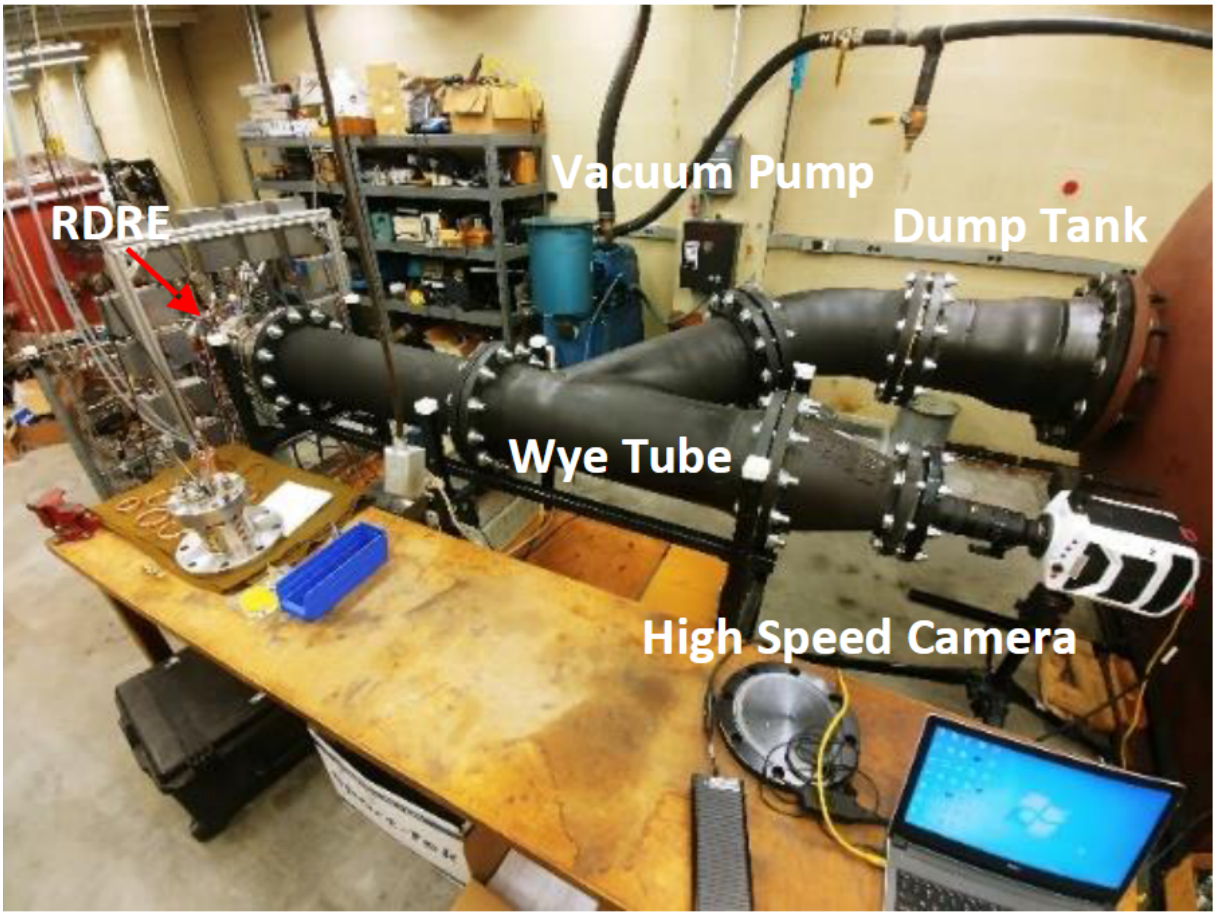

Figure 3.1: The UW RDE experimental test facility

§3.1 Description of UW Rotating Detonation Engine Laboratory

The University of Washington Rotating Detonation Engine test facility is located in an interior laboratory space that has a 4 m^3 dump tank rated from vacuum to 0.7 MPa working pressure. A 0.25 m diameter wye tube, shown in Fig. 3.1, connects the dump tank to the RDEs on the test stand. The wye allows for an observation port to be installed at the end of the straight leg, i.e., directly aft of the combustor exit. The wave dynamics within the RDE combustors were captured by Phantom digital video cameras using either a 70-200 mm or 200-500 mm zoom lens with frame rates up to 450,000 frames per second (FPS) at 0.9-1.9 μs exposure time [13].

The RDE rig is oriented such that the exhaust proceeds in the axial direction, along the wye tube and into the dump tank. After each experiment, the dump tank contents were purged by a Kinney KT-300 vacuum pump, which was also used to set sub-atmospheric back pressure as low as 2 kPa (0.02 bar) prior to engine operation [62]. For all test runs, a mixture of gaseous oxygen and either gaseous methane or gaseous hydrogen was used.

§3.1.0.1 Instrumentation and flow handling

Oxidizer and fuel flows were regulated with TESCOM ER5000 and TESCOM 44-4000 series electronic regulators. Flow data in the upstream run lines and in the experiment plenums was measured with OMEGA PX319-500A5V pressure transducers and low-noise thermocouples (exposed-bead Type K thermocouples, OMEGA TJ36 CASS-116E-12) in approach tubes that were factory calibrated with critical flow nozzles (CFNs). The CFNs were fabricated by Fluid-Dyne from Monel© for high corrosivity resistance, and were sized for sonic flow of the oxidizer (O_2) at 0.110 in. (2.79 mm) and of the fuels at 0.050 in. (1.27 mm) for CH_4 and 0.030 in. (0.76 mm) for H_2, respectively. These sensors collected experiment mass flux values, upstream propellant temperatures, and pressure values in the upstream lines. PCB 113 piezoelectric pressure transducers, sampled at 1.25 MHz, were mounted in approach tubes (equipped with snubbers) that connected to the sidewall and plena of both combustors. This allowed fast-response data collection of the pressure inside the plena, in the combustor interior, and just aft of the combustor. The remaining sensors were sampled at 2 kHz via a National Instruments-based 32-channel data acquisition system (DAQ). Propellant mass flow rates ranged from $\dot{m} = 0.006 - 0.44$ kg/s and equivalence ratios ranged between $\phi =$ 0.2-2.8. The net uncertainty in mass flow rate and equivalence ratio was ±1.5% [67].

The laboratory flow handling system is shown in Fig. 3.2, with details on the flow

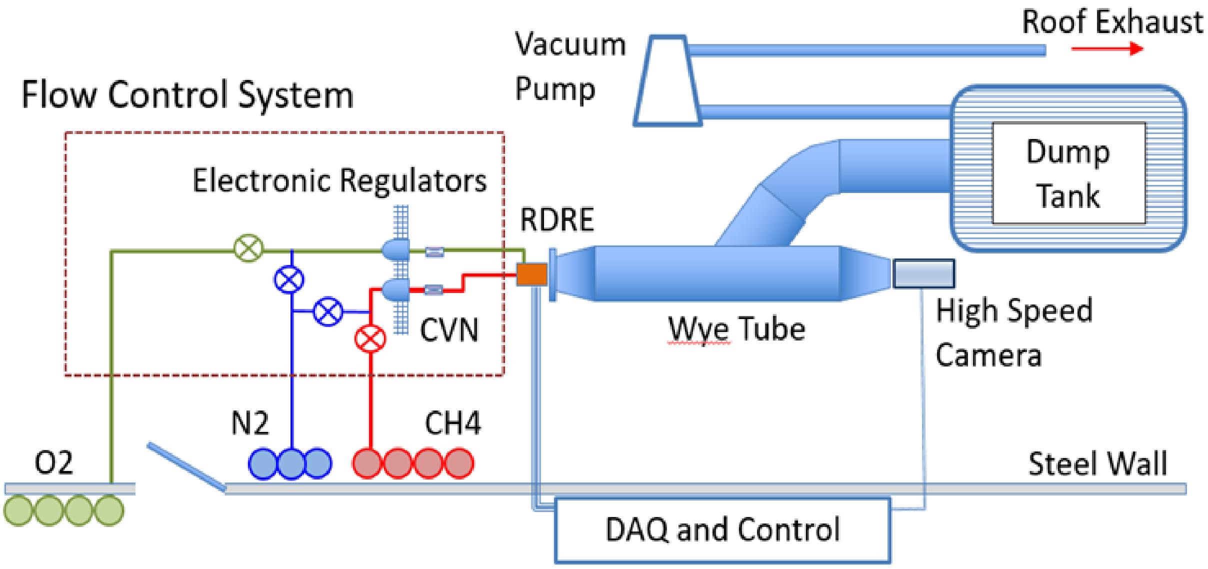

Figure 3.2: Flow handling and control system diagram in the RDE lab.

control system shown in 3.3. The pre-detonator schematic in Fig. 3.4 shows the RDE ignition system, which is used to commence detonation via the sparkplug and pre-detonator fuel slug.

Both RDE geometries utilized the same stainless steel endcap (SS304), but with different brass injectors and copper outer walls (see Figs. 3.5, 3.9, 3.12). The injectors were located between the outer core and the endcap and centered to within within 0.026 mm of the combustor centerlines. The oxidizer (GOX) was flowed through four feedlines into an annular plenum within the endcap, which in turn fed a thinner annular disk into which injector ports were drilled. These parts were used for both RDE sizes, and can be seen in detail in Figs. 3.9 and 3.12 along with the size-specific injector designs. The plenum pressures and temperatures for the oxidizer injectors were measured in the outer annulus.

Similarly, the fuel was flowed through a single feedline into a cylindrical fuel plenum located at the center of the endcap. The fuel plenum pressure and temperature were measured in a plumbing tee connected to the 25 mm welded port fitting at the rear of

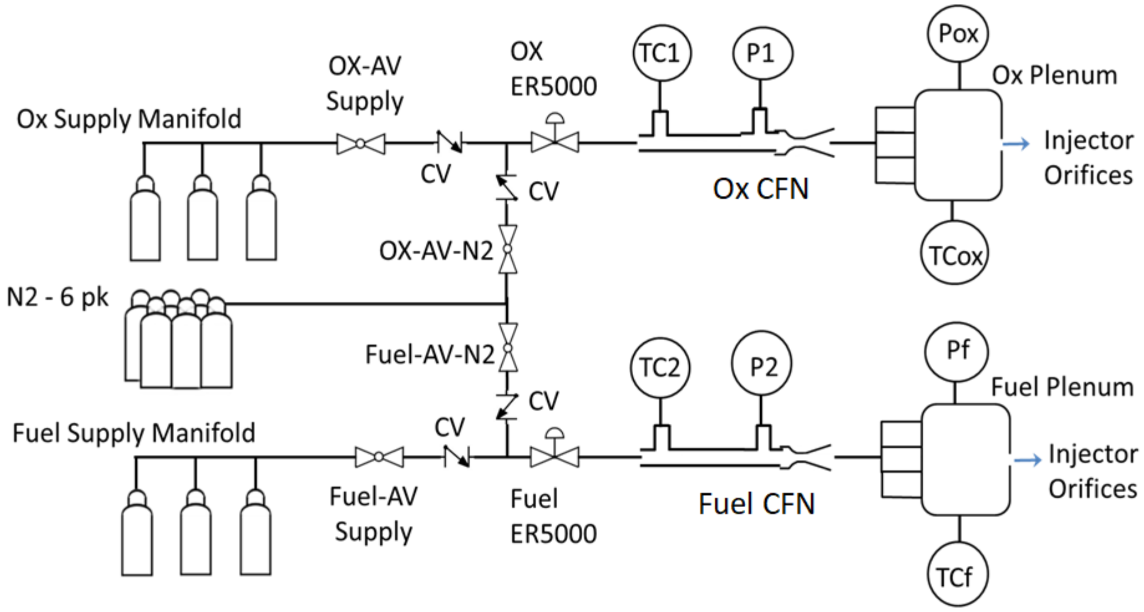

Figure 3.3: Detailed propellant flow diagram, used with minor changes for both RDE sizes.

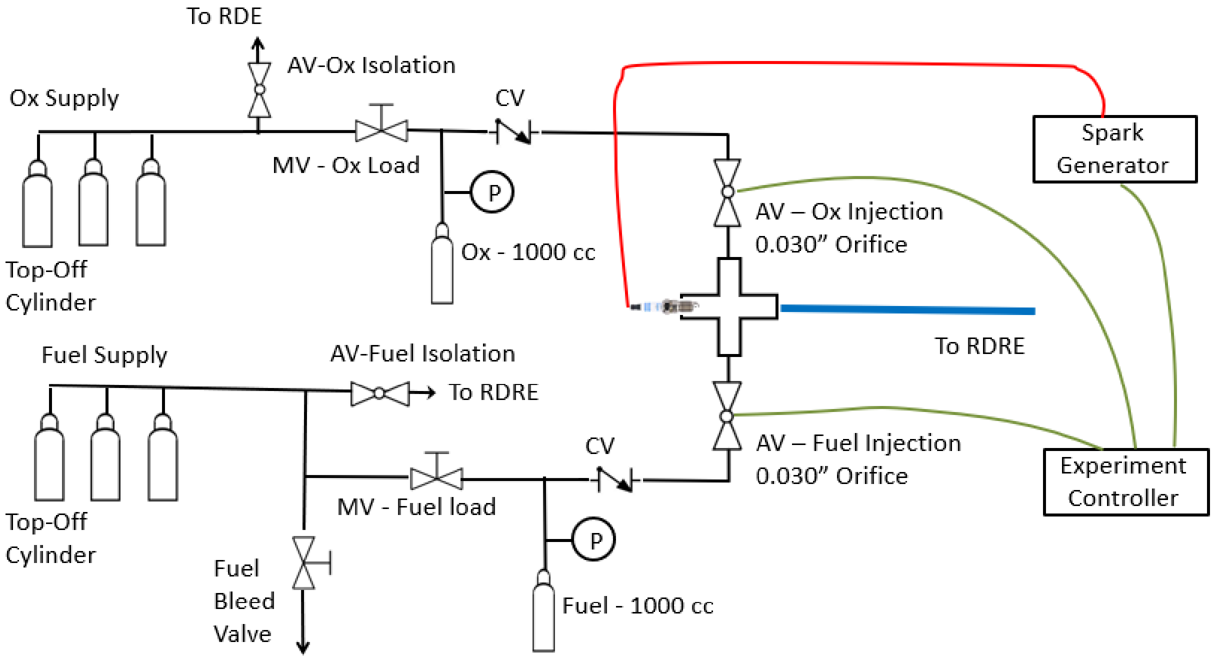

Figure 3.4: Pre-detonator flow and control system diagram, used to initiate detonation in both RDEs.

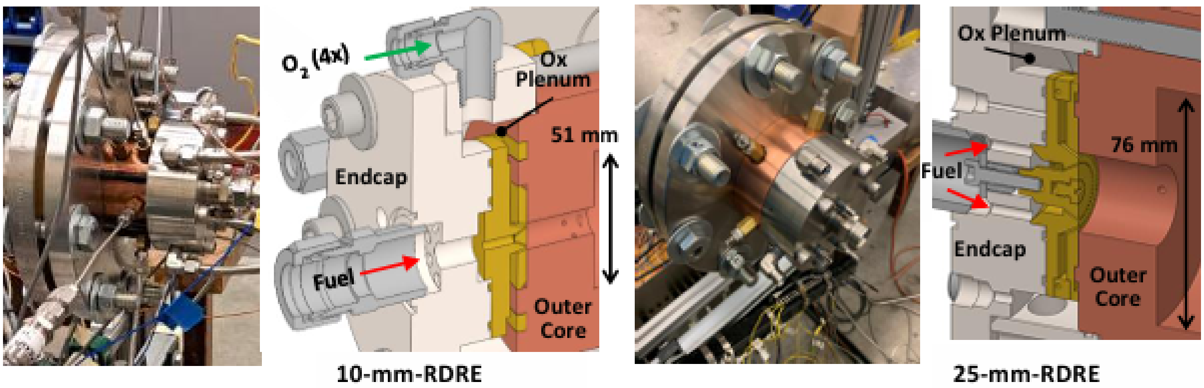

Figure 3.5: Design details of the RDE configurations. Left: 10 mm RDE on the test stand and 10 mm RDE section view. Right: 25 mm RDE on the test stand and 25 mm RDE section view.

the test rig. Fuel was injected into the engine from the inner ring of injector ports on the annular injector disk. The pressure drops in the plenum pathways were negligible relative to the drops at the injector ports for the fuel mass flow rates considered in this investigation, as noted by Knowlen et al. [13].

The port diameters ($d_o = 0.81$ mm and $d_f = 0.51$ mm) and area ratios ($A_o/A_f = 2.56$) were the same for both RDEs, meaning that the fuel and oxidizer plena for both engines had the same injector pressure drop at fuel equivalence ratios of 1.08 with CH_4-O_2 and 0.78 for H_2-O_2. The injector-to-combustor area ratios, however, differed from 0.11 (for the 10 mm RDE) to 0.067 (for the 25 mm RDE), resulting in the larger combustor having stiffer injectors at a given propellant mass flux.

Detailed figures of the engine geometries for the 10 mm and 25 mm RDEs are shown in Secs. §3.1.2 and §3.1.3, respectively.

Post-processing of the experimental data included running the high-speed video and PCB 113 pressure data through a 2D Fast-Fourier Transform (FFT) process, from which were created spectrograms and pressure spike plots. The spectrograms are graphed as frequency vs. the experiment TOR, up to a frequency of 120 kHz, while the pressure spike plots were graphed as power in dB vs. frequency from 1–240 kHz over the TOR.

This allowed for more detail to be seen than in the spectrograms, although after 120 kHz the frequency spikes shown are merely a mirror image of those found in the 1–120 kHz frequencies. FFT relies on collapsing large amounts of data into much smaller bundles for processing, which allows faster computation time and additionally much clearer results; FFT calculates the primary temporal and spatial modes of operation which characterize the number of waves as well as the precession speed and direction of each wave. However, it also creates artifacts in the form of integer multiples of the strongest frequencies, hence the chosen cut-off point of 120 kHz.

§3.1.1 Experimentation Run Sequence

For detonation initiation in the combustors, a spark-ignited pre-detonator using CH_4-O_2 reactants was mounted into the last port of the combustor annulus. The pre-detonator was fired 200 ms to 300 ms after the fuel and oxidizer flows were switched on. The combustion process exhibited transient wave behavior initially, but typically established steady-state operating modes within the first 200 ms after firing the pre-detonator. Data was collected during the experiment time of record (TOR), which corresponded to the last 100 ms of the run, and was averaged for each test of the TOR. Gaseous nitrogen was used to purge the fuel and oxidizer supply lines after each run [62]. The data was then saved and post-processing begun.

§3.1.2 10 mm RDE Description

Instrumentation ports for the 10 mm RDE are listed in Table 3.1.

The 10 mm RDE had a combustor with an outer diameter of 10 mm and a length of 20 mm. The fuel (methane or hydrogen) flowed through a 25 mm weld port fitting to

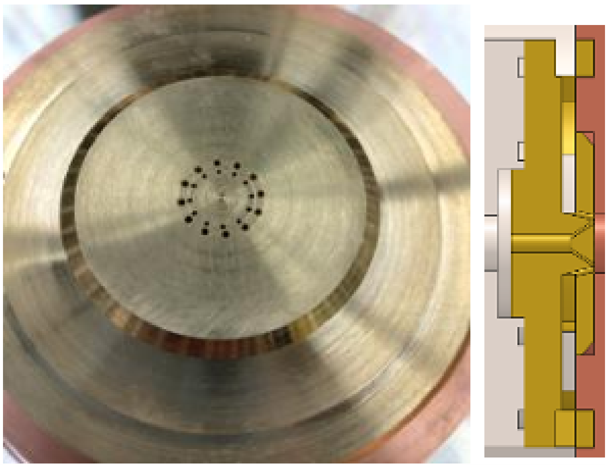

Figure 3.6: 10 mm RDE injector face. Right: front face. Left: cross-sectional view.

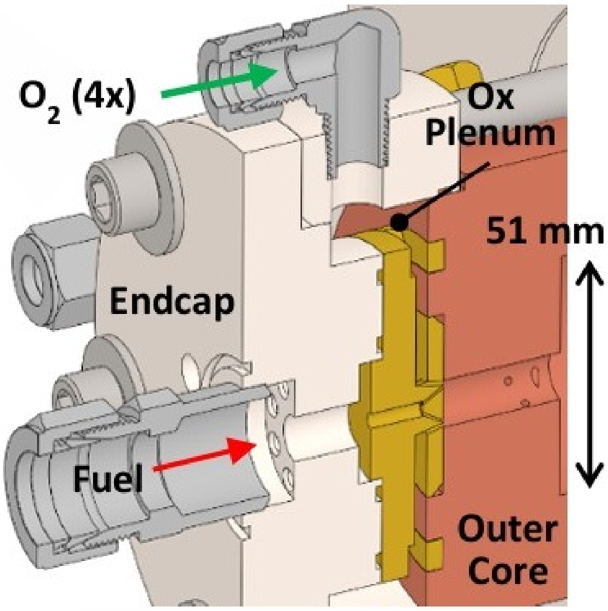

Figure 3.7: Plenum details close-up in the 10 mm RDE.

Table 3.1: Instrument port locations for the 10 mm RDE. Note OD stands for outer diameter, Pre-det. refers to the pre-detonator port location, z is axial length, and dia. refers to the port diameters.

Parameter	Combustor: 10 mm OD × 20 mm long								Exit	51 mm OD	Pre-Det.
z, mm	9.0	9.0	9.0	10.0	11.0	13.0	15.0	17.0	20.0	33.0	17.0
Dia., mm	1.57	2.29	2.29	TC	1.57	1.57	1.57	1.57	-	1.57	2.38
Angle, deg.	345	180	300	60	165	105	195	45	-	345	225

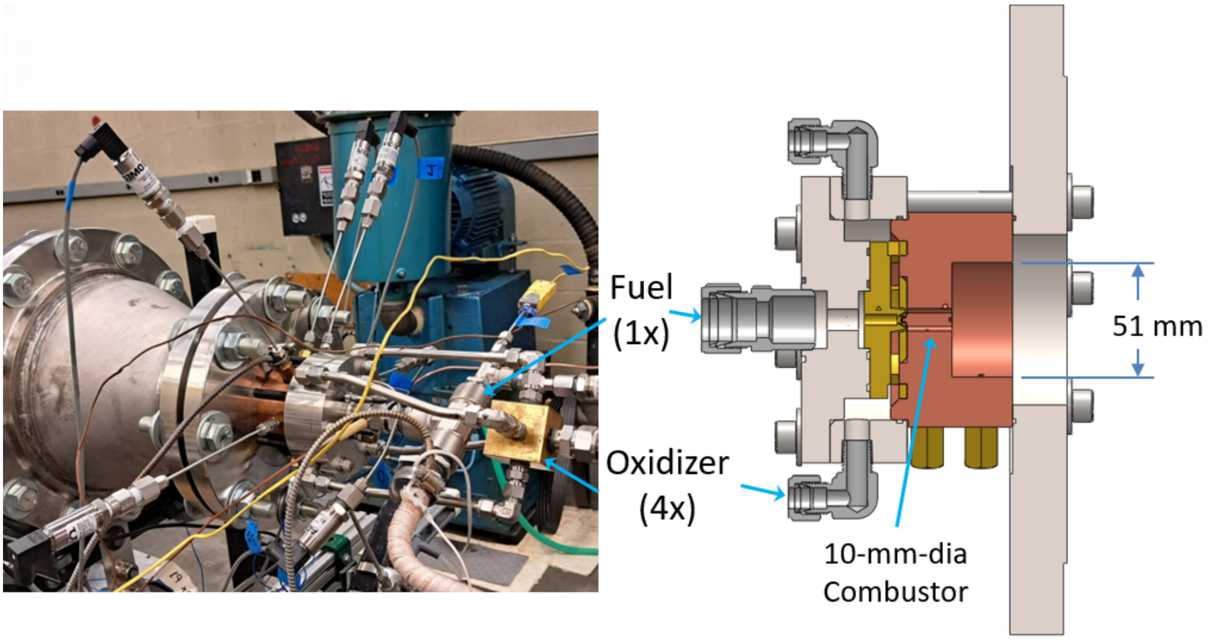

Figure 3.8: Fuel and Oxidizer inlet system in the 10 mm RDE.

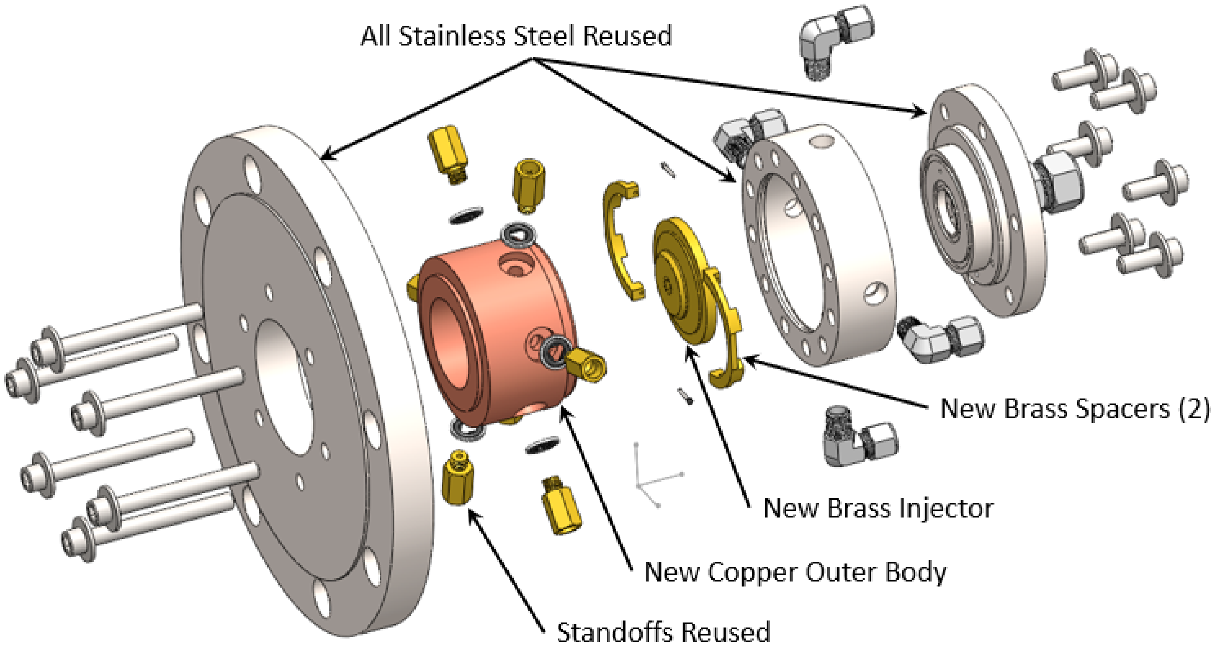

Figure 3.9: Exploded view of the 10 mm RDE.

an eight-hole distributor with 3.2 mm diameter bores, to the fuel plenum, and last to a 4.8 mm diameter blind hole with fuel injector ports drilled into its base, where the fuel was injected into the combustor. To start the combustion, the pre-detonator was fired tangentially through a port near the combustor exit. Outside the combustor, the exhaust products flowed into a cylindrical section 25 mm long and 51 mm in diameter and thence into the dump tank as described above. For details of the laboratory flow system, see Fig. 3.2.

Details of the injector system are shown in Figs. 3.6, 3.7, and 3.8. The 10 mm RDE had 12 pairs of injectors; the oxidizer ports angled inward toward the combustor centerline at 11.3° while the fuel ports angled outward at 30° for an impingement diameter of 8.5 mm. This resulted in a momentum balance, which is to say the promotion of axial flow, at $\phi = 1.15$ for CH_4-O_2 and at $\phi = 0.78$ for H_2-O_2.

Details of the instrumentation ports are given in Table 3.1. The sidewall ports measured axial pressure gradients along with wave frequency and spin speed using the piezoelectric transducers described in Sec. §3.1.0.1. A thermocouple well port of 1.65 mm diameter was drilled to within 6 mm of the combustion chamber outer wall to monitor the wall temperature transients during operation, and a pressure port downstream of the combustor (in the 51 mm diameter section) was used for back pressure measurements.

The 10 mm RDE was also fitted with a 6 mm core for running as an annular engine with a 2 mm gap. However, the data gathered from these experiments were sparse due to the erosion and burning of the core with successive runs. Cores made with copper and molybdenum were unsuccessful in resisting the high heat transfer levels during experiment runs. A single test with a tungsten core showed promise in that the core was undamaged; however, the design needed reworking to prevent the core from separating from the injector plate during test operation. Tests were conducted using both methane (CH_4) and hydrogen (H_2) fuels. More details on that experimentation are given in [21].

§3.1.2.1 Heated Propellants

The 10 mm engine was also run on methane with heated fuel lines. For this portion of the experiment, the fuel line was replaced with a 0.61-m-long SS tube with a 12.7 mm outer diameter; this was then wrapped in 200 W heat tape, with typical wall temperature settings of 360–400 K. This design raised the fuel exit temperature to an average temperature of 330 K. A PID controller was used to maintain the desired tube temperature, with a thermocouple at the exit of the heated line section used for temperature control. The plenum temperature, as recorded by the plenum thermocouple, showed only a minor decrease in temperature between the heated line exit and the plenum. Hence, the fuel heat loss through the run lines was minimal.

Based on the plenum temperatures of the fuel and oxidizer and a mixing ratio analysis, the fuel heating resulted in a typical mixed propellant temperature increase of 10 degrees (K) [68]. The heated CH_4-O_2 propellant mixture nevertheless performed better at leaner (low-ϕ) mixtures compared to the unheated propellant mixture, as described in the results section.

§3.1.3 25 mm RDE Description

Table 3.2: Instrument port locations for 25 mm combustor. As before, OD stands for outer diameter, Pre-det. refers to the pre-detonator port location, z is axial length, and dia. refers to the port diameters.

Parameter	Combustor: 25.4 mm OD × 25.4 mm long				Exit	76 mm OD	Pre-Det.
z, mm	16.5	18.5	20.3	22.4	25.4	38.1	22.4
Dia., mm	2.38	2.38	2.38	2.38	-	2.38	3.18
Angle, deg.	0	60	240	120	-	180	180

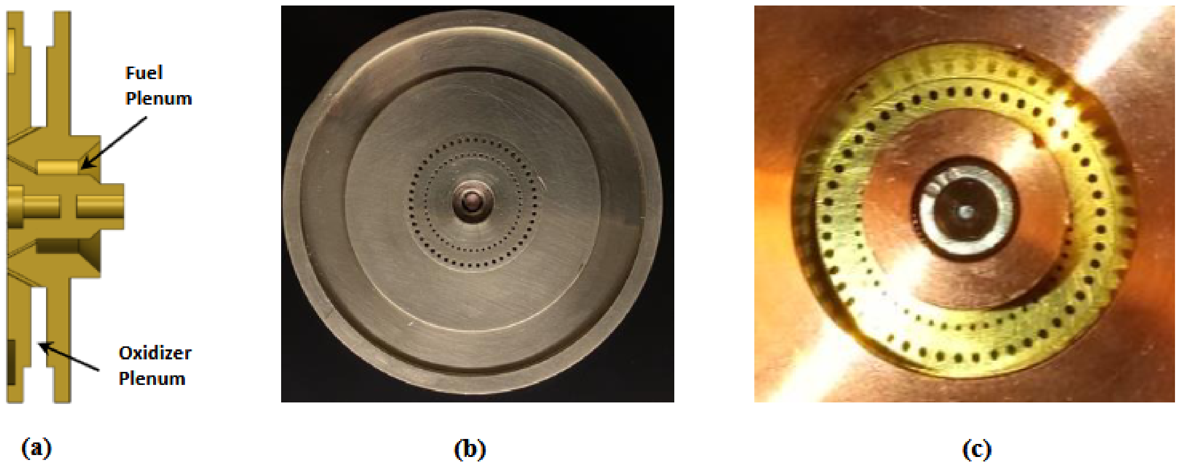

(a) (b) (c)

Figure 3.10: 25 mm RDE injector. a) Cross-sectional view; b) Front face; c) Front face when installed, shown with the 15 mm inner core (5 mm gap) [21].

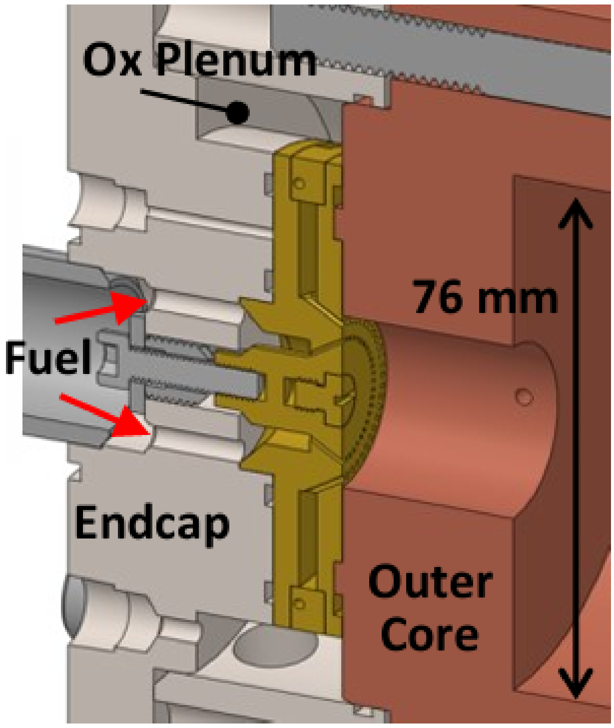

Figure 3.11: Plenum details in the 25 mm RDE.

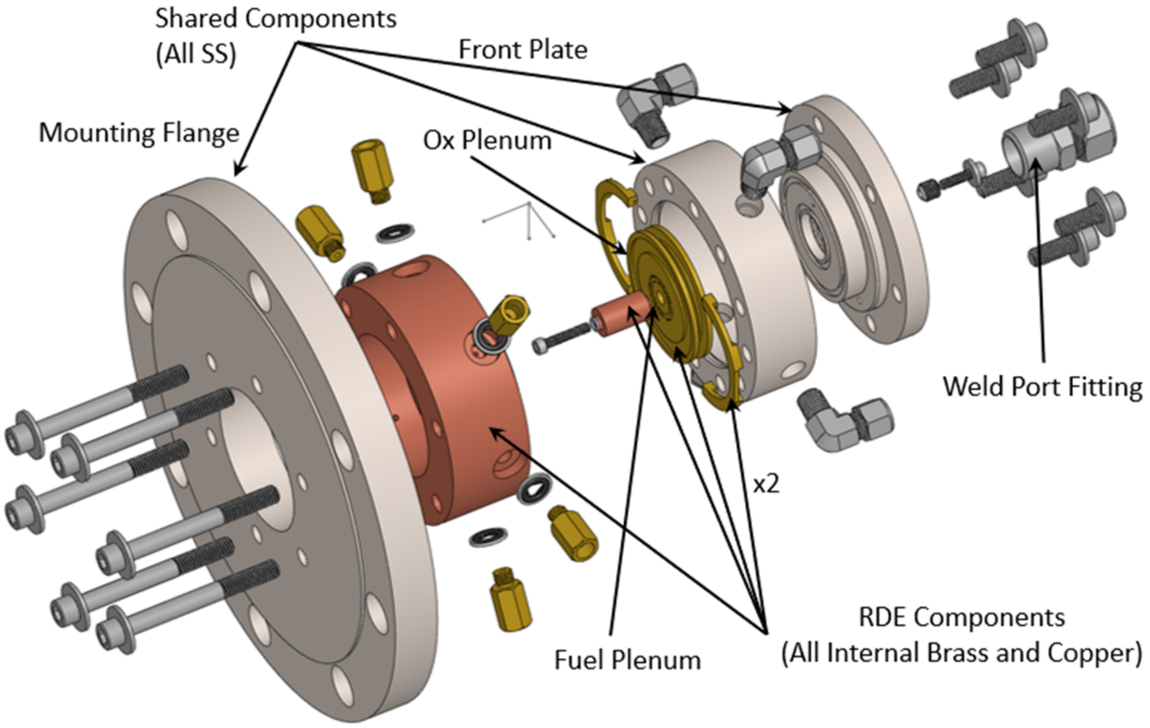

Figure 3.12: Exploded view of the 25 mm RDE.

The 25.4 mm diameter combustor was also 25.4 mm long. The threaded center hole used to retain the injector ring and the eight outer ports feeding the coaxial annular fuel plenum were similar to the fuel injector system in the 10 mm RDE. Additionally, the pre-detonator was fired radially inward in the 25-mm-combustor, while the pre-detonator port was located opposite the last instrument port in the combustor. The exhausted products exited the combustor into a cylindrical section 25 mm long and 76 mm in diameter and into the dump tank.

Details of the injector are shown in Figs. 3.11 and 3.10. This injector had 48 pairs of straight hole ports; the oxidizer ports angled inward (toward the combustor centerline) at 30° and the fuel ports angled outward, also at 30°. The impingement ring diameter was 20.4 mm, with momentum balance at $\phi = 2.93$ for CH_4-O_2 and at $\phi = 1.99$ for H_2-O_2.

Details of the instrumentation ports are given in Table 3.2. The sidewall ports allowed measurement of both axial pressure and wave spin frequency and speed. The back pressure measurement port was located aft of the combustor exit in the 76 mm diameter section.

The 25 mm combustor was designed to accommodate the addition of inner cores of varying diameters to enable testing with different annular gap widths. The core diameters and respective annular gaps are listed in Table 3.3.

Images of the 25 mm RDE during operation as a hollow engine and with gap sizes of 3 mm, 5 mm and 7 mm are shown in Fig. 3.13.

Table 3.3: Annular and hollow gap sizes and area ratios (AR) in the 25 mm RDE.

Annular gap	Core dia.	Gap center	Injector-gap AR
3 mm	19.4 mm	22.4 mm	0.164
5 mm	15.4 mm	20.4 mm	0.108
7 mm	11.4 mm	18.4 mm	0.086
Coreless	0.0 mm	12.7 mm	-

§3.2 Physics of Detonation and Acoustics in RDEs

In this section, an analytical background in the physics of detonation waves and the acoustics relevant to RDEs is presented.

§3.2.1 Physics of Detonation Waves in RDEs

The thermodynamic cycle employed in RDEs can boost engine performance via gains in stagnation pressure. Heat addition at constant pressure (ideal Brayton cycle) is the thermodynamic principle underlying gas turbine engine thrust generation. In contrast, PGC (pressure gain combustion) relies on heat addition at nearly constant volume (ideal Humphrey cycle), resulting in decreased entropy generation and increased ideal thermal efficiency [31]. This is illustrated by Figure 3.14, (reproduced from [29]), where the area enveloped by the respective curves represents the total power created by a given quantity

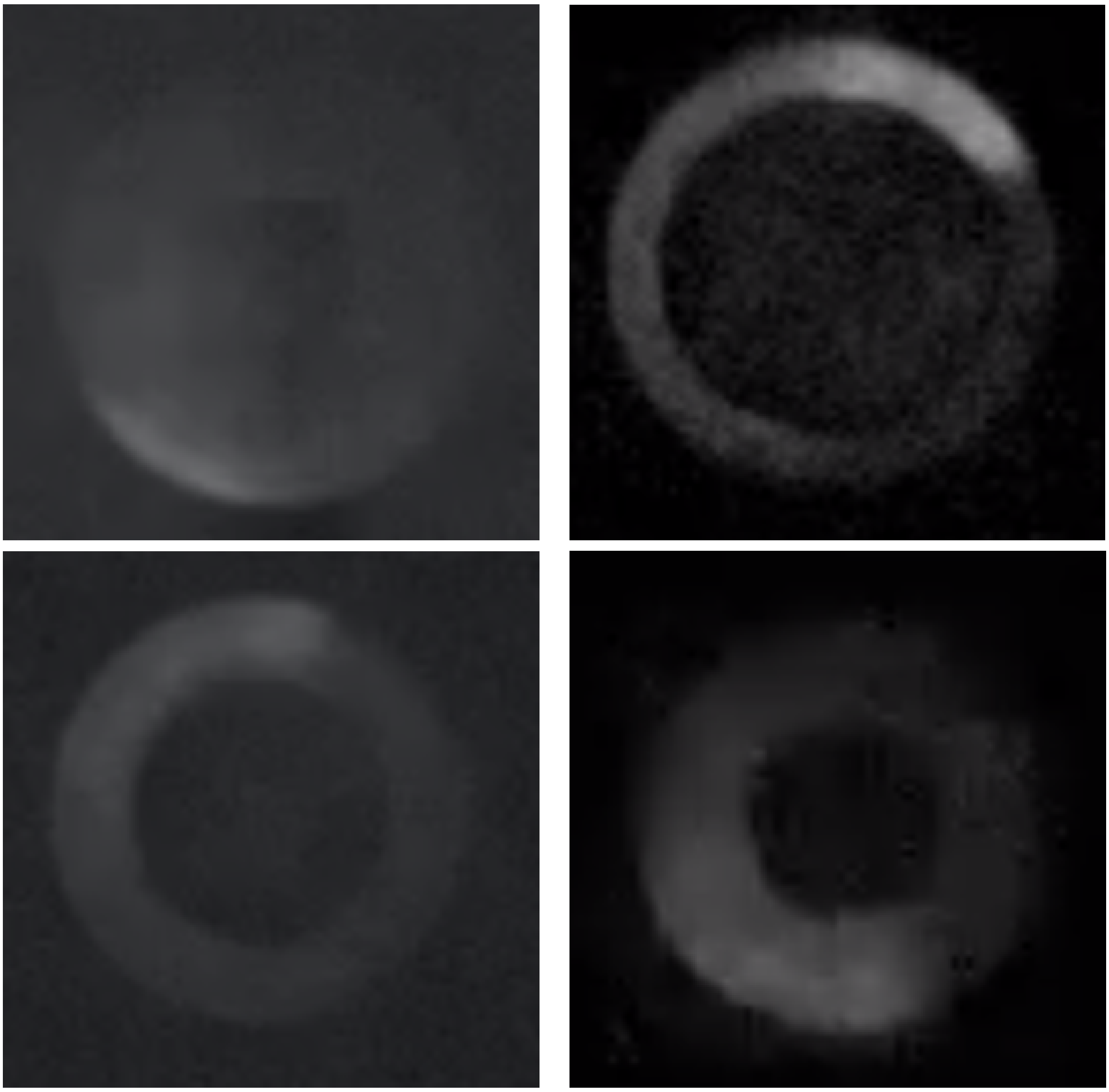

Figure 3.13: 25 mm RDE, CH_4-O_2: pictures of experimental operation taken as 450,000 FPS, 1.9 μs exposure time. Top Left: Hollow configuration. Top Right: Annular configuration with 3 mm gap. Bottom Left: Annular configuration with 5 mm gap. Bottom Right: Annular configuration with 7 mm gap.

of fuel, showing the increase in power output for the same quantity of fuel input. The gain in efficiency is seen by the line labeled PDE (for Pulsed Detonation Engine, as in Sec. §2.2) as an entropy decrease $(s - s_0)$ due to higher combustion temperature. Notably, and unlike the Brayton cycle, this gain does not require prior compression. The advantage is reduced for increased combustor inlet temperatures, which highlights the need for accurate assumptions [31]. While RDEs do not demonstrate overall combustor pressure

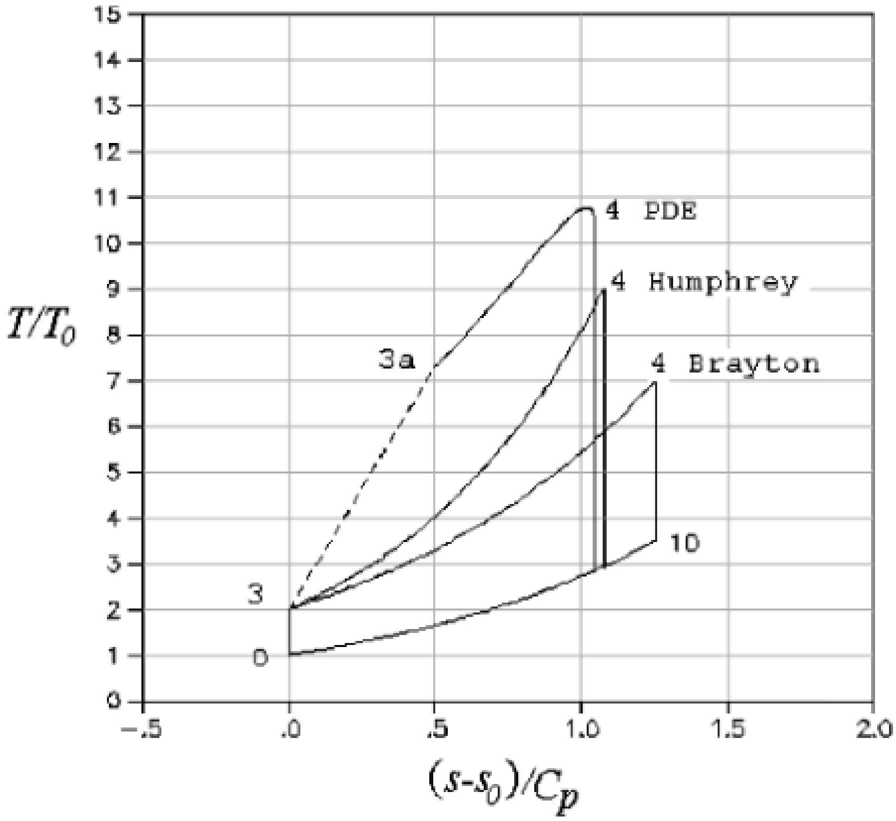

Figure 3.14: Pressure gain combustion (PGC), Brayton and Humphrey cycles. More work is produced from the same fuel using a PGC cycle such as a pulsed detonation engine (PDE) or rotating detonation engine (RDE).

gain, the reduced pressure loss due to the Humphrey cycle still effectively realizes efficiency improvements over Brayton cycle-based engines.

The physics of one-dimensional detonation-driven shock waves can best be described with the Zeldovich-von Neumann-Döring (ZND) model. The key assumption of the ZND model is that the leading shock wave incites chemical reactions immediately after its passage through detonable mixtures, but does not itself contain chemical reactions [69]. More specifically, as shown in Fig. 3.15 the leading shock wave, which is on the order of a few mean free path lengths wide such that

$$1 \leq \lambda_{\text{mfp}} \leq 4$$

is followed first by an induction zone and then by a reaction zone. The corresponding

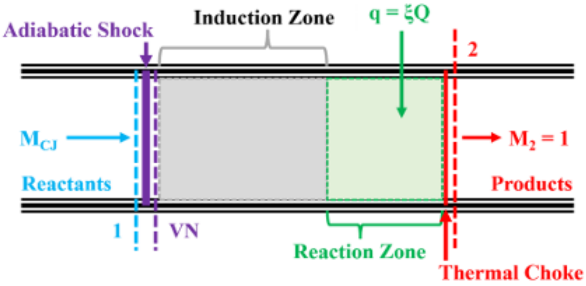

Figure 3.15: ZND detonation model, from the shockwave frame of reference [62].

exothermic release from the reaction zone provides the energy to drive the leading shock forward. This model allows for the decoupling of the leading shock wave and a subsequent Chapman-Jouguet deflagration zone into an idealized three-part system (shock wave, induction zone and reaction zone), considerably simplifying the problem of solving for the detonation wave dynamics [70].

For a 1D, adiabatic, constant-area duct flow with negligible viscosity and body forces, the conservation equations of mass (Eq. 3.1), momentum (Eq. 3.2) and energy balance (Eq. 3.3) relating to stations 1 (upstream of the detonation) and 2 (downstream of the detonation wave) are given by:

$$\rho_1 u_1 = \rho_2 u_2 \tag{3.1}$$

$$p_1 + \rho_1 u_1^2 = p_2 + \rho_2 u_2^2 \tag{3.2}$$

$$h_1 + \frac{u_1^2}{2} + q = h_2 + \frac{u_2^2}{2} \tag{3.3}$$

where ρ is the density, u is the velocity, p is pressure, h is the enthalpy and q is the heat release per unit mass between the two states [66]. The equation of state for an ideal gas is

$$p = \rho R_s T \tag{3.4}$$

where T is temperature and $R_s = R_u/\bar{M}$ is the specific gas constant based on the universal gas constant $R_u = 8.31446$ J/(K· mol) and the average molar mass $\bar{M}$ of the mixed propellant [31].

The average speed of sound a in gaseous propellant is defined as

$$a = \sqrt{\gamma R_s T} \tag{3.5}$$

where γ is the ratio of specific heats of pressure to volume, $\gamma = c_p/c_v$ [71].

By substituting Eq. 3.1 into Eq. 3.2, we can obtain the Rayleigh line, which is a function of pressure, p, and specific volume, v (here $v = \frac{1}{\rho}$). This enables dependence on just one velocity, here chosen to be upstream velocity (u_1):

$$p_2 - p_1 = u_1^2 \rho_1^2 \left(\frac{1}{\rho_1} - \frac{1}{\rho_2} \right) = \frac{u_1^2}{v_2^2}(v_1 - v_2) \tag{3.6}$$

Similarly, substituting Eq. 3.6 into Eq. 3.3, eliminates the remaining velocity term to obtain the Hugoniot curve (which is hyperbolic), also in terms of pressure versus volume (p-v):

$$h_2 - h_1 = \frac{1}{2} \left(\frac{1}{\rho_2} + \frac{1}{\rho_1} \right) (p_2 - p_1) \tag{3.7}$$

The Rayleigh line and the Hugoniot curve can intersect only tangentially, and these critical points are known as the upper and lower C-J points. The upper C-J point corresponds to detonation cycles, while the lower C-J point corresponds to deflagration.

The Rayleigh line, Hugoniot curve, von Neumann state and upper C-J point are graphed in Fig. 3.16. The Hugoniot line (dashed) shows constant q', while the shock Hugoniot (solid) represents where $q' = 0$. The Rayleigh line is split at the upper C-J point into supersonic and subsonic portions; the point where the shock Hugoniot and the subsonic Rayleigh line meet is defined to be the von Neumann state (vN). As combustion at constant volume progresses, the bold path marked with arrows is followed. In an RDE, the combustion continues by following the “constant volume combustion” line back to point (1), forming a continuous combustion loop.

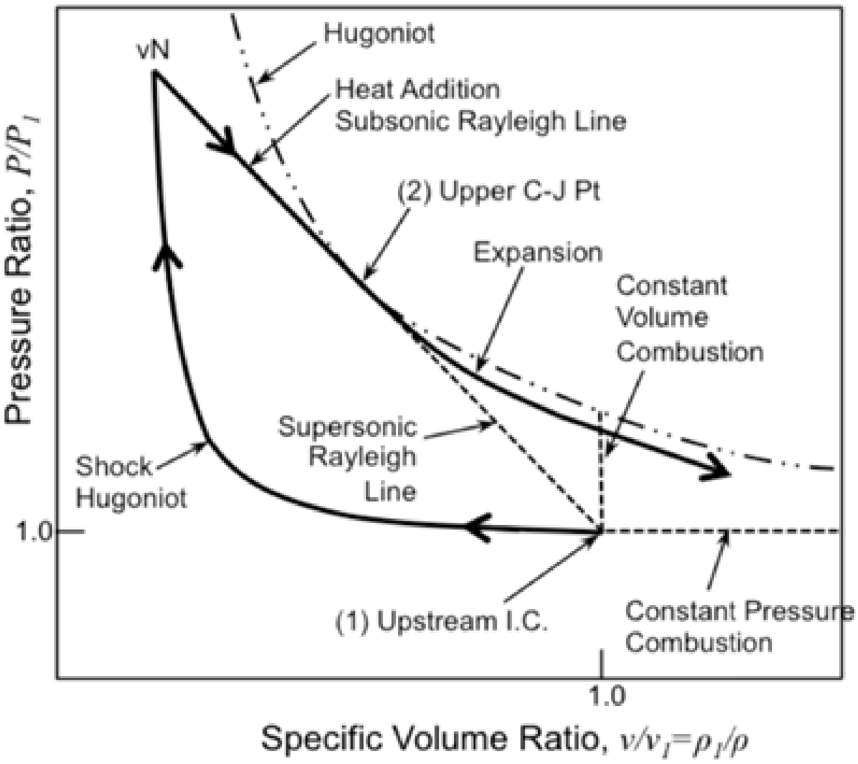

Figure 3.16: ZND Pressure vs. Volume diagram.

Mach number is defined as

$$M = \frac{u}{a} = \frac{u}{\sqrt{\gamma R_s T}} \tag{3.8}$$

The conservation equations can be solved for a given wave Mach number M_1 and a set of initial conditions (p_1, v_1, and q' — here q' represents heat addition), although the solution may or may not be unique depending on the value of M_1. The chemical energy released as heat in the wave, q', is determined by the propellant composition at equilibrium [31].

At the C-J points, the detonation velocity must satisfy the following jump condition across the detonation wave front:

$$h_2 - h_1 = (p_2 - p_1)\frac{v_1 + v_2}{2} - q \tag{3.9}$$

Detonation waves in reactive mixtures are defined as self-sustaining when a shock-induced combustion wave follows the leading shock wave so closely that there are strong interactions between the shock and combustion [48]. The idealized model of a ZND detonation wave is seen in 3.15, in the shock wave frame with thermally choked reactants [62]. The incoming Mach number associated with thermal choking is called the Chapman-Jouguet Mach number, or M_{CJ}, based on the idealized Chapman-Jouguet model and specifically the C-J shockwave velocity, a_{CJ} (also known as the C-J sound speed). M_{CJ} is governed by the following equation:

$$Q = \frac{q'}{c_p T} = \frac{(M_{\mathrm{CJ}}^2 - 1)^2}{2(\gamma + 1) M_{\mathrm{CJ}}^2} \tag{3.10}$$

where Q is the total heat addition, *q'* the local heat addition, c_p is the specific heat and T is the reactant temperature. Solving for Mach number,

$$M_{\mathrm{CJ}} = \sqrt{1 + \frac{q(\gamma^2 - 1)}{2a_1^2}} + \sqrt{\frac{q(\gamma^2 - 1)}{2a_1^2}} \tag{3.11}$$

The shock wave is on the order of one mean free path wide, so there is no time for the chemical reaction of detonation to occur; thus the leading shock can be treated as adiabatic. The induction zone immediately follows the shock wave, and detonation (in the reaction zone) occurs due to the shock-induced elevated temperature and pressure. Propellant ignition, in turn, releases heat and maintains the pressure driving the leading shock; this is known as Rayleigh flow [31]. In the reaction zone, the energy equation is modified to $q' = \xi Q$, where $0 \leq \xi \leq 1$ is a parameter representing the chemical reaction process [62]. After the shock wave, the flow again reaches the thermal choke, and the reaction products are at $M_2 = 1$. For real situations, the flow exiting annular RDEs will be $M \geq 1$ due to the heat loss to the walls and post-detonation combustion effects (as measured by Wheeler [58]).

§3.2.2 Acoustic Modes in RDEs

Performing an acoustic analysis necessitates a thorough understanding of the underlying physics. Acoustics started as the study of sound, originating with vibrational experiments performed by the Greek philosopher Pythagoras in the 6th century to optimize musical composition. The design of Greek and Roman amphitheaters and later theaters was influenced by the discoveries of scientists such as Vitruvius, though the correct theory of sound transmission with a mathematical basis in sinusoidal wave shapes was not fully developed until after the discovery of sound waves in the 17th century and the creation of calculus in the 18th century [72]. By the end of the 19th century, Lord Rayleigh, studying the stability of acoustic wave propagation, found that unstable modes in a closed, gas-filled chamber are driven by the periodic addition (or subtraction) of heat to the system at that point in the cycle where the acoustic pressure is maximum (or minimum) [73].

Stable acoustic modes in a given system correspond to conditions that allow sound waves to propagate steadily, without rapid energy loss or gain. This is generally measured by increasing or decreasing wave amplitude. In contrast, mathematical references to unstable acoustic modes imply system conditions that allow multi-wave resonances to either self-amplify without bound, or be rapidly damped out by wave attenuation or by cancellation due to reflected waves. For a system such as an amphitheater, it is preferable that the building promotes stable acoustic modes over the range of a typical human voice through the breadth and depth of the theater. The design of "sound-proof" rooms is built on promoting unstable acoustic modes that rapidly damp out acoustic vibrations in a given range of the speed of sound in air. But in engineering rockets in particular, the term "acoustic instabilities" generally refers to the third type of unstable mode, where the waves undergo continual amplification and self-reinforcing behavior. Indeed, acoustic instabilities of that type are quite capable of causing serious damage in an enclosed system, however they are initiated.

An acoustic instability as referred to in this work, then, is typically born in an enclosed system. A periodic pulsation is initiated by pressure-based perturbations to the acoustic waves trapped in a chamber such as a rocket engine combustion chamber. Since sound waves must travel through a medium, and the speed of sound depends on the temperature and composition of the gases and other elements of the chamber, the acoustic perturbations may be excited at a wide range of engine conditions based on an equally wide variety of parameters. A short list of such parameters includes the total mass flux through the system, the coupling of the injection or feed system to the combustion chamber acoustics, the incoming propellant velocity and characteristics, the percentage of the fuel-oxidizer mixedness before and after ignition, along with many other factors. Once initiated, the acoustic waves may propagate in longitudinal (along the axial length of the chamber), radial, or tangential directions. Combinations of radial and tangential modes are called transverse modes, and are typically analyzed separately from longitudinal modes due to the inherent differences in initiation factors and propagation characteristics. Such differences allow for the decoupling of longitudinal and transverse modes, making it easier to resolve the pertinent physics [31]. Otherwise, as in Wang's study of vibrations in thick-walled cylinders, the combinations can be quite daunting to separate and categorize [74].

A thorough summary of acoustic modes is presented by Harrje, editor of the influential 1972 NASA report titled Liquid Propellant Rocket Combustion Instabilities [32]. Acoustic instabilities quickly became a primary focus of research among rocket scientists during the twentieth century heyday of rapid rocket engine development [32]. This was due to the observed uncontrollability of what was termed "high-frequency instability" or HFI. However, the initial methodology for improving turbine engine technology involved iterating test conditions over every possible engine operating range, in hopes of detecting and designing methods of damping out the instability modes. This was a very time-consuming (not to mention expensive) task, because once an unstable mode was found, redesigning the engine to remove it often caused another mode to appear at a different set of operating conditions which had previously been found to be stable. Research in recent years has confirmed that the HFI studied and categorized by early rocket engineers are the very same acoustic processes (i.e. transverse acoustic modes) that enable the continual propagation of detonation waves within RDEs [6, 24, 75, 76].

For visualizations of the first few transverse modes (combined tangential (T) and radial (R) modes), see Figs. 3.17, 3.18. Note the high pressure regions in 3.17 are colored in purple, and low pressure regions are colored red. Pure radial modes are of course both radially and tangentially symmetric, while purely tangential modes are not symmetric and may rotate while oscillating about their fixed axis or axes [75, 32, 77]. Since solving for tangential modes results in two eigenvalues, rather than just one for radial modes, the 1T and 2T modes in Fig. 3.17 are shown with perpendicular axes of oscillation, respectively [73]. This same dual-eigenvalue property is what allows tangential modes to rotate as noted above [75].

To derive the mathematical basis of the acoustic analysis presented in this work, it was necessary to draw on a wide variety of resources. Dowling and Stow give a comprehensive overview of the physics of acoustic waves in gaseous combustion, based on the inhomogeneous wave equation [78]:

$$\frac{D^2p'}{Dt^2} - a^2\nabla^2p' = (\gamma - 1)\frac{Dq'}{Dt} \tag{3.12}$$

where the primes represent perturbation variables and a is the sound speed of the gaseous

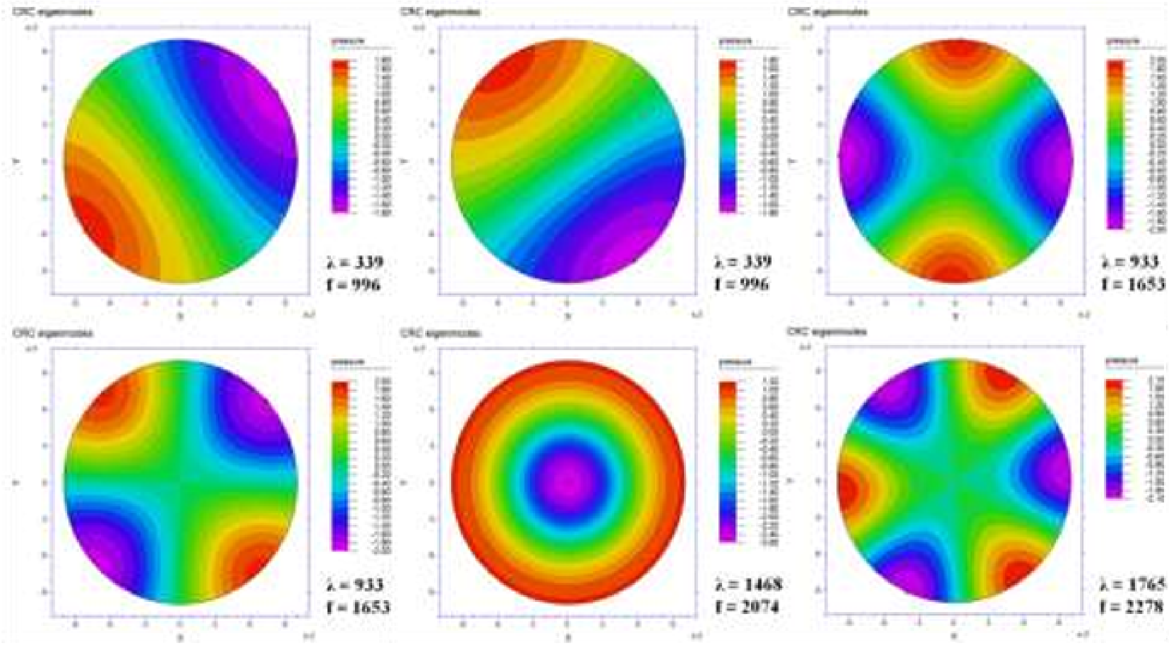

Figure 3.17: Simulated visualization of the first four transverse modes. Top left, top middle: 1T, at two different modal configurations. Top right, bottom left: 2T. Bottom middle: 1R. Bottom right: 3T. Adapted from [73].

propellants.

The wave equation in cylindrical coordinates for the acoustic pressure disturbance is $p' = p'(r, z, \theta, t)$:

$$\frac{d^2p'}{dt^2} = a^2 \left[\frac{d^2p'}{dz^2} + \frac{d^2p'}{dr^2} + \frac{1}{r}\frac{dp'}{dr} + \frac{1}{r^2}\frac{d^2p'}{d\theta^2} \right] \tag{3.13}$$

where t is time, r is the radial variable, z is the axial variable and θ is the angular variable. The solution takes the form

$$p'(r, z, \theta, t) = \sum R(r)\Theta(\theta)Z(z)e^{i\omega t} \tag{3.14}$$

Eq. 3.14, as solved in the rest of this section, was used by Bluemner to create the pressure contours visualized above in Fig. 3.17.

Following the lead of Barrére [77] and Kim [79], we assume the following boundary conditions:

$$\frac{d}{dr}R(r)|_{r=a} = \frac{d}{dr}R(r)|_{r=b} = 0 \tag{3.15}$$

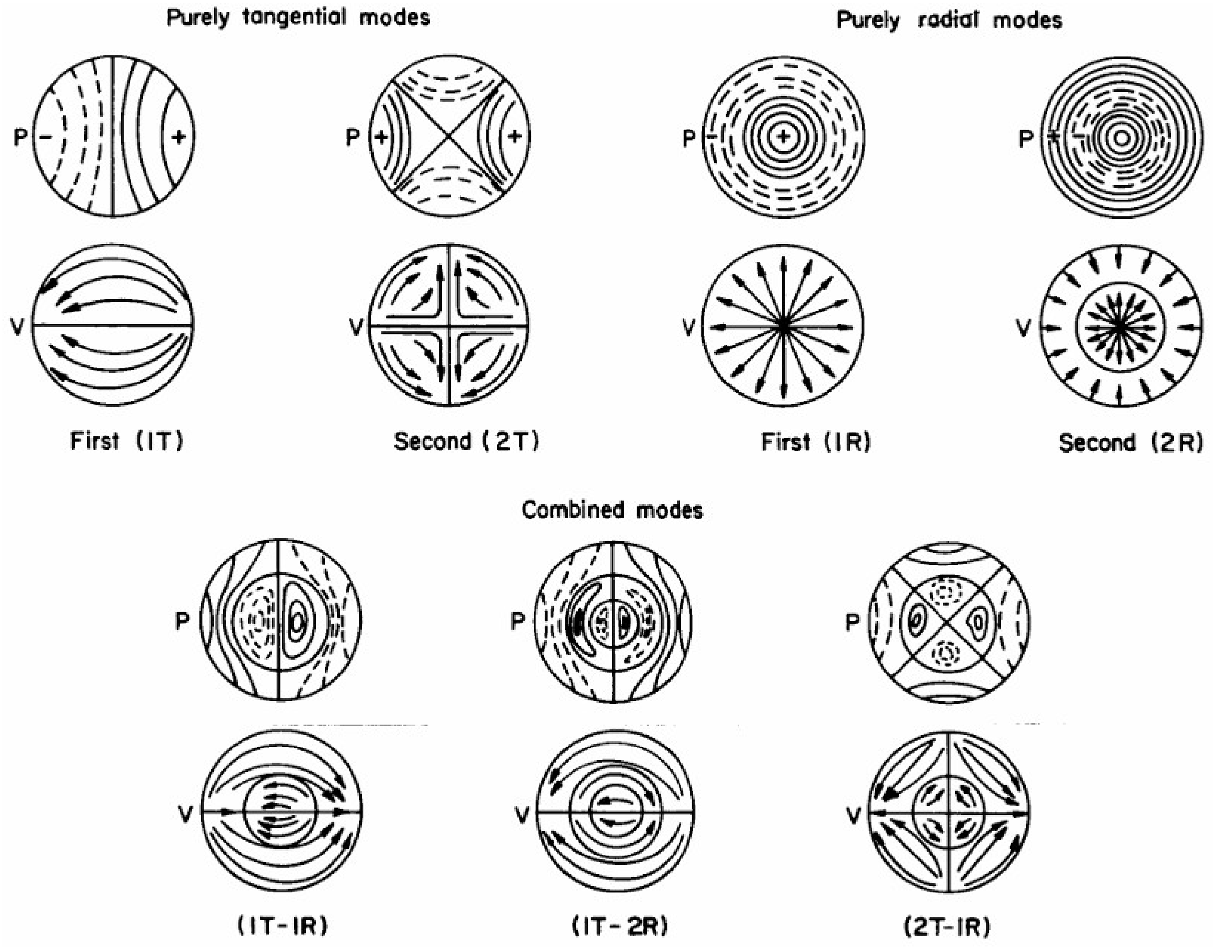

Figure 3.18: Sketch of pressure (P) and velocity (V) contours for the first several transverse modes. Adapted from [32].

$$\frac{d}{dz}Z(z)|_{z=0} = \frac{d}{dz}Z(z)|_{r=L} = 0 \tag{3.16}$$

These simple boundary conditions are motivated by the following points, in order to represent the basic, underlying acoustics of a cylindrical hollow duct:

1. At every cylinder wall, the gas velocity normal to the wall is equal to zero.
2. The solution must be n-periodic in θ with period 2π.
3. The function must be finite for all values of r, θ, z and t.

Note that this last point is important in order to obtain a physically relevant solution [73].

The mode function is

$$R(r) = A_n J_n(\alpha\pi) + B_n Y_n(\alpha\pi) \tag{3.17}$$

where J_n and Y_n are Bessel functions of the first and second kind, respectively, and α is the input variable. The remaining solutions of Eq. 3.14 for $\Theta(\theta)$ and $Z(z)$ are sinusoidal-exponential in form, leading to the equations

$$\Theta(\theta) = c_1 \exp(-in\theta) + c_2 \exp(in\theta) \tag{3.18}$$

$$Z(z) = c_3 \exp\left(-i\frac{\xi z}{L}\right) + c_4 \exp\left(i\frac{\xi z}{L}\right) \tag{3.19}$$

where L is the chamber length, and both the constants $c_1 - c_4$ and the parameters ξ and n are determined by initial conditions and the system's physical limitations.

The boundary conditions given above, when substituted into Eqs. 3.17–3.19, give $J'_n(\alpha\pi) = 0$ and $\xi = n\pi$; note that since the Bessel functions are solved in cylindrical geometries, the tangential mode numbers n will be of integer order. In the case of the common example of a hollow duct (here, a hollow RDE), solving for the cavity's acoustic resonances corresponds to finding the engine-level frequencies or "operating modes" [32, 31]. The final equation for the natural frequencies of the system is then found to be

$$f_{mnq} = \frac{a}{2}\sqrt{\left(\frac{\alpha_{m,n}}{r}\right)^2 + \left(\frac{q}{L}\right)^2} \tag{3.20}$$

where $\alpha_{m,n}$ is then the m^{th} root of $J'_n(\pi\alpha) = 0$ and r is the combustor radius. $\alpha_{m,n}$ is also commonly referred to as the pressure function's eigenvalues (i.e., the eigenvalues of Eq. 3.13), where m expresses the eigenvalues in ascending order such that $n = 0, 1, 2...$ is the n^{th} Bessel function and $m = 1, 2, 3...$ is the m^{th} eigenvalue.

Similarly, for an annular RDE the frequency equation was formulated, for example, by Kim as part of the development of a four-pole method to obtain equations for the pressure within an annular duct [79]. The derivation follows an analogous method as the hollow cylinder but necessitates the addition of recursion functions to solve the mode function based on Bessel functions of both the first and second type. The solutions for annular ducts can also be written with the related Hankel functions, where the Hankel functions of the first and second types are based on the Bessel functions as $H_n^1 = J_n(z) + iY_n(z)$ and $H_n^2 = J_n(z) - iY_n(z)$, respectively (Kurosaka, personal correspondence). This is a convenient formulation because then the Hankel function of the first type, H_n^1, refers to radially outward propagating waves while the second type, H_n^2, refers to radially inward propagating waves.

For the purposes of this analysis, however, it is enough to find that the solutions of Eq. 3.13 in an annular duct are then

$$f_{mnq} = \frac{a}{2}\sqrt{\left(\frac{\kappa_{m,n}}{\pi}\right)^2 + \left(\frac{q}{L}\right)^2} \tag{3.21}$$

where f is in radians/second (Hz) and $\kappa_{m,n}$ is the m^{th} root of the recursion relation $J_n'(a\kappa)Y_n'(b\kappa) - J_n'(b\kappa)Y_n'(a\kappa) = 0$, where a, b are the precursors of the constants A_n, B_n in the mode function.

Note that the annular configuration will contain Bessel functions of both the first and second kind, whereas the hollow configuration will have only a Bessel function of the first kind. This is due to the fact that the hollow configuration includes the origin (as the center of the combustor), but the second Bessel function has a singularity at the origin. By necessity, then, $B_n = 0$ in the hollow configuration, and the mode function for hollow ducts is solved as $R(r) = A_n J_n(\alpha\pi)$. Additionally, note that in the hollow duct, the radial term is $\frac{\alpha_{m,n}}{r}$ whereas in the annular duct, it becomes $\frac{\kappa_{m,n}}{\pi}$. Solving for $\alpha_{m,n}$ as defined above actually necessitates dividing by π (due to the solution of $\xi = n\pi$) to find the correct values of $\alpha_{m,n}$, while using a slightly varied definition will result in the hollow duct radial term becoming $\frac{\alpha_{m,n}}{\pi \times r}$. This is further discussed in the following subsection.

§3.2.2.1 Corrections to the frequency equations

In the above equations, m is the radial mode number, n is the tangential mode number and q is the longitudinal mode number. The notation for the modes unfortunately varies widely in the literature. The above assignment is used in Barrere, while Shimokuri and Morse and Feshbach have m and n reversed [75, 77, 80]. In contrast, Kim permutes m and q, leading with q as the radial mode and ending with m as the longitudinal mode [79]. The terminology for α_{mn} is also not fully standardized; in sources such as Bluemner and Pritschau the root of the first Bessel function is labeled $s_{\nu\eta}$, where $\alpha_{m,n} = s_{\nu\eta}/\pi$ by definition, leading to an extra factor of π^{-1} in the frequency equations [6, 31]. The sources that published full or partial tables for their respective Bessel roots and/or calculated frequencies were most helpful in verifying the code calculations, and are cited here for completeness: [6, 14, 31, 73, 75, 77, 80].

Although longitudinal modes can be important in RDEs, as noted by Keller, they correspond primarily to the presence of counter-rotating waves or to “longitudinal explosions” (also called “pop-outs”, seen visibly as deflagration outside the engine; they may also be related to pulsing) within the engine rather than radial detonation wave fronts [81]. Longitudinal modes were found by Bluemner et al. to be maximized at a critical combustor length-to-perimeter ratio of 0.5, where the perimeter was measured for an annular engine [76]. For the 25.4 mm and 10 mm engines in this study the length-to-perimeter ratios are 0.32 and 0.62, respectively, although the length-to-perimeter ratio is likely a less important factor given that the RDEs here studied are primarily run in coreless operation. Additionally, pulsing in engine runs is primarily associated with very low mass flux rates and the presence of counter-rotating waves, or with outlet restrictions and high-frequency

(1–4 kHz) pulsed operation [76]. The RDEs operated at the University of Washington have outlet restrictions in the form of piping to the dump tank, but the diameter of the piping is large compared to the diameter of the RDEs, and thus cannot be considered an engine nozzle for the purposes of reflecting detonation waves (see Secs. §3.1.2 and §3.1.3 for more detail). For the hollow runs in this study, counter-propagating waves were never observed, and detonation wave numbers varied from 1–3, with steady axial pulsing observed on only one annular run with $\phi = 2.0$, $\dot{m} = 150$ kg/(m$^2 \cdot$ s) (low mass flux). On the average annular run, counter-propagating waves became more common for smaller annular gap size, while pulsing was considered atypical behavior [13]. It was concluded that for the bulk of the runs presented in this study longitudinal modes do not need to be taken into account; so, in the rest of the following analysis q is taken to be 0 (see [14]).

Additionally, Shimokuri et al. in their study on tubular flame burners found the need for a correction due to the open end of their experimental hollow tube [75]. The alternate derivation is found to be

$$f_{mnq} = \frac{a}{2\pi}\sqrt{\left(\frac{\alpha_{m,n}}{r}\right)^2 + \left(\frac{(2q-1)\pi}{2(L+\Delta L)}\right)^2} \tag{3.22}$$

where ΔL is the open-end correction term. However, the authors believed that the correction was somewhat inaccurate [75]. The inaccuracy may be due to a difference in the importance of the correction between radial and tangential modes; hence, for $m = 0$ modes (radial modes) the correction term is likely of greater importance than for tangential modes [82]. In order to investigate the need for the open-end correction, f_{mnq} was calculated for multiple values of a and ΔL, and the results compared to Eq. 3.20.

Within the work of this study, it was confirmed that the value of $\Delta L = 0$ (chosen by Ishihara et al.) produced significant discrepancies from Eq. 3.20, while $\Delta L = 0.6$ produced results with 0.003% of Eq. 3.20 results. Choosing $\Delta L = 0.534$ (recommended by one author) gave results that showed a consistent 27.5% difference across both H_2 and CH_4 results; however, the net effect of implementing the correction was to simply lower the predicted frequency values of f_{mnq} by that percentage.

Both Eqs. 3.22 and 3.20 were tested on the 10 mm database to check equation validity. On H_2-O_2 results, the corrected equation using $\Delta L = 0.534$ had the effect of placing experimental data for the $w = 1$ dataset about halfway between the predicted 2T and 1T modes and placing the $w = 2$ dataset on or above the predicted 3T mode. The results were much more clearly inaccurate on CH_4-O_2, since Eq. 3.20 correctly identifies the $w = 1$ dataset with the 1T mode while Eq. 3.22 predicts no modes overlapping the experimental data. Therefore, Eq. 3.20 was ultimately chosen for better alignment with the data and with previously established analysis methods in hollow RDEs.

§3.3 Initial Experimentation

For the 10 mm engine, the initial experiments were designed to be run with both hydrogen-oxygen (H_2-O_2) and methane-oxygen (CH_4-O_2), both hollow and with a 6 mm-diameter copper core to produce a 2 mm annular gap. However, it was found initially that the CH_4-O_2 propellant did not run in the annular configuration, whereas in the hollow configuration, the detonation wave was only sustainable in fuel-rich conditions. The H_2-O_2 annular case, in contrast, ran steadily, but the heat transfer to the inner core resulted in rapid erosion and/or ejection from the engine with each test run. Additional cores were fabricated out of molybdenum and later tungsten for better durability, but the erosion was still severe enough to render the cores useful single tests only. The bulk of the erosion appeared to occur at the end of the test, that is, after the experiment time of record. Data gained from those two series of tests are included in this analysis in Sec. §3.1.3, with the caveat that the data, especially for the H_2-O_2 case, may be limited in applicability due to the effects of core erosion.

Finally, data using a heated fuel line is shown in Sec. §4.1.5.5. The remaining data presented in this study is based on both hollow and annular runs with $0.2 \leq \phi \leq 1.9$ with both H_2-O_2 and CH_4-O_2 propellants.

For the 25.4 mm engine, initial experiments were run on CH_4-O_2 only with $0.2 \leq \phi \leq 2.8$ in hollow and annular configurations, as noted in Sec. §3.1.3.

This provides the following eight separate configurations run with a mix of propellants, as listed in Table 3.4.

Table 3.4: List of fuels, engine sizes and RDE configurations studied in this thesis, where HF refers to heated fuels and UF stands for unheated fuel. Unspecified (–) are by default unheated fuels.

10 mm RDE				25 mm RDE			
CH_4	CH_4	H_2	H_2	CH_4	CH_4	CH_4	CH_4
UF & HF	–	–	–	–	–	–	–
Hollow	2 mm gap	Hollow	2 mm gap	3 mm gap	5 mm gap	7 mm gap	Hollow

Chapter 4

Results

This chapter discusses the development of the MATLAB analysis script used to calculate the predicted transverse modes in hollow RDEs, including the choices and validation of input pressure and temperature, sound speed parameters and comparison of methodology. It includes the results from implementing the analysis on both the 10 mm and 25 mm RDEs in the hollow and annular configurations, with such points as finding the expected detonation wave spin speed, investigating trends in the resonance mode data, and conducting a temperature sweep in the hollow engine results to verify initial parameter values. Finally, it discusses (section-by-section) the results for each RDE configuration studied.

The characteristic average sound speed in the RDE was taken to be the speed of sound of the pre-detonation wave gaseous mixture (i.e. uncombusted propellant mixture). This represents a departure from the typical input value of the speed of sound of the combustion products at the sonic wave behind the shock wave, i.e. in simpler terms, the sound speed of the post-detonative combusted mixture. However, choosing the sound speed of the incoming, pre-detonation propellant (a) was validated by comparison to the input values of the C-J detonation speed (D_{CJ}) and the C-J sound speed (a_{CJ}) [71, 83]. Ultimately, incoming propellant sound speed was chosen due to it producing closest match to the experimental frequency results; thus a was used at the primary input value in the bulk of the analysis. All speeds were computed using NASA CEA with a range of experimental chamber pressures $p = 1 - 10$ bar, equivalence ratios of $\phi = 0.2 - 1.9$ or $\phi = 0.2 - 2.9$, depending on the engine size, and the estimated initial temperature T. Based on the work of Knowlen et al., the propellant was considered pre-heated (that is, heated above room temperature of approximately 300 K) in the combustion chamber prior to detonation, and therefore the initial propellant temperature was set at $T = 1000$ K, and the initial pressure was set at $p = 3$ bar; see Sec. §4.1.2 and §4.1.3 for more details [61].

§4.1 Acoustic Analysis in Hollow RDEs

This section discusses the analysis carried out in the hollow configurations of 10 mm and 25 mm in diameter, using either methane (CH_4) or hydrogen (H_2) fuels with gaseous oxygen O_2.

§4.1.1 Frequency Determination

Acoustics may occur in tandem with the unburned propellant (reactant) as well as in the combustion products before it exits the engine. To answer the question of which sound speed to use, reactant and product sound speed frequency outputs across a range of resonant transverse modes were compared with the available experimental databases. The data was produced as discussed in Sec. §2.2.1.

The results from those calculations are discussed section-by-section by engine size and propellant combination, such as in Fig. 4.1. Based on the results from those comparisons as well as additional tests using a_{CJ} as the input sound speed (see Fig. 4.30), reactant sound speed values were chosen because the slope of their velocity-equivalence ratio curves and frequency-equivalence ratio curves were closest to that of the plotted experimental frequency data.

§4.1.2 Temperature Determination

Acoustic resonance frequencies in annuli and cylinders vary strongly with sound speed, which in turn is strongly dependent on the average temperature of the gas mixture. Unfortunately, in an RDE in particular, measuring the temperature of the mixed, unburned propellant immediately before the detonation wave is expensive, although it has been done before in a 154 mm (diameter) RDE [61]. The detonation wave itself presents a steep temperature gradient passing a given point at very high frequencies, resulting in instrument failure due to probe tip melting [61]. Some have taken the incoming propellant temperature to be at or near room temperature of $T = 300$ K based on the temperature of the propellants at the injector face [14, 31]; however, this approach does not account for propellant mixing with residual (heated) post-detonative products near the injectors, nor the pre-heating from oblique shock waves (which originate from the detonation zone) sweeping through the mixture. In fact, previous results found that using these methods, the frequency calculations at a given mode number did not simultaneously match the visually observed modes and the experimentally obtained engine frequency. Thus even if a predicted frequency matched the experimental frequency, the mode number(s) did not match the observed number of detonation waves in the engine. The same held vice versa: for an observed single detonation wave, the frequency calculated at the first tangential mode was inconsistent with the experimental frequency (Durkee, personal communication). Determining an accurate estimation of the incoming propellant temperature immediately before the detonation wave passage is thus critical to obtaining the correct wave spin frequencies and matching acoustic modes using this analysis.

To study these effects, Washington et al. measured the temperature of the propellants (CH_4-O_2) ahead of the detonation zone of an RDE with an outer diameter of 154 mm, annular gap width of 11.4 mm, with mass fluxes of 10, 20, and 30 kg/($m^2\cdot$ s). Importantly, it was found that the actual temperature of the reacting propellants at the base of the detonation wave was consistently above 1000 K (between 1200–1400 K) for the operating conditions of the engine tested. Additionally, it was found that the detonation wave has a stand-off distance axially downstream from the injector face which decreases with increasing mass flux [61]. The standoff distance was non-dimensionalized as the axial distance z of the instrument measurement (by insertion of the thermocouple into the engine from the injector faceplate) over the height of the annular gap h, that is, z/h (mm/mm). The base of the detonation wave was then found by thermocouple failure at z/h = 1.5–3.5. Increasing z/h (by decreasing mass flux) was associated with higher pre-wave propellant temperature, so at 10 kg/($m^2\cdot$ s), $z/h \approx 3.5$ and the associated temperature T_f at thermocouple failure, i.e., the detonation wave base, was $T_f = 1400$ K. For comparison, at 30 kg/($m^2\cdot$ s), it was found that $z/h \approx 1.7$ and $T_f = 1300$ K.

In this study, mass fluxes ranged from 160–400 kg/($m^2\cdot$ s) at $\phi = 1.15$ for the 25.4 mm annular engine [21] with gap widths of 3 mm, 5 mm and 7 mm. Correspondingly, $z/h = 8.4$ mm, 5 mm, and 3.6 mm for those gap widths, respectively. By analogy to the larger annular RDE studied above, the z/h values are sufficiently higher in the annular 25.4 mm configuration ($[z/h]_{25.4} > [z/h]_{154}$), so that despite the smaller sizing and higher mass fluxes, an approximate value for pre-detonation wave equilibrium temperature of $T = 1000$ K holds as a reasonable test case.

Applying similar logic to the hollow case is not as straightforward as the annular case,

Table 4.1: Stand-off detonation wave distances (z) from injector plate. Values for the 154 mm combustor are experimental; values for the 10 mm and 25.4 mm combustor are scaled to combustor length by percentages of axial distance.

RDE Dia.	Axial Length	Mass Flux	z, Stand-off Dist.	Axial Length Ratio
154 mm	177.8 mm	10 kg/($m^2\cdot$ s)	39.9 mm	22.5%
154 mm	177.8 mm	20 kg/($m^2\cdot$ s)	22.8 mm	12.5%
154 mm	177.8 mm	30 kg/($m^2\cdot$ s)	19.4 mm	10.9%
10 mm	20 mm	–	4.5 mm	22.5%
10 mm	20 mm	–	2.5 mm	12.5%
10 mm	20 mm	–	2.18 mm	10.9%
25.4 mm	25.4 mm	–	5.7 mm	22.5%
25.4 mm	25.4 mm	–	3.2 mm	12.5%
25.4 mm	25.4 mm	–	2.77 mm	10.9%

since as of yet, no similar studies have been performed to experimentally determine the detonation wave stand-off distance from a hollow RDE injector face. Nevertheless, it is strongly suspected that the stand-off distance is nontrivial, though it may be slightly smaller than the annular case since the hollow center potentially allows for faster mixing [24]. Hence, the incoming propellant has more time to be preheated by the previous reactants before it is consumed by the detonation wave.

As an initial check to validate whether a high initial temperature of $T = 1000$ K would be considered reasonable in the hollow configurations considered here, a comparison using relative combustor lengths is carried out below.

For the 10 mm hollow configuration, the mass flux was varied between 80–385 kg/($m^2\cdot$ s), and in the 25 mm hollow engine, mass flux was varied between 80–505 kg/($m^2\cdot$ s). Axial stand-off distance calculated for the 154 mm annular engines was $z \approx 19.4$ mm for 30 kg/($m^2\cdot$ s), $z = 22.8$ mm for 20 kg/($m^2\cdot$ s) and $z = 40$ mm for 10 kg/($m^2\cdot$ s). Representing z as a percentage of the total axial combustor length gives Table 4.1 for mass flux and z, with proportional z calculated for the 10 mm and 25 mm RDEs also.

While axial combustor length is admittedly not the most pertinent of parameters governing detonation wave operation, the z values calculated above are in surprisingly good correlation to experimentally determined propellant fill height in the 25.4 mm engine, with a range of approximately $z = 5.5$–3.5 mm [67]. Propellant fill height, by definition, is the axial distance from the injector front plate to which the injected propellant rises before the onset of the propagating detonation wave. Since the finite height of the propellant fill layer allows for non-premixed propellants to equilibrate and mix, thus enhancing fuel burning efficiency, it was deemed reasonable to take these stand-off distances as approximately correct, implying that there is indeed sufficient time for incoming propellant to be heated to at least $T = 1000$ K before it is consumed by the passing detonation waves. Hence, $T = 1000$ K was the temperature used in calculating the sound speed a in the unreacted propellant.

As a referential check, a_{CJ} values (note: this is post-detonation sound speed) were computed from NASA CEA, using the reference temperatures $T = 300$ K for the newly injected propellant at approximately room temperature and $T = 1000$ K for the pre-heated propellant just before detonation. These results were run through the MATLAB code and the resulting frequencies compared. As expected, using $a|_{T=300}$ produced frequency results similar to Durkee, who chose $T \approx 300$ K based on the propellant temperature at the injector face, but the code output at $a|_{T=300}$ showed little correlation to the experimental data. Utilizing $a|_{T=1000}$, on the other hand, produced results more in line with experimental frequencies. This will be shown in the following results, in Secs. §3.1.2 and §3.1.3.

NASA CEA software was initially used to calculate a and a_{CJ} [84, 85]. However, since CEA is based on the ideal gas equation of state, an investigation was made using REFPROP as a software that incorporates real gas effects, and the resulting sound speeds compared for the same initial conditions [86]. Table 4.2 was created to calculate the percent difference of a between CEA and REFPROP, for CH_4-O_2 and H_2-O_2 at a range of equivalence ratio values ($\phi = 0.4$–1.4) (see Sec. §4.1.1 for why a was chosen as the sound speed of interest rather than a_{CJ}). Pre-detonation pressure was chosen as $p = 3$ bar (see Sec. §4.1.3 for discussion on input pressure), with initial temperature T = 1000 K.

Table 4.2: Values a calculated NASA CEA and REFPROP, and standard deviation between values. ϕ and percentages are nondimensional; all other units are in m/s.

	CH_4-O_2			H_2-O_2		
	CEA	REFPROP	Deviation	CEA	REFPROP	Deviation
$\phi = 0.4$	595.6	596.4	0.13%	772.3	772.9	0.075%
$\phi = 0.8$	608.2	609.1	0.15%	910.6	911.2	0.065%
$\phi = 1.15$	618.5	619.5	0.16%	1008.0	1008.7	0.069%
$\phi = 1.8$	634.9	636	0.17%	1152.3	1153	0.061%

The deviation in Table 4.2, however, showed little difference between the calculated a values using CEA and REFPROP. The percent error was within 0.04% for a in methane across the range of ϕ, with marginal increases in error with increasing ϕ (i.e., fuel-rich conditions). For hydrogen, the error was yet smaller and stayed within a 0.014% range. This result is not entirely surprising, since real gas effects are expected to be significant with pressures above 20 bar. Therefore, it was determined that the software packages were equivalent for the purposes of this study, and CEA software was chosen as the primary source as is common in the literature [6, 14, 31].

§4.1.3 Pressure and Additional Variables

An exploration to choose the proper pressure values was undertaken, with the following steps taken. Based on previous experimental work, an initial (pre-detonation) pressure range of 1–10 bar was selected for verification of applicability. As one of the inputs needed to resolve the sound speed a_{CJ}, the initial pressure range was entered into NASA CEA for the conditions of interest (T = 1000 K, $\phi = 0.2$–1.9).

For T = 1000 K and ϕ = 0.2–1.9 in both H_2 and CH_4, the reactant sound speed varied little between p = 1–10 bar, whereas the a_{CJ} (product sound speed) values typically varied by no more than 20 m/s over that pressure range. For reference, a_{CJ} in H_2-O_2 is on the order of 1700–3200 m/s and in CH_4-O_2, $a_{\mathrm{CJ}} = 1600$–2600. Since the variation was less than a 2% difference in all cases, this was considered confirmation of pressure being a less important parameter than temperature, pre- or post-detonation sound speed choice, equivalence ratio or mass flux.

Additional research found that the experimental results for the 154 mm RDE shows that the initial pressure of the incoming propellant was around 4 bar [12, 27]. This is consistent with the annular injection pressure measured by Durkee for a 25 mm RDE, while for the hollow testing, injection pressure was measured to be $p = 2.8$ bar [14]. To check the dependence in the code output, input pressures of both 3 and 4 bar were used to compare values over the predicted transverse frequency range in hollow engines. It was found that for the operating conditions considered here, a pressure difference of 1 bar produced insignificant increases in the pre-detonation propellant sound speed, and thus had little effect on frequency output predictions. Therefore, the input pressure of $p = 3$ bar was taken as standard for both hollow and annular configurations to represent the likely post-injection, pre-detonation pressure at the base of the detonation wave.

While variations in sound speed values were small for the operating pressure inputs considered, variations in equivalence ratio ϕ contribute to significant variations in a_{CJ}. However, as mentioned in the section on UW studies, mass flux plays a large role in determining the number of detonation waves concurrently operating in the engine [12]. In fact, Cobb et al. found that mass flux is a more important parameter in engine performance than chamber pressure [87]. This may affect propellant velocity and/or temperature, leading to corresponding fluctuations in sound speed. However, mass flux can best be accounted for in the data for the 25 mm configurations due to the more extensive database of experimental results.

§4.1.4 10 mm RDE: H_2 Frequency Results and Discussion

This subsection summarizes the results of the code on the 10 mm, hydrogen-fueled hollow RDE.

§4.1.4.1 Wave spin speed vs. sound speed

Wave spin speeds in the RDEs were determined as the wave speed S with a dependence on resonance mode wavelength λ and frequency f as

$$S = \lambda \times f \tag{4.1}$$

In RDEs, the applicable λ is the outer circumference of the combustor, so that $\lambda = \pi \times d$, where d is the diameter of the combustor. Thus spin speed was calculated as

$$S = \pi \times d \times f \tag{4.2}$$

The frequency, f, was taken as the experimentally determined RDE operating frequency values, computed from the high-speed video and/or piezoelectric pressure sensor (PCB 113) data. The ideal gas sound speeds a and a_{CJ} were plotted alongside D_{CJ} and the experimental wave spin speeds. in Fig. 4.1. Average experimental frequencies across a wide range of equivalence ratios and mass fluxes were approximately 92 kHz, 135–145 kHz and 167 kHz, as shown; these correspond to wave counts of $w = 1$, $w = 2$ and $w = 3$, which appear as three distinct groups of data on the figure.

These data are more or less in tune with the predicted detonation velocity for $\phi =$ 1.1–1.4. As is notable throughout these results, experimental spin speeds do not show

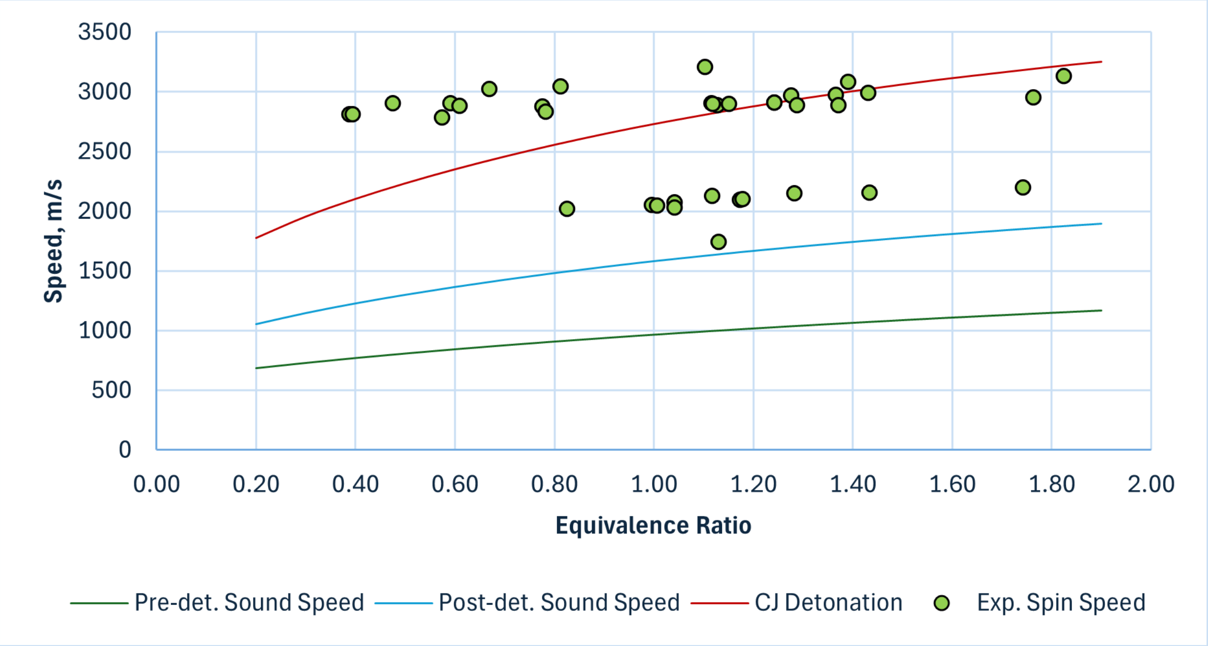

Figure 4.1: Ideal product (Post-det.) sound and detonation speeds, a_{CJ} and D_{CJ}, plotted alongside reactant (Pre-det.) sound speed and experimentally determined wave spin speed, for H_2-O_2 in the 10 mm coreless RDE.

a strong dependence on ϕ, unlike the idealized C-J property curves plotted in Fig. 4.1. Additionally, the $w = 1$ group (where w is the detonation wave number, corresponding at $w = 1$ to one-wave RDE operation), with spin speeds of approximately 2800 m/s, shows close correlation to the C-J detonation velocity, while for $w = 2$ and $w = 3$, the wave spin speed is significantly less than the idealized 1-D model prediction.

Fig. 4.2 shows comparison of the detonation wave speed vs. experimental wave spin speed using $p = 1$ bar with callouts for the average frequency per wave group. The detonation velocity curve has a faster rate of increase at the lower pressure value, thus passing through fewer of the experimental data points. Also, it is worth pointing out that as frequency increases, the wave speed decreases due to the shorter propellant fill height between passes of the detonation wave. This phenomenon is by now well-established in the literature, for example in [59].

It is notable that while the ideal gas sound speed (both reactant and product) and

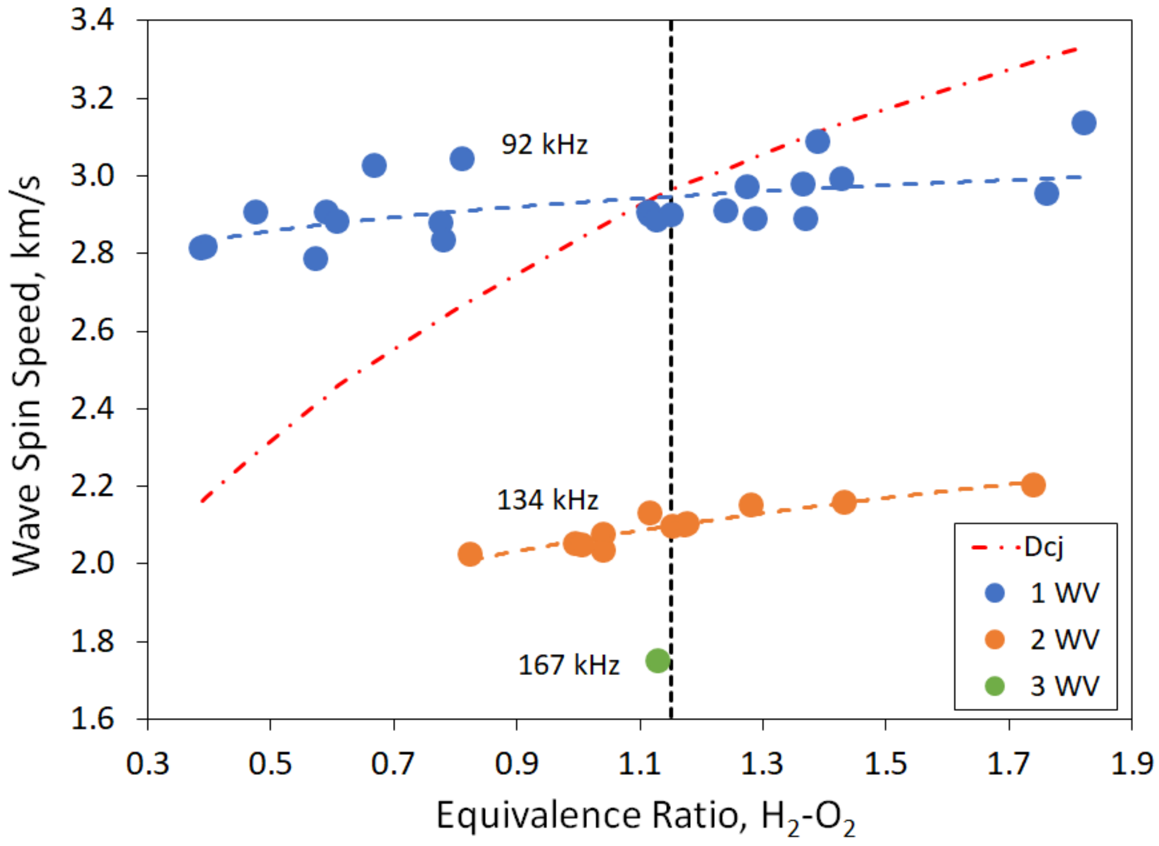

Figure 4.2: Experimental ϕ vs. calculated spin speed on the hollow 10 mm RDE, H_2-O_2.

detonation velocity are predicted to increase as the equivalence ratio is raised, experimental results vary little over the range of ϕ. This is may be due to the effects of the small radius of curvature, the diatomic hydrogen structure of the fuel molecules, and additional factors at play that may have a stabilizing effect on the variability of the wave speed and frequency.

§4.1.4.2 Trend lines and expected base frequencies

In contrast to the previous section, Fig. 4.3 shows the expected fundamental engine frequency (the "Injector Base" line), calculated with the shock-heated reactant sound speed divided by injector impingement circumference, plotted alongside the first tangential mode (1T), the first radial mode (1R) and experimental frequencies with trend lines across a

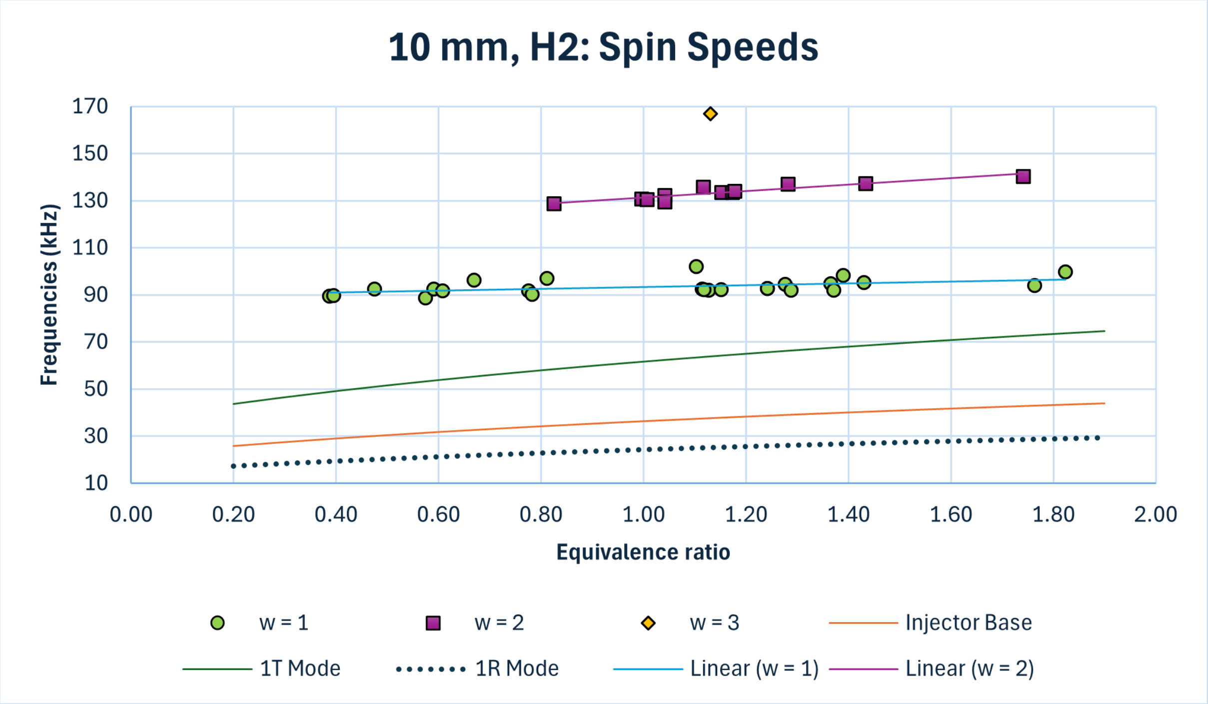

Figure 4.3: Minimum expected fundamental line (Injector Base), 1T and 1R mode frequencies alongside experimental data and corresponding trend lines for the $w = 1$ and $w = 2$ groups in the hollow 10 mm H_2-O_2 RDE.

range of ϕ. The slope of the trend lines clearly differs from the calculated sound speed slopes, with less dependence on equivalence ratio, as previously mentioned.

§4.1.4.3 Initial frequency results

Using the experimental data, and running the MATLAB script created, the transverse mode frequencies were computed starting with the 10 mm hollow RDE configuration. Initial frequency calculations across hollow engine cases were run using the following α_{mn} values, which were exhaustively compared to the values published in prior literature for accuracy (listed in Sec. §3.2.2.1). For the aid of developing the acoustic analysis field in RDEs, the full table of α_{mn} values is given below: It is important to distinguish between modes based on the α_{mn} values, lest the mode numbers become confusing. Throughout the rest of this analysis, the $m = 1, n = 0$ value is called the 1R mode, and pure radial modes (1R, 2R, 3R...) are taken as the $n = 0$ row, across; pure tangential modes (1T,

Table 4.3: α_{mn} values for radial modes $m = 1 - 5$ and tangential modes $n = 0 - 4$.

	$m = 1$	$m = 2$	$m = 3$	$m = 4$	$m = 5$
$n = 0$	0.00	1.22	2.23	3.24	4.24
$n = 1$	0.59	1.70	2.71	3.73	4.73
$n = 2$	0.97	2.13	3.17	4.19	5.20
$n = 3$	1.34	2.55	3.61	4.64	5.66
$n = 4$	1.69	2.95	4.04	5.08	6.11

Table 4.4: Code results: H_2, hollow, 10 mm, $\phi = 0.8$, $T = 1000$ K. Here $m =$ radial modes are numbered across, $n =$ tangential modes are numbered down.

	$m = 1$	$m = 2$	$m = 3$	$m = 4$	$m = 5$
$n = 0$	22.8 kHz	113.4 kHz	204.6 kHz	295.8 kHz	386.9 kHz
$n = 1$	58.0 kHz	156.2 kHz	248.2 kHz	340.1 kHz	431.4 kHz
$n = 2$	91.4 kHz	195.7 kHz	289.9 kHz	382.4 kHz	474.4 kHz
$n = 3$	123.9 kHz	233.4 kHz	329.7 kHz	423.4 kHz	516.1 kHz
$n = 4$	155.8 kHz	270.0 kHz	368.3 kHz	463.3 kHz	556.9 kHz

Table 4.5: Code results: H_2, hollow, 10 mm, $\phi = 1.15$, $T = 1000$ K. Radial modes are numbered across, tangential modes are numbered down.

	$m = 1$	$m = 2$	$m = 3$	$m = 4$	$m = 5$
$n = 0$	25.2 kHz	125.5 kHz	226.5 kHz	327.4 kHz	428.2 kHz
$n = 1$	64.2 kHz	172.9 kHz	274.7 kHz	376.4 kHz	477.6 kHz
$n = 2$	101.2 kHz	216.6 kHz	320.9 kHz	423.3 kHz	525.1 kHz
$n = 3$	137.1 kHz	258.4 kHz	364.9 kHz	468.7 kHz	571.3 kHz
$n = 4$	172.5 kHz	298.9 kHz	407.7 kHz	512.8 kHz	616.4 kHz

2T, 3T...) are taken as the $m = 1$ column; and finally, the mixed modes are based on the $n \geq 1$, $m \geq 2$ matrix values. For example, the single-radial-component transverse modes of 1T1R, 2T1R, 3T1R and 4T1R are taken as the $m = 2, n = 1 - 4$ column values.

Having calculated the Bessel function roots as given in Table 4.3, the following tables (Tables 4.4, 4.5, 4.6) are example outputs for the frequency calculation.

Graphed in Fig. 4.4 are the initial results for multiple modes and the experimental

Table 4.6: Code results: H_2, hollow, 10 mm, $\phi = 1.6$, $T = 1000$ K. Radial modes are numbered across, tangential modes are numbered down.

	$m = 1$	$m = 2$	$m = 3$	$m = 4$	$m = 5$
$n = 0$	27.8 kHz	138.5 kHz	249.9 kHz	361.2 kHz	472.4 kHz
$n = 1$	70.9 kHz	190.7 kHz	303.1 kHz	415.3 kHz	526.8 kHz
$n = 2$	111.6 kHz	239.0 kHz	354.0 kHz	467.0 kHz	579.3 kHz
$n = 3$	151.3 kHz	285.1 kHz	402.6 kHz	517.0 kHz	630.3 kHz
$n = 4$	190.3 kHz	329.7 kHz	449.8 kHz	565.7 kHz	680.0 kHz

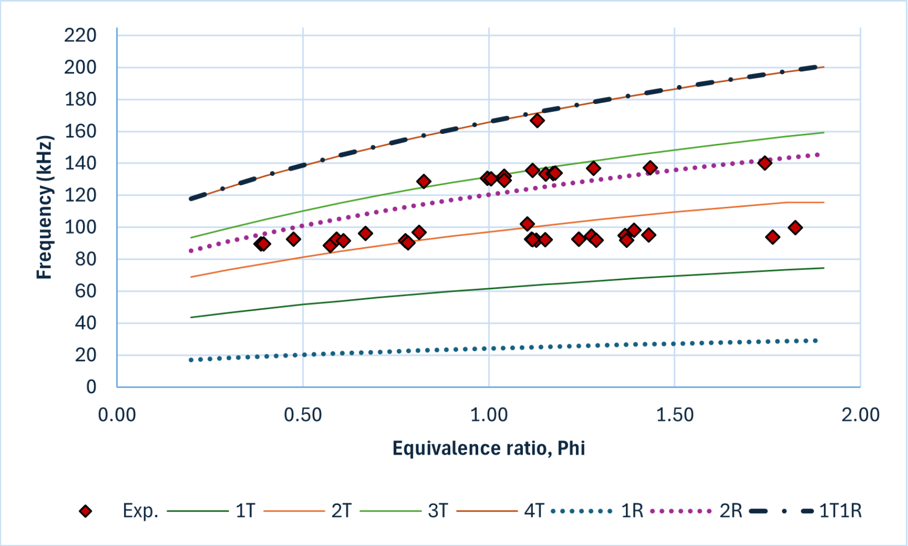

Figure 4.4: Frequency results across a range of modes, phi and experimental data in the 10 mm H_2-O_2 hollow RDE.

data at $T = 1000$ K. As you can see, the lowest line of 1T is not shown to closely match the experimental frequencies; however, the experimental data plotted here is the wave spin frequency data as calculated from the high-speed video data. In fact, the lowest operating frequencies revealed on the spectrogram results (as in Figs. 4.5, 4.7, 4.9) show much closer correlations to the 1R mode, the 1T mode and/or harmonic multiples of those numbers, as noted in Sec. §4.1.5.4.

The experimental data lay in three roughly similar frequency groups with wave numbers $w = 1$–3. The $w = 1$ group has an average frequency of 92 kHz, $n = 2$ averages around 135 kHz, and the singular $w = 3$ point was at 167 kHz. The experimental data graphed here include frequency trend lines, which as noted above, do not linearly increase with ϕ as predicted by the idealized frequency lines. As seen in Fig. 4.4, the middle group of experimental data points ($w = 2$, with frequencies around 135 kHz) in this picture aligns most closely with the 2R/3T mode, while the $w = 3$ point lies almost on the 4T/1T1R mode. While this seems to have the same problem as found by Durkee, that the predicted frequencies do not match the visible modes, further investigation shows that a higher initial

Table 4.7: 10 mm, H_2: approximate multiples of the 1R mode across the equivalence ratio sweep of $0.2 \leq \phi \leq 1.8$ and the remainder (based on deviation from the calculated transverse mode frequencies), alongside the standard deviation of the remainder across the ϕ sweep.

	Multiple of 1R	Remainder	Rem. standard dev.
1T	2.5	0.8 – 1.4 kHz	0.27
2T	4	0.3 – 1.5 kHz	0.44
3T	5.5	1 – 1.7 kHz	0.21
4T	7	2.7 – 4.6 kHz	0.56
1R	5	0.3 – 0.6 kHz	0.07
1T1R	7	2.4 – 4.1 kHz	0.50

temperature yields more reasonable results such that the $w = 2$, $w = 3$ wave count groups align with the 2T/2R and 3T modes, respectively. Sec. §4.1.2 shows the temperature sweep conducted and predicts an initial temperature of $T = 1400$ in the 10 mm, H_2-O_2 case. That said, even this initial result agrees with the conclusion made by Durkee that hollow RDEs promote radial modes (and perhaps also mixed radial-tangential modes) rather than purely tangential modes [14].

Significantly, the 1R mode exhibits two important properties. First, it has a shallower slope (closer to the median slope of the experimental values by wave group $w = 1, 2, 3$) than higher transverse modes. Secondly, the 1R mode is an approximate integer or fractional multiple of all the other transverse modes. Since acoustic modes can be combined in superposition, this effectively means that the 1R mode may act as a fundamental frequency enabling tangential-based (spinning) detonation waves to propagate through the hollow cylinder.

The following table was therefore created to study the possible multiples of the 1R mode, Table 4.7.

The remainder listed in Table 4.7 is what is left over from multiplying the 1R mode by the stated multiple and subtracting the result from the calculated frequencies of the lefthand column. This remainder was calculated across a sweep of ϕ and rounded to the range given (in kHz) while the standard deviation in remainders across ϕ values is shown in the rightmost column.

§4.1.4.4 Experimental data: spectrograms

The following three experimental data points are identified by run numbers 53, 55, and 60. Run 53 had a mass flux of 167 kg/(m^2· s), $\phi = 1.823$, and recorded wave frequency 99.79 kHz. Run 55 had a mass flux of 171.9 kg/(m^2· s), $\phi = 1.007$, and recorded wave frequency 130.4 kHz. Both of these waves have one recorded wave ($w = 1$) during the experiment time of record. Finally, Run 60 had a mass flux of 276.5 kg/(m^2· s), $\phi = 1.178$, and recorded wave frequency 133.9 kHz, with $w = 2$. The wave frequencies listed here were measured by the high-speed video data; thus, they correspond to the highest average wave spin frequency associated with the detonation wave.

Spectrograms from these three runs are shown in Figs. 4.5, 4.7, 4.9, and the corresponding power spikes recorded by the high-speed data are shown in Figs. 4.6, 4.8, 4.10. The spectrograms are compilations of a Fast-Fourier Transform (FFT) process. The FFT process creates additional high-frequency spikes at multiples of the strongest frequencies, and while the higher spikes may not be physical, lower spikes at resonance mode values can co-exist alongside the strongest frequencies. These figures clearly show that, while the the average engine operation wave frequencies recorded by the high-speed camera were on the spectrograms, lower base frequencies also exist as shown here which are likely physical pressure waves in the combustor given their correspondence to the predicted transverse frequencies. Thus underlying harmonics are clearly at play in RDE operation.

Example code outputs for $\phi = 0.8, 1.15, 1.6$, $T = 1000$ K and $p = 3$ bar are shown in Tables 4.4, 4.5, and 4.6, respectively. It is interesting to note that the $m = 1$, $n = 0$ mode (where again m is the radial mode, n is the tangential mode) has a predicted frequency of

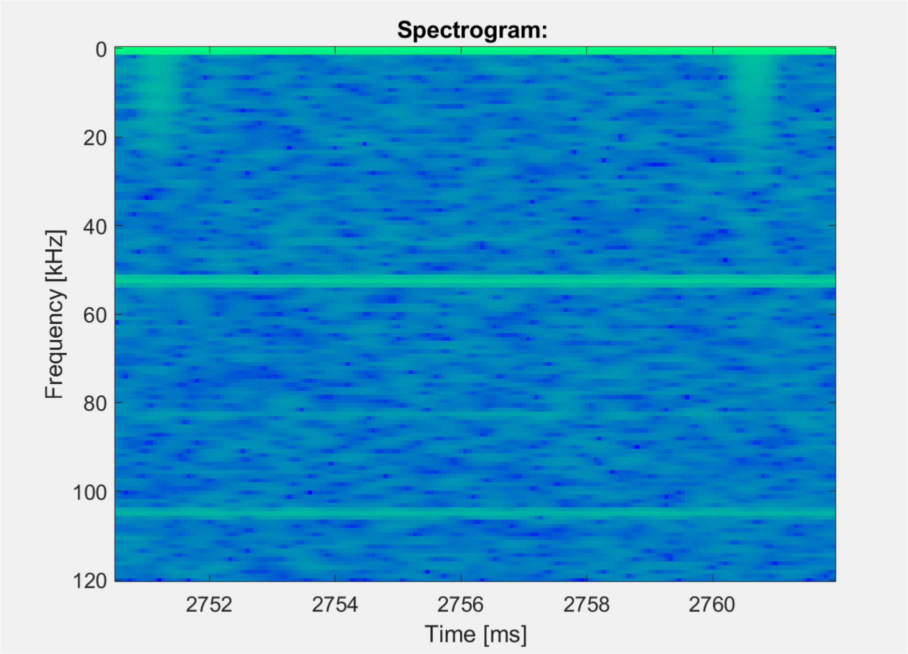

Figure 4.5: Run 53 spectrogram ($\phi = 1.823$, H_2). Frequencies shown are approximately 57, 83, and 105 kHz, respectively, with the line at 83 kHz being the weakest.

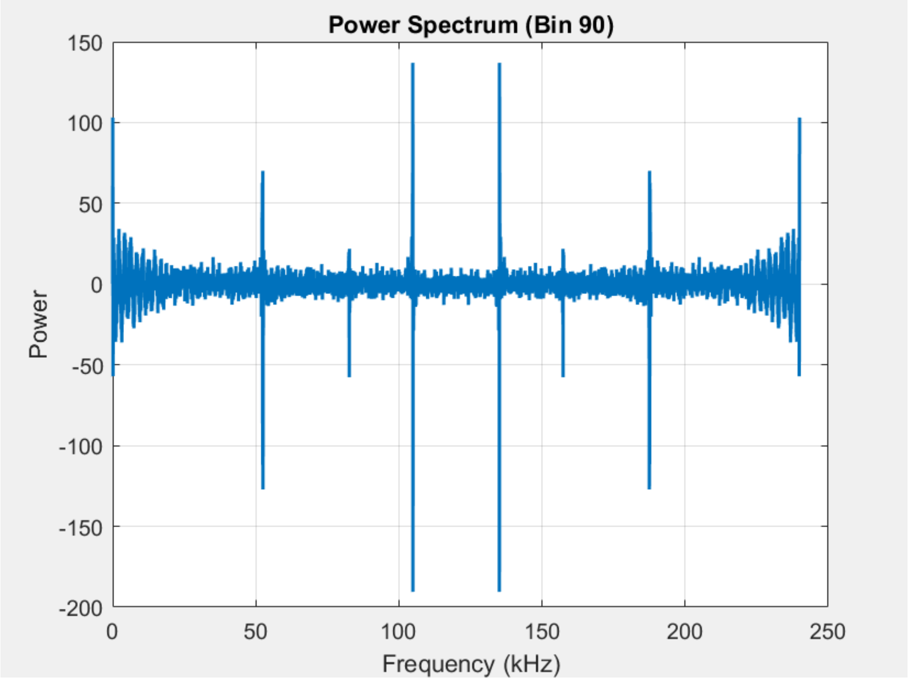

Figure 4.6: Run 53 power spikes ($\phi = 1.823$, H_2). Frequencies shown are approximately 52, 83, and 105 kHz, respectively; above 120 kHz, the image is mirrored due to the data processing technique.

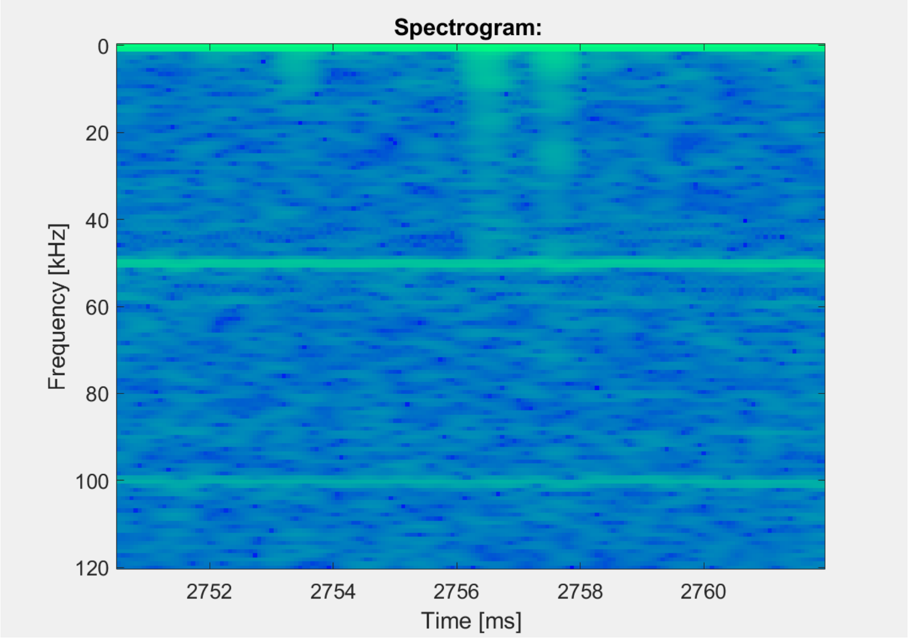

Figure 4.7: Run 55 spectrogram ($\phi = 1.007$). Frequencies shown are approximately 50-53 and 100 kHz.

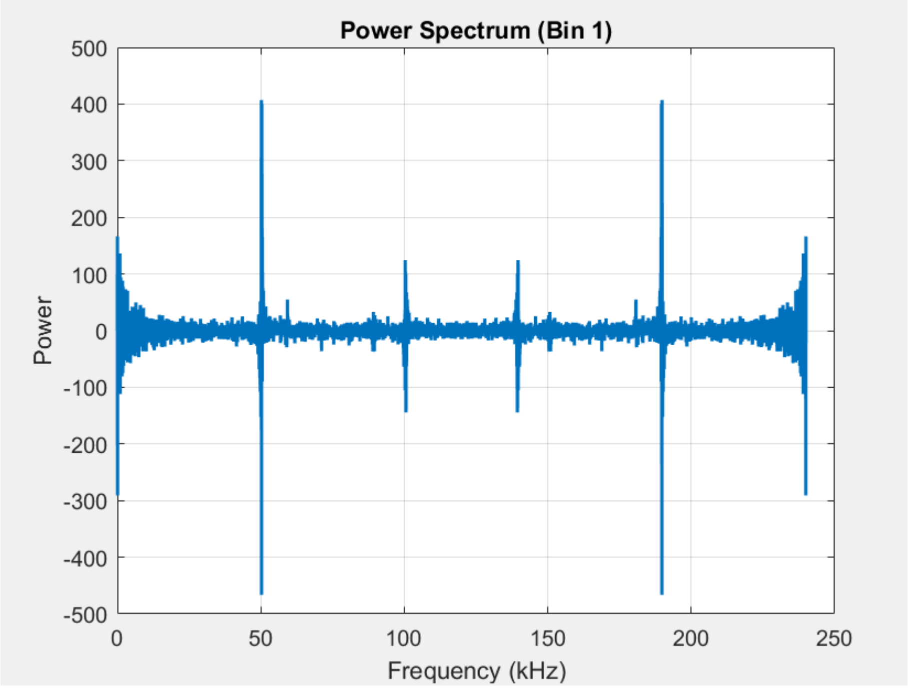

Figure 4.8: Run 55 power spikes ($\phi = 1.007$). Frequencies shown are approximately 50 and 100 kHz; as before, above 120 kHz the image is mirrored.

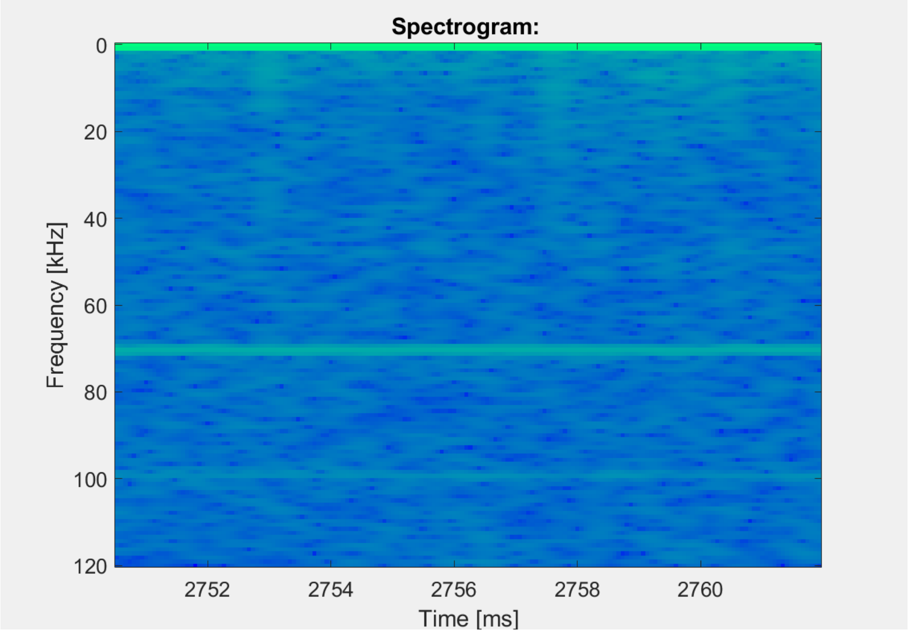

Figure 4.9: Run 60 spectrogram ($\phi = 1.178$). Frequencies shown are approximately 72 and 98 kHz.

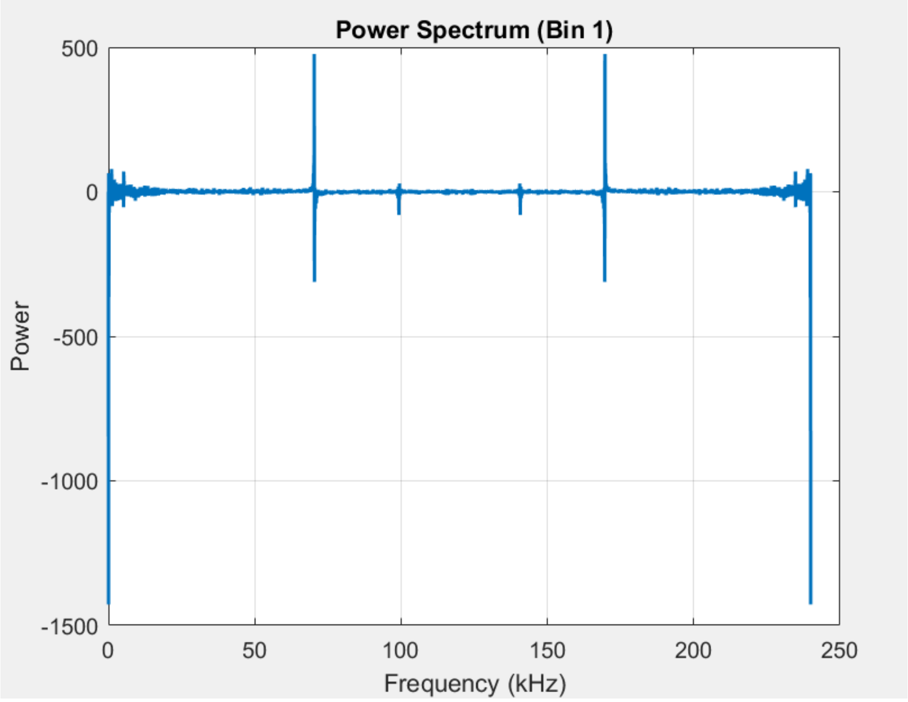

Figure 4.10: Run 60 power spikes ($\phi = 1.178$). Frequencies shown are approximately 72-74 and 98 kHz; above 120 kHz the image is mirrored.

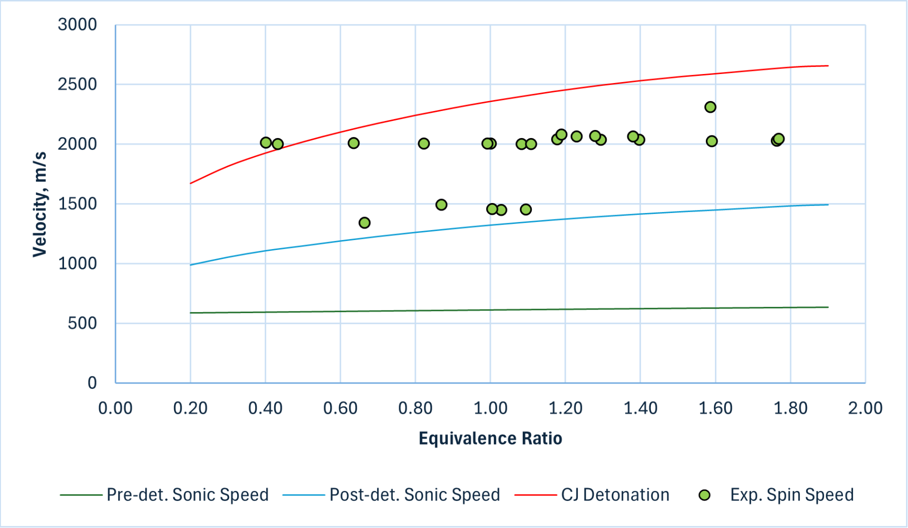

Figure 4.11: 10mm, CH_4; Experimental data vs. ideal sound speeds and detonation velocity.

about 55 kHz, which is remarkably aligned with the lowest frequency lines captured on the spectrograms for Runs 53 and 55 (Figs. 4.5, 4.7). This is despite the disagreement in the literature about the meaning and importance of what is in fact the 1R mode, which depending on calculation methods appears to have been misunderstood in some literature (see [6, 31] for more discussion); this may be due to the fact that it is calculated with $n = 0$, $m = 1$ as $\alpha_{m=1,n=0} = 0$. This α_{mn} is shown also in Shimokuri et al. and textbooks such as Methods of Theoretical Physics [75, 80]. More on this is found in Sections §4.1.4.3, §4.1.5.3, §4.1.6.3.

§4.1.5 10 mm RDE: CH_4 Frequency Results and Discussion

§4.1.5.1 Wave spin speed vs. sound speed

Similar to the previous section, the propellant sound speed and detonation velocities in methane are shown in Fig. 4.11.

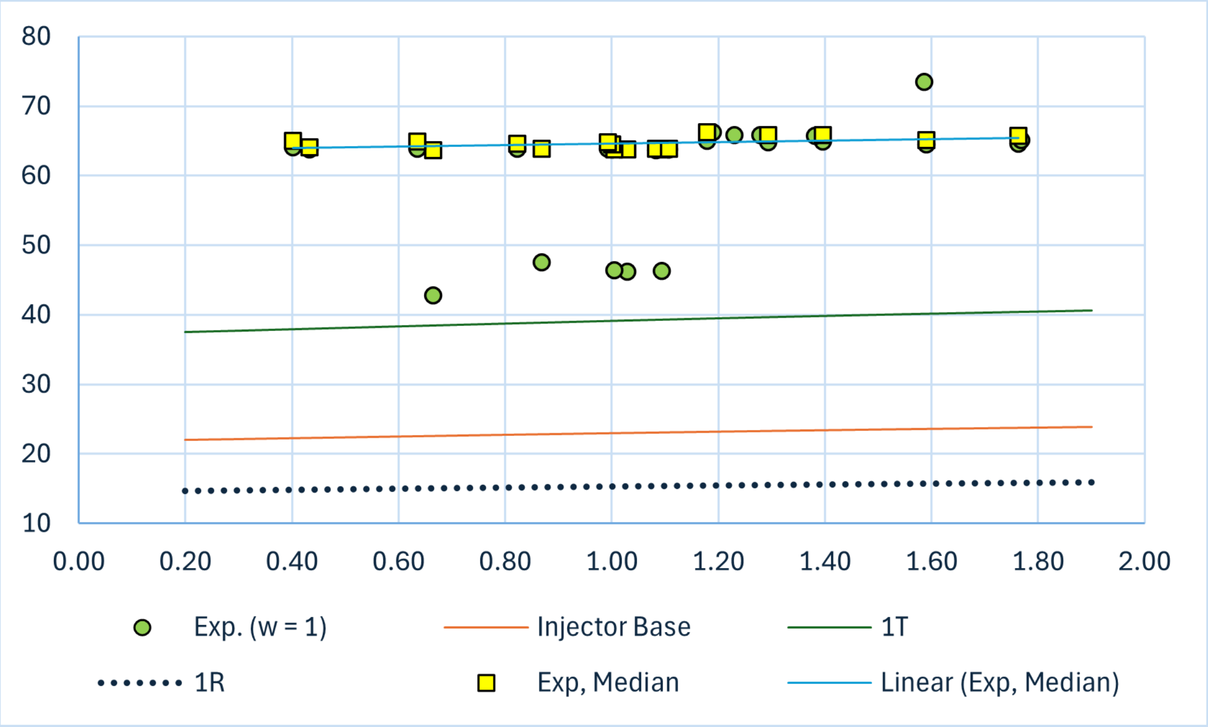

Figure 4.12: Trend line of median experimental data frequencies compared to predicted 1R mode, 1T, and expected baseline in the hollow 10 mm RDE, CH_4-O_2.

§4.1.5.2 Trend lines and expected base frequencies

For methane, plotting the trendlines and expected baseline values was a bit trickier than in the 10 mm H_2 case. The baseline was again taken to be the reactant sound speed at $T = 1000$ K divided by injector ring circumference. However, while only one wave was seen in this dataset, experimental frequencies appear on what appear to be two different linear trends. Thus, taking the trend line has been modified to only account for the median experimental values, for comparison to the slope of the predicted values. Fig. 4.12 shows that the median values' trend line has a slope much closer to the predicted frequency slopes compared to hydrogen. The additional data points close to the 1T line show unexpectedly low frequency values, that interestingly are an approximate multiple of the 1R mode. More discussion on this will be presented in Sec. §4.1.5.3.

Table 4.8: Code results: CH_4, hollow, 10 mm, $\phi = 0.8$, $T = 1000$ K. m = radial modes are numbered across, n = tangential modes are numbered down.

	$m = 1$	$m = 2$	$m = 3$	$m = 4$	$m = 5$
$n = 0$	15.5 kHz	77.0 kHz	137 kHz	198 kHz	258 kHz
$n = 1$	39.4 kHz	104 kHz	166 kHz	227 kHz	288 kHz
$n = 2$	62.1 kHz	131 kHz	194 kHz	255 kHz	317 kHz
$n = 3$	84.1 kHz	156 kHz	220 kHz	283 kHz	345 kHz
$n = 4$	106 kHz	180 kHz	246 kHz	309 kHz	372 kHz

Table 4.9: Code results: CH_4, hollow, 10 mm, $\phi = 1.15$, $T = 1000$ K. Radial modes are numbered across, tangential modes are numbered down.

	$m = 1$	$m = 2$	$m = 3$	$m = 4$	$m = 5$
$n = 0$	15.5 kHz	77.0 kHz	139 kHz	201 kHz	263 kHz
$n = 1$	39.4 kHz	106 kHz	169 kHz	231 kHz	293 kHz
$n = 2$	62.1 kHz	133 kHz	197 kHz	260 kHz	322 kHz
$n = 3$	84.1 kHz	159 kHz	224 kHz	288 kHz	351 kHz
$n = 4$	106 kHz	183 kHz	250 kHz	315 kHz	378 kHz

Table 4.10: Code results: CH_4, hollow, 10 mm, $\phi = 1.6$, $T = 1000$ K. Radial modes are numbered across, tangential modes are numbered down.

	$m = 1$	$m = 2$	$m = 3$	$m = 4$	$m = 5$
$n = 0$	15.8 kHz	78.5 kHz	142 kHz	205 kHz	268 kHz
$n = 1$	40.2 kHz	108 kHz	172 kHz	235 kHz	299 kHz
$n = 2$	63.3 kHz	135 kHz	201 kHz	265 kHz	328 kHz
$n = 3$	85.7 kHz	162 kHz	228 kHz	293 kHz	357 kHz
$n = 4$	108 kHz	187 kHz	255 kHz	321 kHz	385 kHz

§4.1.5.3 Initial frequency results

Again for the sake of developing the field of acoustic analysis, tables of results for the 10 mm RDE run on methane fuel are shown as Tables 4.8, 4.9, 4.10:

The code corresponds extremely well with the experimental data for the 1T mode. The experimental data had $w = 1$ exclusively, and as seen in Fig. 4.13, operating frequencies closely align with the predicted 1T mode for some of the runs. However, for the majority of the runs the engine appears to be operating at frequencies about halfway between the predicted 1T and 2T mode frequencies.

Continuing on the thread from Sec. §4.1.4.3, a table of values for multiples of the 1R mode was computed using the same methods as described. It is striking that the same

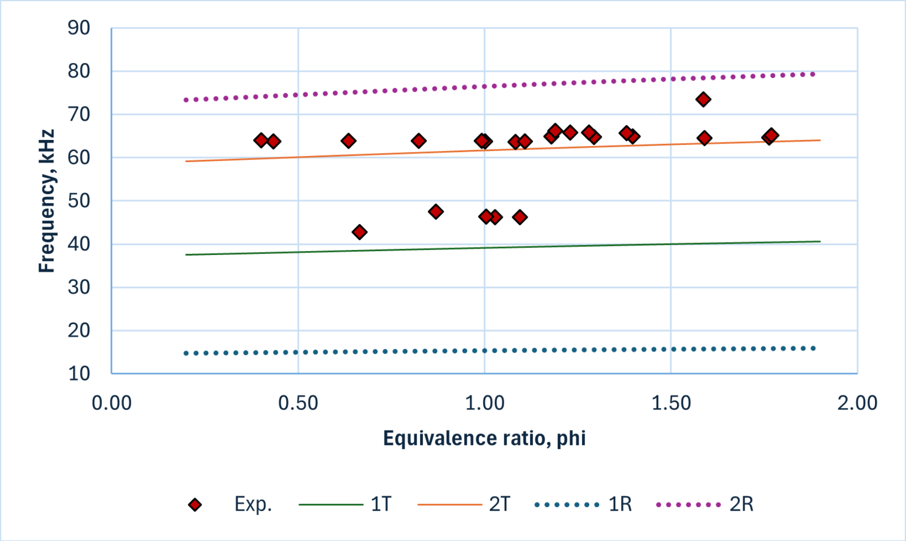

Figure 4.13: CH_4, 10mm; transverse mode frequencies vs. experimental data.

Table 4.11: 10 mm, CH_4: approximate multiples of the 1R mode across the equivalence ratio sweep of $0.2 \leq \phi \leq 1.8$ and the remainder (based on deviation from the calculated transverse mode frequencies), alongside the standard deviation of the remainder across the ϕ sweep.

	Multiple of 1R	Remainder	Rem. standard dev.
1T	2.5	0.7 – 0.8 kHz	1.7×10^{-2}
2T	4	0.2 kHz	0.5×10^{-2}
3T	5.5	0.8 – 0.9 kHz	2×10^{-2}
1R	5	0.3 kHz	0.7×10^{-2}
1T1R	7	2.0 – 2.2 kHz	4.8×10^{-2}
4T	7	2.3 – 2.5 kHz	5.3×10^{-2}

multiples of the 1R mode hold for both methane and hydrogen fuels in the 10 mm RDE, pointing to a property of the RDE sizing itself. Methane is of course more stable and hence has much smaller standard deviations from the remainder, as seen in Table 4.11; see also Sec. §4.1.6.3 for the 25 mm table.

§4.1.5.4 Experimental data: spectrograms

The following three experimental data points for methane in the 10 mm RDE are identified by run numbers 22, 59, and 144. Run 22 had a mass flux of 246 kg/(m$^2\cdot$ s), $\phi = 1.17$, and recorded wave frequency 61.45 kHz. Run 59 had a mass flux of 236 kg/(m$^2\cdot$ s), $\phi = 1.4$, and recorded wave frequency 65.01 kHz. Finally, Run 144 had a mass flux of 249 kg/(m$^2\cdot$

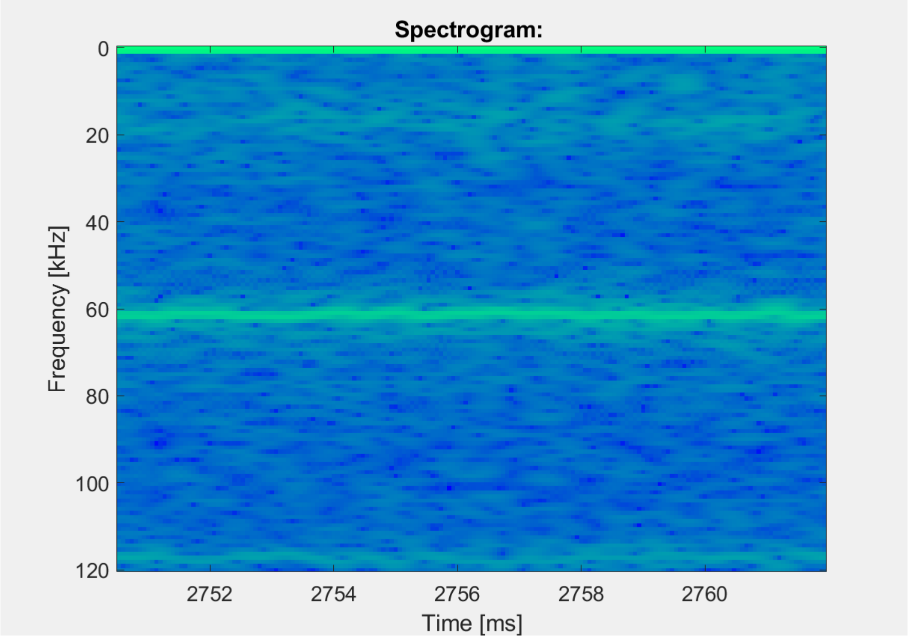

Figure 4.14: Run 22 spectrogram ($\phi = 1.17$, 10 mm RDE, CH_4-0_2). Frequencies shown are approximately 19 kHz (faint), 61 kHz and 118 kHz.

s), $\phi = 1.15$, and recorded wave frequency 59.66 kHz. All of these waves have one recorded wave ($w = 1$) during the experiment time of record. Again, the wave frequencies listed above were determined from the high-speed video data and correspond to the average frequency of the spinning detonation wave.

Spectrograms from these three runs are shown in Figs. 4.14, 4.16, 4.18; the corresponding power spikes recorded by the high-speed data are shown in Figs. 4.15, 4.17, 4.19. The power spike frequencies again correspond closely with the predicted transverse frequencies, emphasizing the harmonics within RDEs. Examples of the correspondence between the experimental frequencies and transverse modes are given in these figures. For example, in Run 22 ($\phi = 1.17$), Run 59 ($\phi = 1.4$), and Run 144 ($\phi = 1.15$) the experimental frequencies are between 61-65 kHz; frequencies on this order are clearly seen on the spectrogram and power spike graphs (Figs. 4.14–4.19). This frequency range corresponds to the 2T line, seen in Fig. 4.13. Comparison of the remaining frequencies (seen on the figures) to the code results at $\phi = 1.15$ shows the following correlated points:

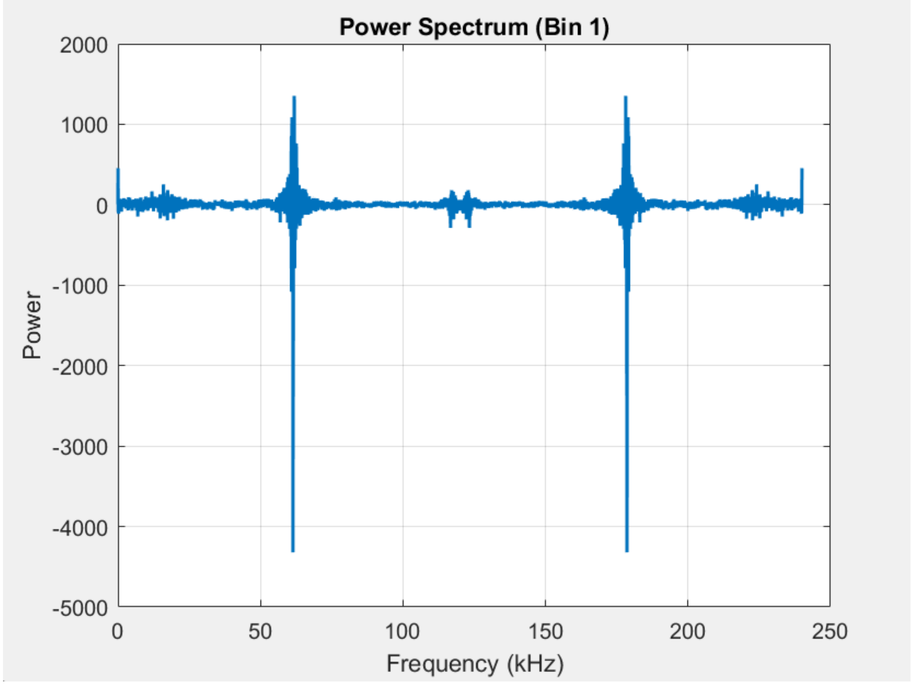

Figure 4.15: Run 22 power spikes ($\phi = 1.17$, 10 mm RDE, CH_4-0_2). Frequencies shown are approximately 61 kHz and 118 kHz, with mirroring above 120 kHz.

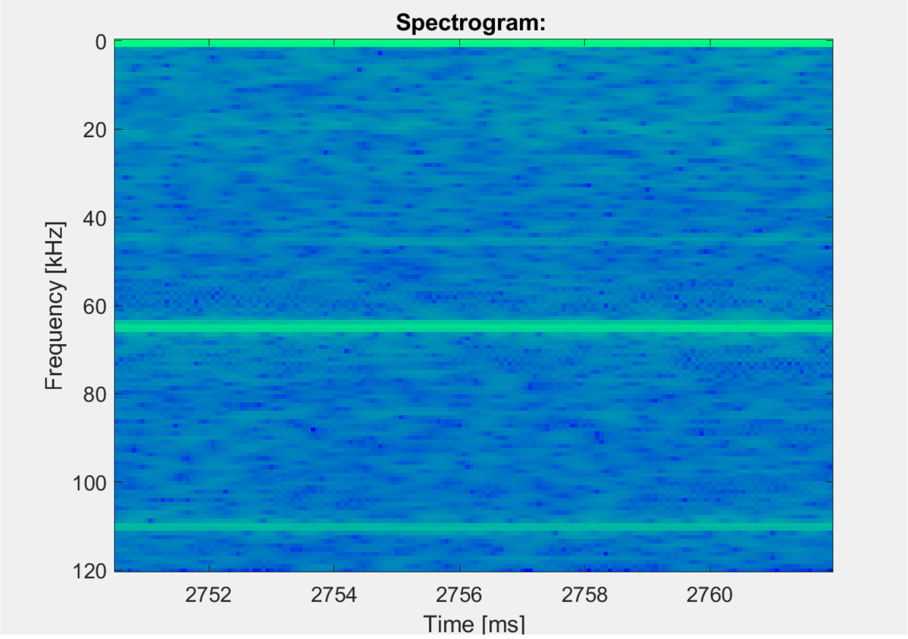

Figure 4.16: Run 59 spectrogram ($\phi = 1.4$, 10 mm RDE, CH_4-0_2). Frequencies shown are approximately 19 kHz (faint), 43 kHz, 63 kHz and 113 kHz.

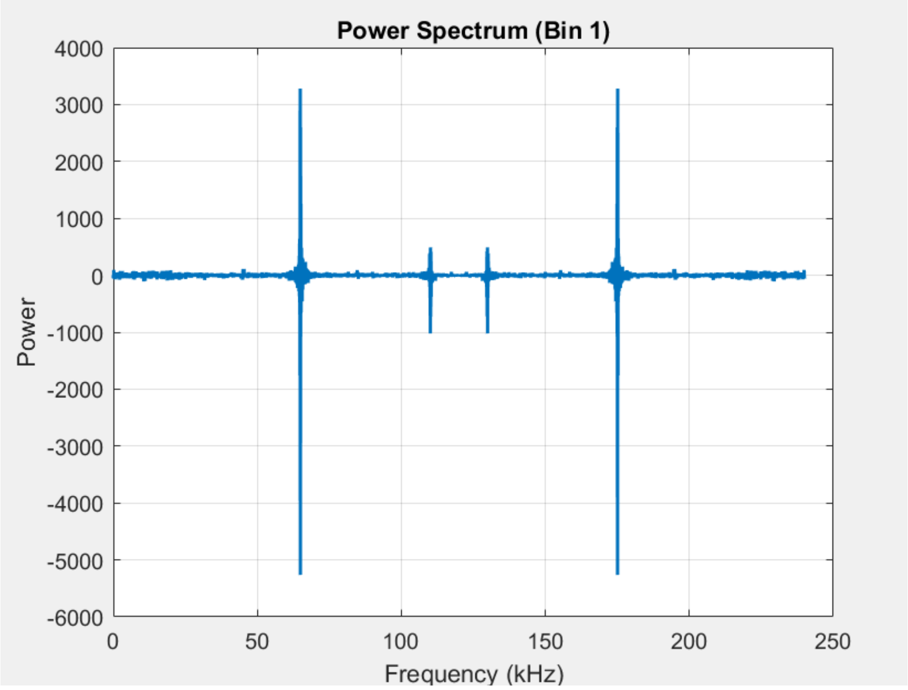

Figure 4.17: Run 59 power spikes ($\phi = 1.4$, 10 mm RDE, CH_4-0_2). Frequencies shown are approximately 63 kHz and 113 kHz, with mirroring above 120 kHz.

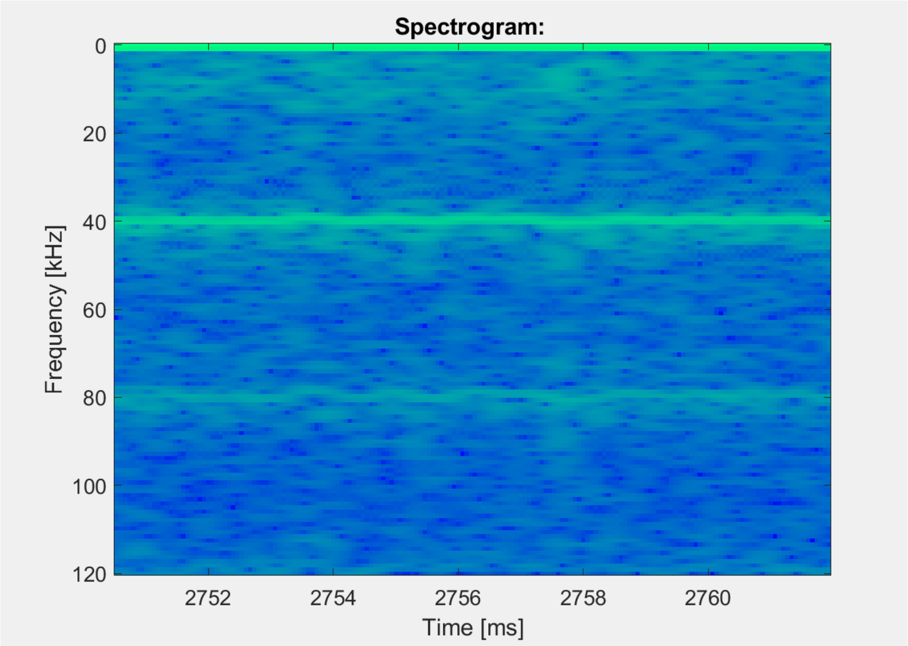

Figure 4.18: Run 144 spectrogram ($\phi = 1.15$, 10 mm RDE, CH_4-0_2). Frequencies shown are approximately 40 kHz and 80 kHz.

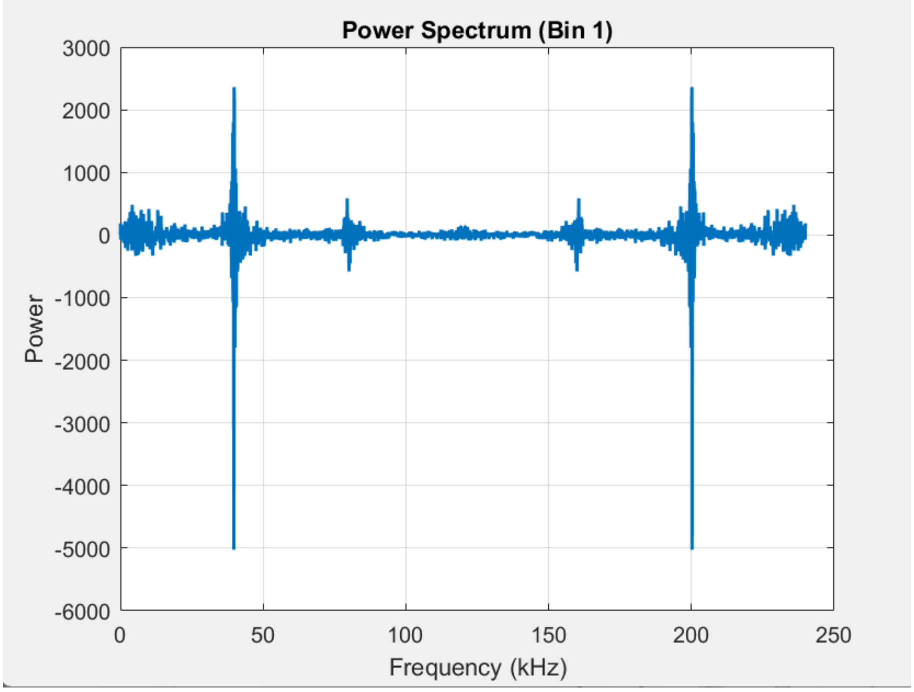

Figure 4.19: Run 144 power spikes ($\phi = 1.15$, 10 mm RDE, CH_4-0_2). Frequencies shown are approximately 40 kHz and 80 kHz, with mirroring above 120 kHz.

- The faint spike around 19 kHz is close to the 1R frequency of 15 kHz
- 40–43 kHz is close to the 1T resonance frequency
- 61–63 kHz is close to the 2T resonance frequency

The remaining frequencies called out are likely artifacts of the Fast-Fourier Transform method, which creates duplicates of the average experimental frequencies in the process of highlighting the frequencies. This means that the frequencies of 80 kHz and 113–118 kHz are likely non-physical, although it is nonetheless worth pointing out the possible correlations to transverse modes:

- 80 kHz $\approx$ 3T frequency of 84 kHz
- 113–118 kHz falls between the 4T/1T1R frequency of 106 kHz and the 5T frequency of 128 kHz

It remains unclear precisely which mechanisms pick out the operating frequencies seen in the data, although there are a few trends revealed. For instance, it can be seen that the 1R mode is operating at low frequency of about 15 kHz, while the pure tangential modes of 1T and 2T modes may be operating simultaneously, as in Run 59 with the higher equivalence ratio. This demonstrates how multiple acoustic waves in RDEs can co-exist within the same operating conditions while still creating only one unified detonation wave.

Although a single detonation wave spin speed is captured by the video data during the time of record (TOR), this analysis has not yet taken into account the transient behavior as the RDE begins operation in a detonation-driven regime. Indeed, the presence of multiple frequencies is clearly seen in the initial propellant flow before firing the pre-detonator to start the engine, and the frequencies generated by the initial blast wave, specifically whether the 1R mode in hollow RDEs or 1T mode in annular RDEs is able to start, may determine whether a detonation wave is successfully created while also serving to strengthen the later visible detonation wave and enable steady spin.

§4.1.5.5 Heated propellants

The 10 mm coreless RDE was also run with heated propellant using an external fuel line heat wrap (see Sec. §3.1.2.1). As the data obtained above might have said, tests run with unheated propellant showed consistent pressurization and visible confirmation of detonation waves only above $\phi = 1.15$. Below that equivalence ratio, the engine was assumed to revert to deflagration due to the lack of luminous spinning detonations (note: it is typical for detonation waves to be more luminous at low ϕ than at $\phi \geq 1$, which strengthened the assumption of deflagration). In contrast, tests run with the heated propellant, which achieved a mixture temperature increase of about 10 K above the unheated initial propellant temperature, showed consistent ignition and detonation with both camera and pressure data until $\phi = 1.0$. However, the current sparcity of data does not allow for further analysis of whether detonation was sustained but with low luminosity as in the unheated propellant case.

In contrast to Fig. 4.13, which showed only the experimental data points with unheated fuel (UF), Fig. 4.20 includes the heated fuel (HF) data, noted as "HF Exp." on the chart. Both the UF and HF datasets operated with one detonation wave for all cases shown here. While the unheated fuel was previously thought to be operating with deflagration due to the lack of visibly distinguishable detonation waves, plotting it alongside the predicted frequency modes shows that all of the operating frequencies are in fact in the same range, primarily located just above the 2T wave mode (despite the 1-wave operation). The exceptions to this correspond to the experimental points that hover just above the 1T line; possible explanations for the lower frequency values are that those experiment runs correspond to unsteady engine operation, that they had lower mass fluxes than the other runs, or simply that during those runs steady-state operation was established close to the 1T mode frequency. If the last hypothesis is correct, it prompts a closer look at the initial transient pressure spikes and shock wave behavior during detonation wave establishment, i.e. before the experiment time of record from which the plotted experimental frequencies are calculated.

§4.1.6 25 mm RDE: CH_4 Frequency Results and Discussion

This section discusses the 25 mm hollow RDE run on methane, similar to the previous sections.

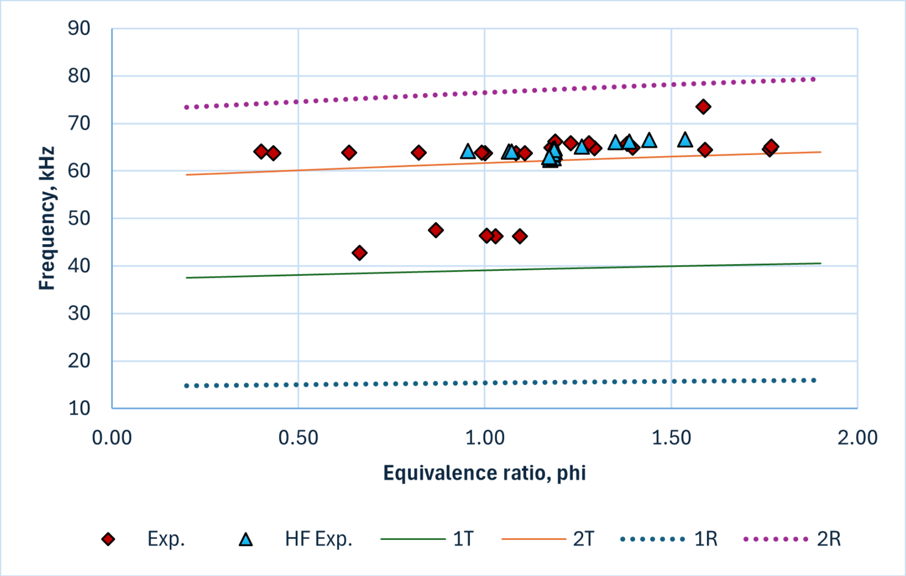

Figure 4.20: CH_4, 10mm; transverse mode frequencies vs. experimental data ($w = 1$ for all experiment data). Here unheated fuel frequency data are demarcated by red diamonds, while heated fuel data are demarcated by blue triangles.

§4.1.6.1 Wave spin speed

As in previous sections, the experimental data shown in Fig. 4.22 are the same data plotted in the results of Sec. §4.1.6.3. The rise in spin speed and frequency at low phi appear to be an artifact of the behavior of methane in the 25 mm RDE, since it is seen also in the 25 mm annular RDE configurations with gap widths of 3 mm and 5 mm; see Secs. §4.2.2 and §4.2.3 for comparison.

Wave spin speed in the 25 mm hollow RDE has been previously reported, for instance as seen in Fig. 4.21; however, the apparently anomalous inverse relationship between detonation speed, D_{CJ}, and wave spin speed across a sweep of ϕ had not been resolved. However, note that when the ideal gas wave spin speed was normalized by D_{CJ}, the result showed a peak at low ϕ exactly as seen in the experimental data plotted in Fig. 4.21.

For both the 25 mm and 10 mm hollow RDE results, CH_4 showed only one wave, while the 10 mm hollow RDE run on H_2 produced multiple wave cases. In hydrogen, individual wave cases ($w = 1$ and $w = 2$) showed that experiment frequencies generally increased

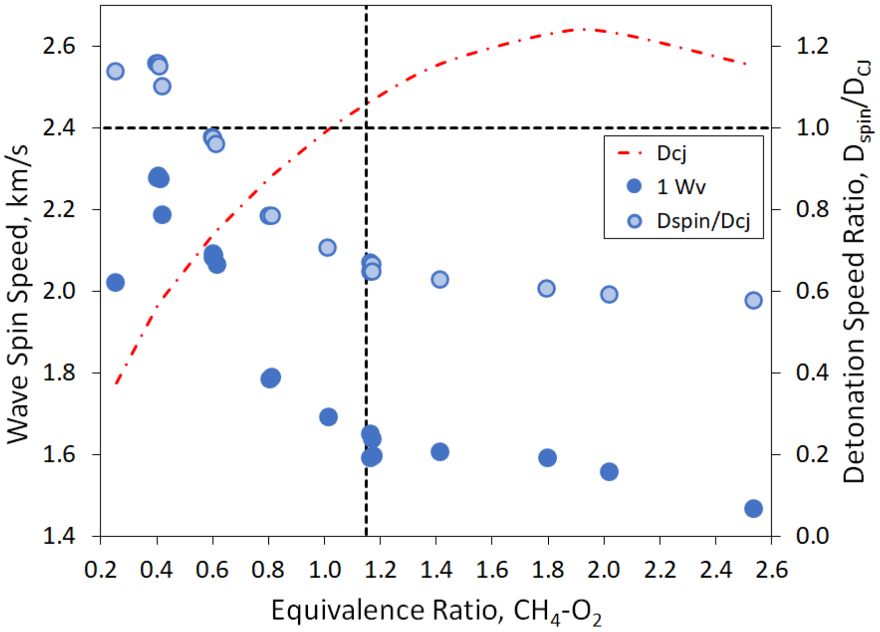

Figure 4.21: Wave spin speed in the 25 mm hollow RDE running CH_4-O_2. The solid dots are experimental spin speeds (as in Fig. 4.22), while the hollow dots are idealized detonation spin speed normalized by D_{CJ} [13].

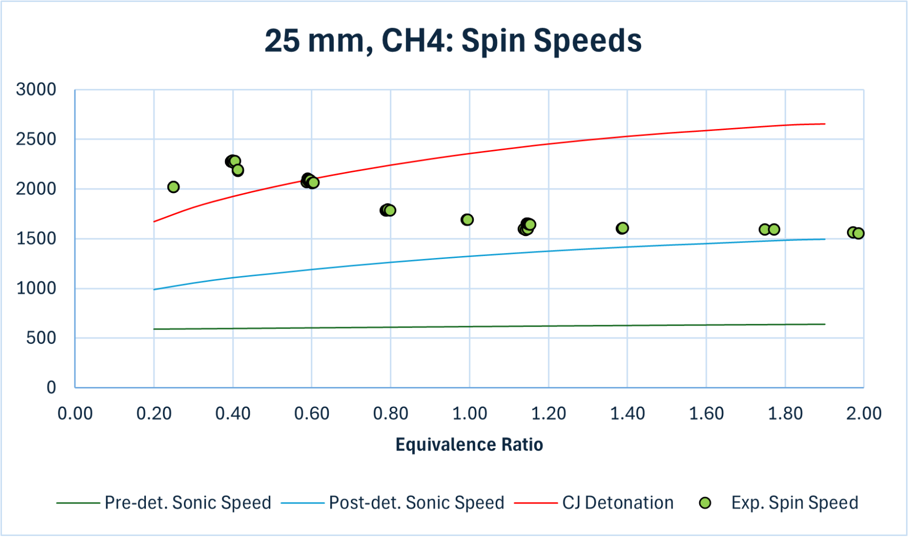

Figure 4.22: Wave spin speed vs. D_{CJ} and a_{CJ} in the 25 mm hollow RDE running CH_4-O_2.

as ϕ increased, correspondingly increasing the speed across the individual wave datasets. However, as wave count increased from $w = 1$ to $w = 3$, the experiment speed decreased by roughly 60% and again by $\tilde{1}$8%. Since frequency rose by about 30% and 18%, respectively, it can be concluded that the wavelength decrease with wave count increase has a much larger impact on wave spin speed than the observed frequency increase.

By comparison across gasses, and noting the difference in methane behavior between the 25 mm and 10 mm RDEs, it can be expected that higher wave counts in methane will increase engine frequency while decreasing wave spin speed and wavelength. This is consistent with prior literature as well; see the references noted in Sec. §2.2.1 for discussion of this phenomenon.

§4.1.6.2 Trend lines and expected base frequencies

The 25 mm RDE shows an arch behavior at low ϕ that appears to be unique to the 25 mm engine and/or the CH_4-O_2 propellant combination. No trend line was computed, but the expected baseline is shown as the reactant sound speed at $T = 1000$ K divided by combustor circumference (not, as previously, the injector ring circumference. This dataset saw only the $w = 1$ wave case; Fig. 4.23 shows the resulting graph.

§4.1.6.3 Initial frequency results

As in the 10 mm hollow engine, example frequency results are shown in Tables 4.12, 4.13, 4.14:

With the engine size increased to 25.4 mm precisely, and frequencies computed to $\phi=$ 2.8, Fig. 4.24 was made. As in the 10 mm RDE, the 25 mm RDE with CH_4-O_2 also saw wave numbers hold steady at $w = 1$ throughout the experimental test range. As you can see here, the methane data shows predictable trends on the 1T line for high equivalence

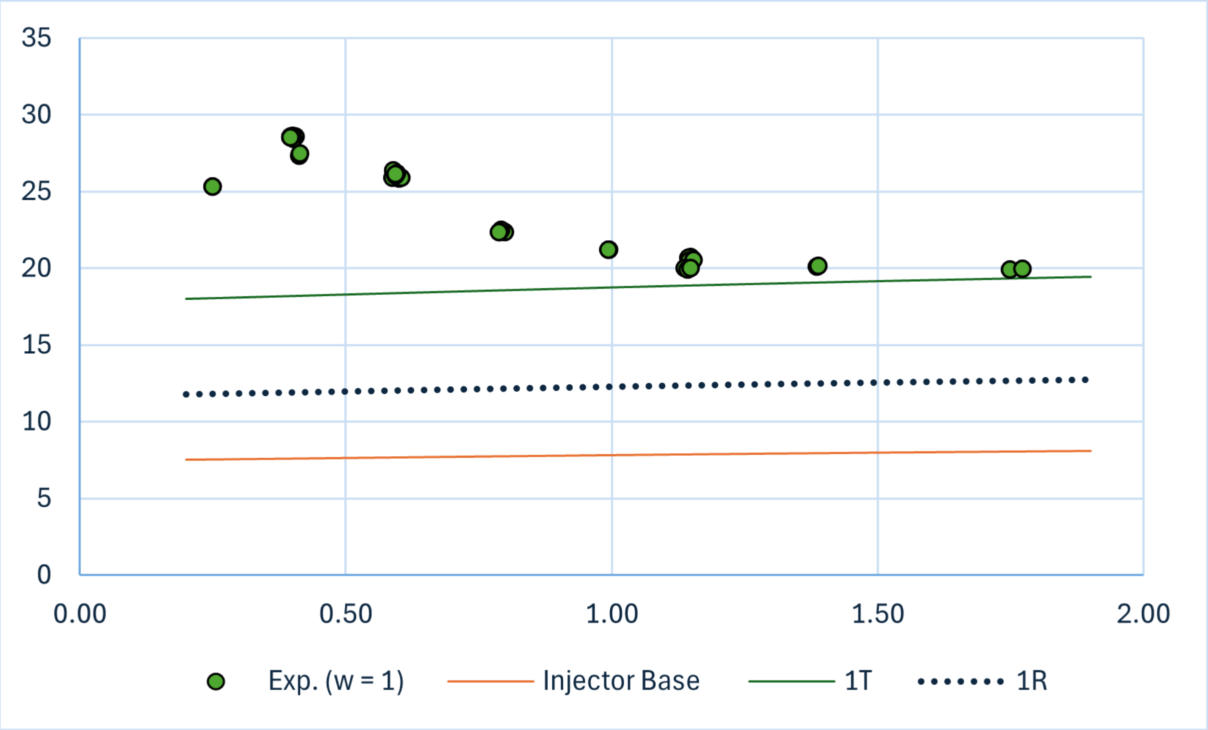

Figure 4.23: Experimental data frequencies compared to predicted 1R and 1T with the expected baseline in the hollow 25 mm RDE, CH_4-O_2.

Table 4.12: Code results: H_2, hollow, 10 mm, $\phi = 0.8$, $T = 1000$ K. Here m = radial modes are numbered across, n = tangential modes are numbered down.

	$m = 1$	$m = 2$	$m = 3$	$m = 4$	$m = 5$
$n = 0$	12 kHz	31.6 kHz	54.8 kHz	78.5 kHz	102 kHz
$n = 1$	18.4 kHz	42.4 kHz	66.1 kHz	90 kHz	114 kHz
$n = 2$	26.2 kHz	52.5 kHz	76.9 kHz	101 kHz	125 kHz
$n = 3$	34.2 kHz	62.3 kHz	87.3 kHz	112 kHz	136 kHz
$n = 4$	42.3 kHz	71.8 kHz	97.4 kHz	122 kHz	147 kHz

Table 4.13: Code results: H_2, hollow, 10 mm, $\phi = 1.15$, $T = 1000$ K. Radial modes are numbered across, tangential modes are numbered down.

	$m = 1$	$m = 2$	$m = 3$	$m = 4$	$m = 5$
$n = 0$	12.2 kHz	32.1 kHz	55.7 kHz	79.8 kHz	104 kHz
$n = 1$	18.8 kHz	43.1 kHz	67.2 kHz	91.5 kHz	116 kHz
$n = 2$	26.6 kHz	53.4 kHz	78.2 kHz	103 kHz	127 kHz
$n = 3$	34.8 kHz	63.3 kHz	88.8 kHz	114 kHz	138 kHz
$n = 4$	43 kHz	73 kHz	99.0 kHz	124 kHz	149 kHz

Table 4.14: Code results: H_2, hollow, 10 mm, $\phi = 1.6$, $T = 1000$ K. Radial modes are numbered across, tangential modes are numbered down.

	$m = 1$	$m = 2$	$m = 3$	$m = 4$	$m = 5$
$n = 0$	12.4 kHz	32.7 kHz	56.8 kHz	81.3 kHz	106 kHz
$n = 1$	19.1 kHz	43.9 kHz	68.5 kHz	93.3 kHz	118 kHz
$n = 2$	27.1 kHz	54.4 kHz	79.7 kHz	105 kHz	130 kHz
$n = 3$	35.4 kHz	64.5 kHz	90.5 kHz	116 kHz	141 kHz
$n = 4$	43.8 kHz	74.4 kHz	101 kHz	127 kHz	152 kHz

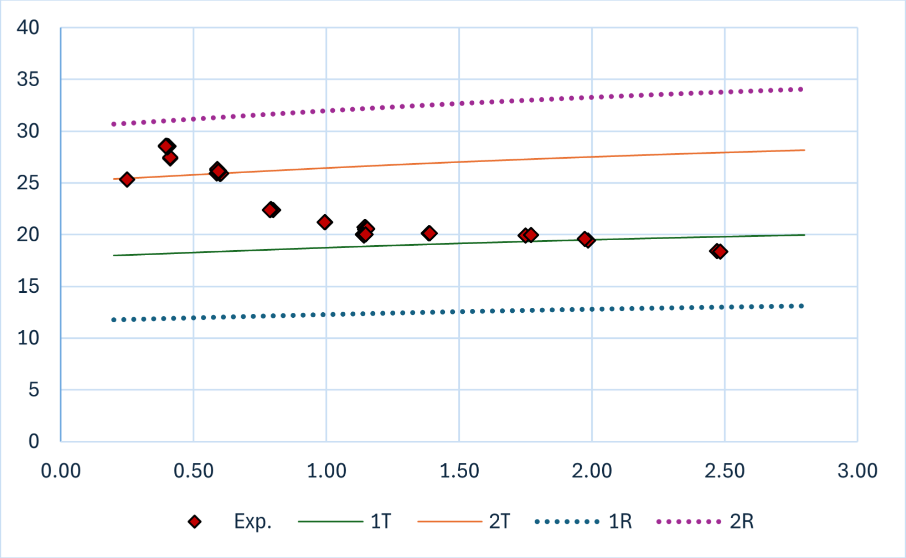

Figure 4.24: CH_4, 25.4 mm, hollow; transverse mode frequencies vs. experimental data. $w = 1$ for all experimental data.

ratio, while at low ϕ, the waves had higher experimental frequencies, almost reaching the 2T and 1R modes.

Notably, the data shown at values of $\phi < 1$ corresponded to runs previously marked as "deflagration runs," due to the difficulty of visibly distinguishing detonation waves. This was primarily due to camera placement directly downstream of the engine at the observation port of the wye tube: it was impossible to tell whether the engine was undergoing full deflagration with occasional pulsations or whether the detonation was steadily ongoing but obscured by luminous downstream gases. The frequency data plotted in Fig. 4.24 was obtained by the high-speed piezoelectric sensors rather than the high-speed camera recordings, and clearly shows the detonation ongoing via the correlation between data

Table 4.15: 25 mm, CH_4: approximate multiples of the 1R mode across the equivalence ratio sweep of $0.2 \leq \phi \leq 1.8$ and the remainder (based on deviation from the calculated transverse mode frequencies), alongside the standard deviation of the remainder across the ϕ sweep.

	Multiple of 1R	Remainder	Standard dev. in rem.
1T	1.5	0.3 – 0.4 kHz	0.8×10^{-2}
2T	2	1.8 – 2 kHz	4.4×10^{-2}
3T	3	2.2 – 2.4 kHz	5.3×10^{-2}
1R	2.5	1.2 – 1.3 kHz	2.8×10^{-2}
1T1R	3.5	0.2 kHz	0.4×10^{-2}
4T	3.5	0.2 – 0.3 kHz	0.6×10^{-2}

points and the predicted modes.

For comparison to the 10 mm engine, the same mode frequency analysis was computed for the 25 mm engine, and is shown in Table 4.15. Intriguingly, although the base multiples of the 1R mode are different for the larger engine than for the 10 mm RDE, there are some correlations. For instance, in the 25 mm RDE the 1T1R mode is a multiple of 3.5×1R, while in the 10 mm RDE the multiple is 7×1R, which is to say that the multiple for the 1T1R mode in 25 mm hollow RDE is exactly half that multiple in the 10 mm hollow RDE.

§4.1.7 Temperature Comparison Across Hollow RDE Cases

Temperature has a strong effect on the predicted frequency results. Hence, the resonance frequencies were determined over a sweep across multiple temperature values ($T = 300$ K, 500 K, 800 K, 1200 K) and plotted as equivalence ratio vs. frequency for each of the hollow runs to to examine how this parameter influenced the theory-experiment correlations across engine sizes and propellants.

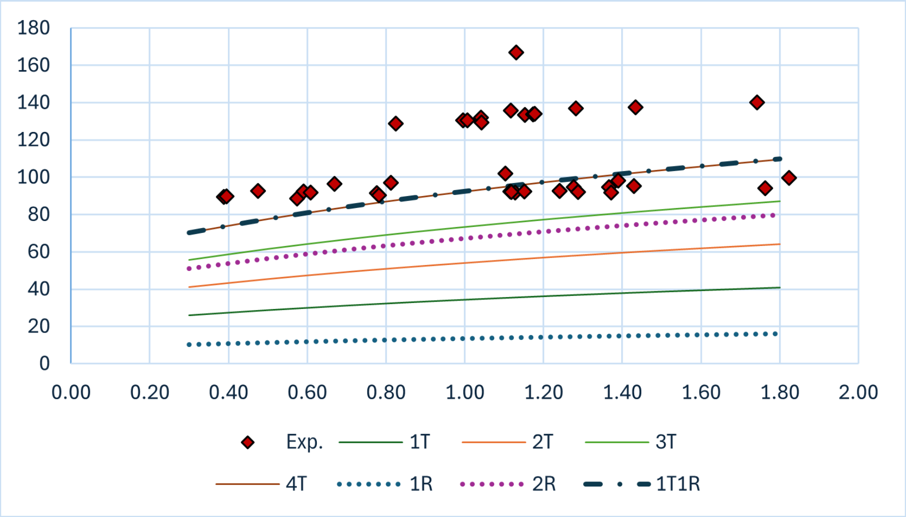

Figure 4.25: $T = 300$ K, 10 mm RDE, H_2.

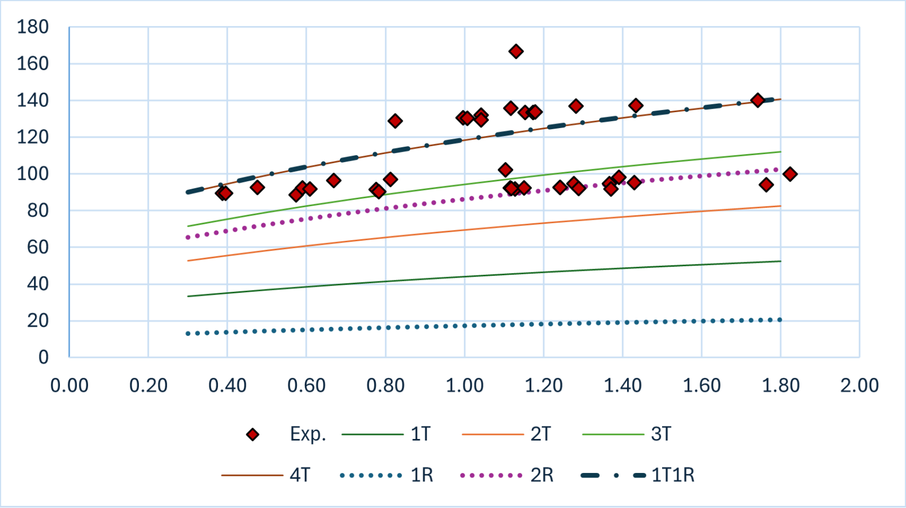

Figure 4.26: $T = 500$ K, 10 mm RDE, H_2.

§4.1.7.1 10 mm RDE: H_2-O_2

For the 10 mm RDE run with hydrogen fuel, a temperature sweep was conducted for initial incoming propellant temperatures of $T = 300$ K, 500 K, 800 K, 1200 K and 1400 K; this is shown in Figs. 4.25–4.29. Additionally, to verify the use of the pre-ignition propellant sound speed rather than the post-ignition (C-J) sound speed, a plot using data created with a_{CJ}, $T = 1000$ K is presented in Fig. 4.30 to compare to the plot shown in Sec. §4.1.4.3.

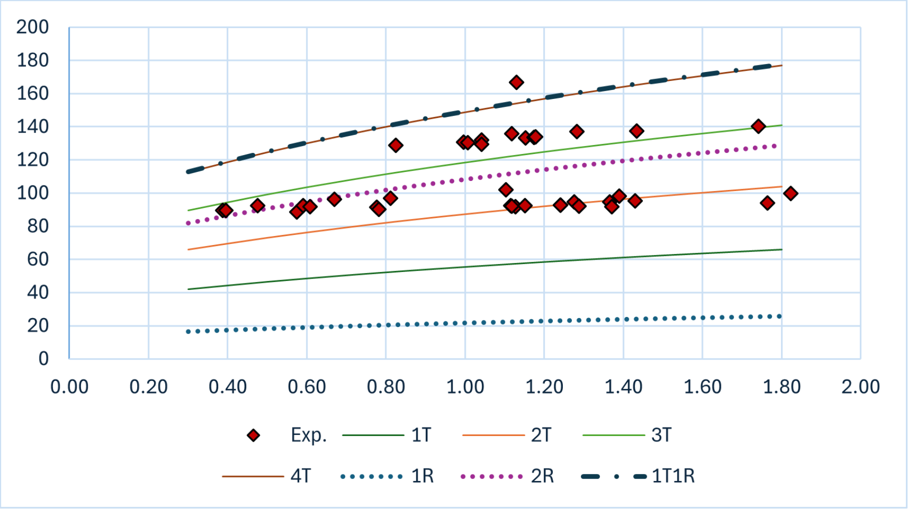

Figure 4.27: T = 800 K, 10 mm RDE, H_2.

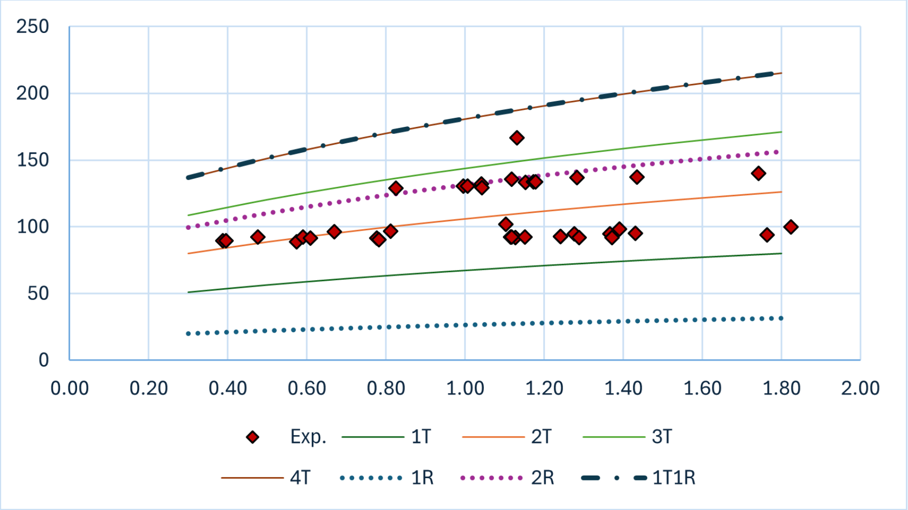

Figure 4.28: T = 1200 K, 10 mm RDE, H_2.

Unlike the methane cases following, the temperature sweep across the 10 mm RDE with H_2-O_2 indicates that the hydrogen is heated to 1400 K, since the data in Fig. 4.29 shows the closest correlation of the $w = 1, 2$, and 3 wave count data to the 1T, 2T and 3T resonance modes.

The transverse mode frequencies calculated using the C-J product sound speed, a_{CJ} with initial propellant temperature of $T = 1000$ K are plotted in Fig. 4.30. It is clear from the figure that the predicted transverse modes both curve too sharply and are spaced too far apart to give reasonable correlations to the experimental frequency data. So for the

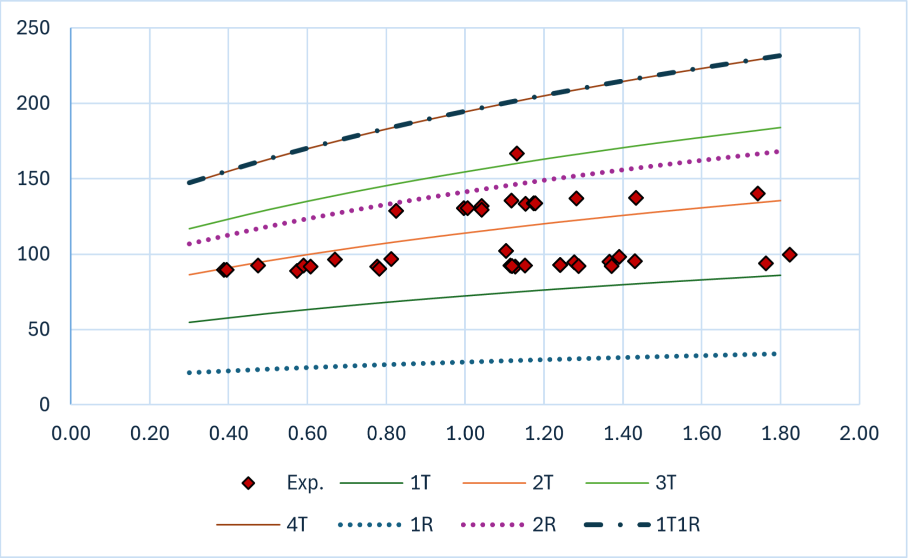

Figure 4.29: $T = 1400$ K, 10 mm RDE, H_2.

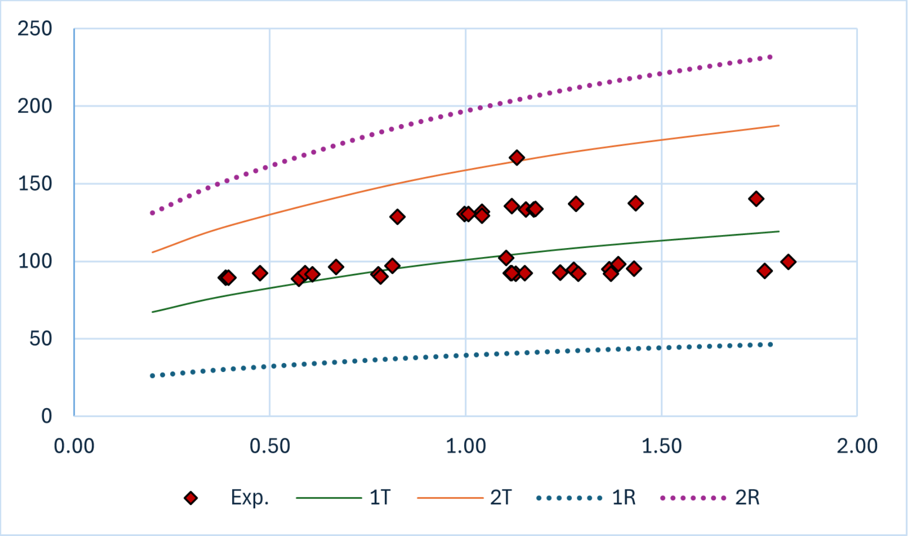

Figure 4.30: $T = 1000$ K, using a_{CJ} sound speed, 10 mm RDE, H_2.

purposes of matching and categorizing possible resonance modes in the RDE, it is more accurate to use the reactant sound speed for frequency calculations.

For clarity in visualizing the frequency increase with initial temperature increase, Fig. 4.31 shows the modal frequencies at fixed equivalence ratio, $\phi = 1.15$. Note that although experimental data points do not have experimentally measured temperature values, the data are plotted here on the $T = 1100$ K vertical line to distinguish the experimental points from the modal prediction.

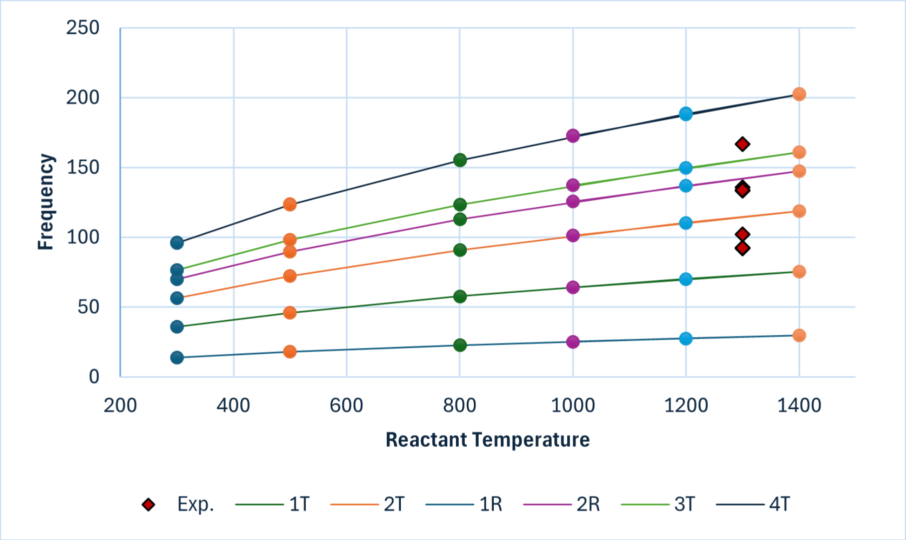

Figure 4.31: $\phi = 1.15$, 10 mm RDE, CH_4. Experimental data points are plotted at $T = 1300$ K for easier visualization.

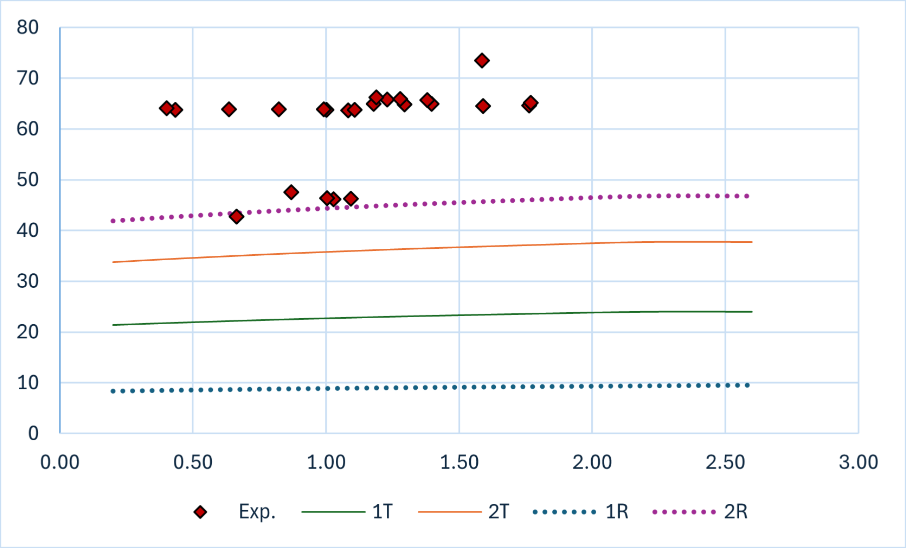

Figure 4.32: $T = 300$ K, 10 mm RDE, CH_4.

§4.1.7.2 10 mm RDE: CH_4-O_2

For the 10 mm RDE run on methane, the temperature sweep included the incoming propellant temperatures of $T = 300$ K, 500 K, 800 K and 1200 K. Data from these are shown in Figs. 4.32–4.35. It is clearly seen that for temperatures lower than 1000 K, the predicted modes underestimate the actual frequencies, while the higher temperatures overestimates the data compared to the initial $T = 1000$ K result.

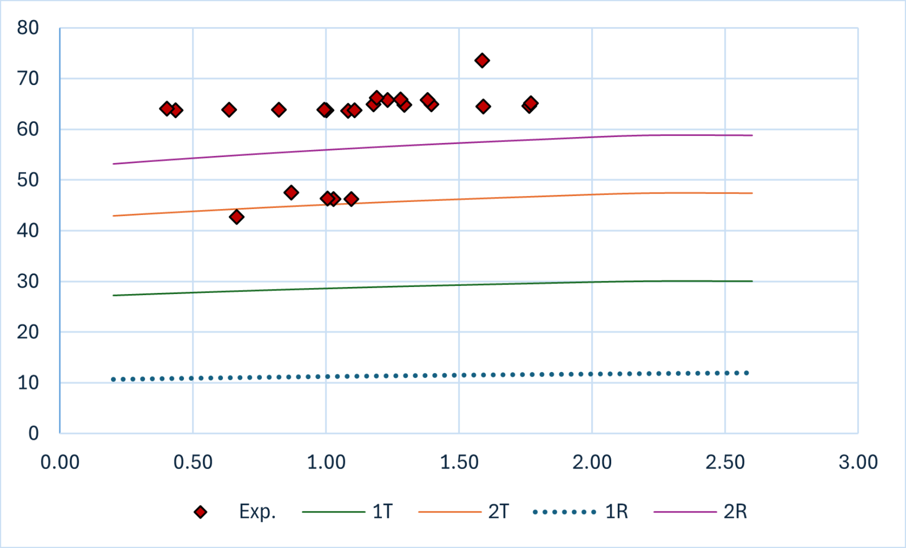

Figure 4.33: $T = 500$ K, 10 mm RDE, CH_4.

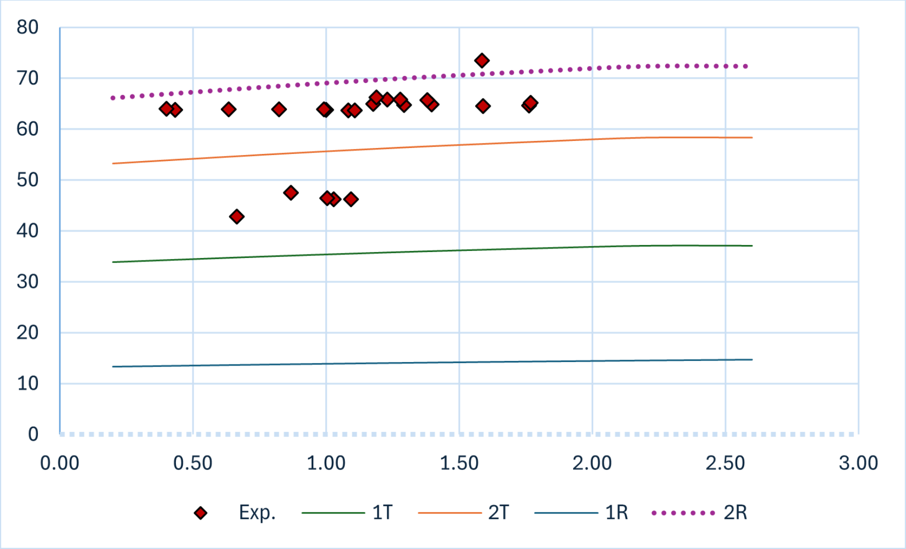

Figure 4.34: $T = 800$ K, 10 mm RDE, CH_4.

Fig. 4.36 shows the increase in modal frequency at fixed equivalence ratio, $\phi = 1.15$. Note that although experimental data points do not have experimentally measured temperature values, the data are plotted on the $T = 1100$ K vertical line to distinguish the experimental points from the modal prediction. The outlier seen at about 10 kHz is an anomaly that seems to have produced a slight pressure rise in the combustor while not fully achieving detonation frequencies.

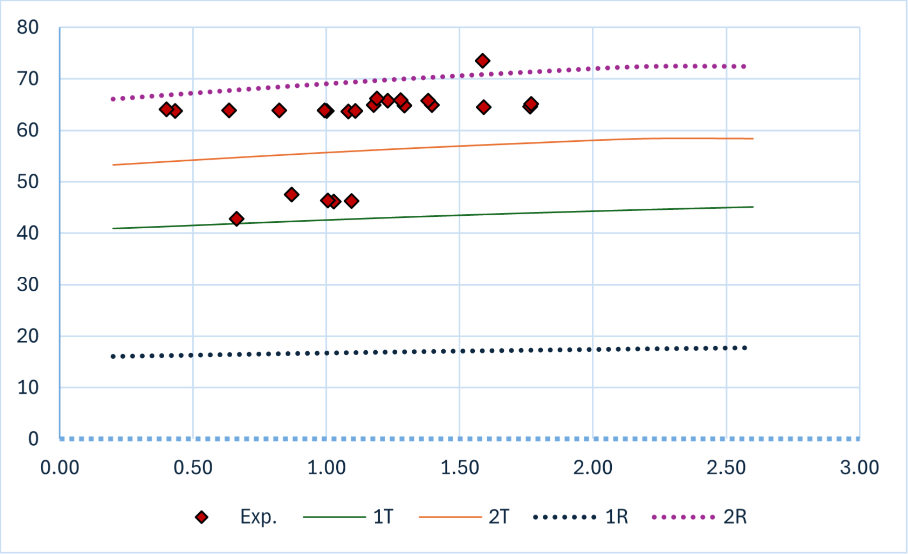

Figure 4.35: $T = 1200$ K, 10 mm RDE, CH_4.

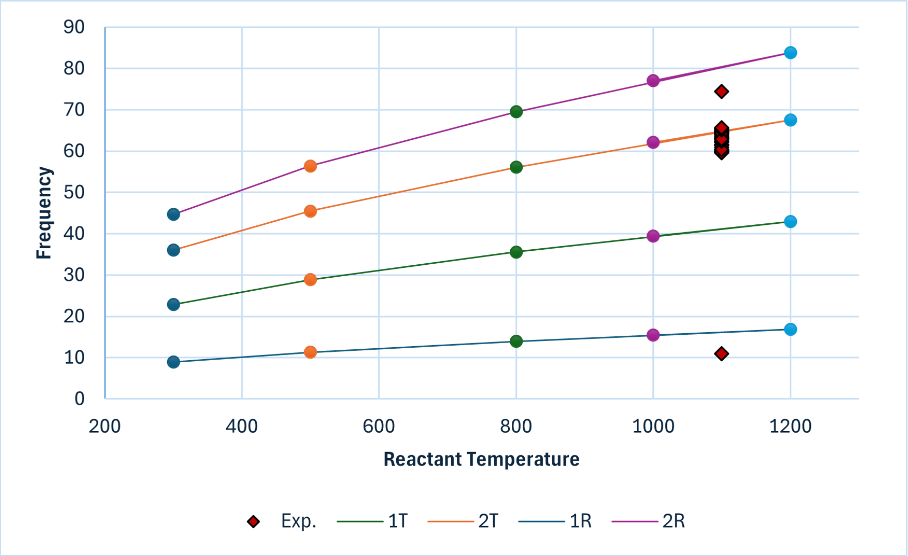

Figure 4.36: $\phi = 1.15$, 10 mm RDE, CH_4. Experimental data points are plotted at $T = 1100$ K for easier visualization.

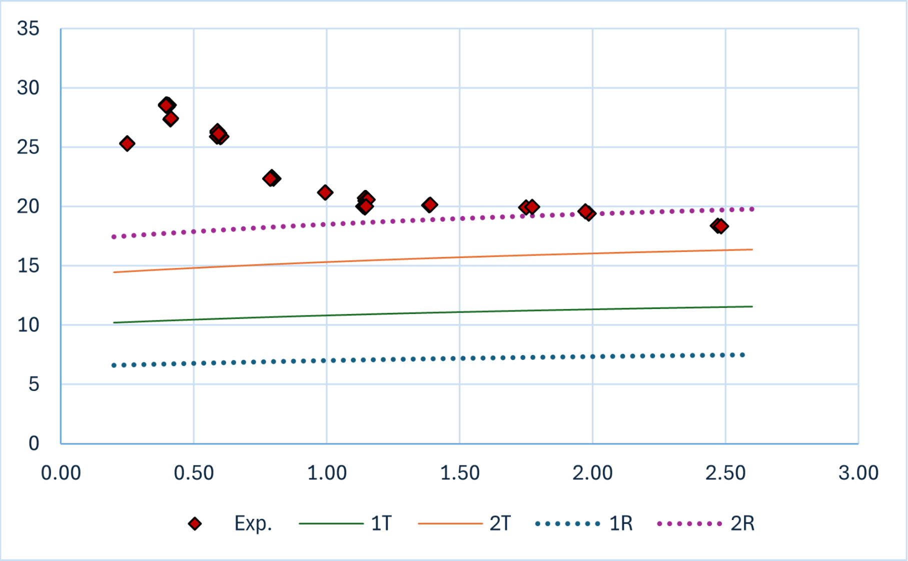

Figure 4.37: T = 300 K, 25 mm RDE, CH_4.

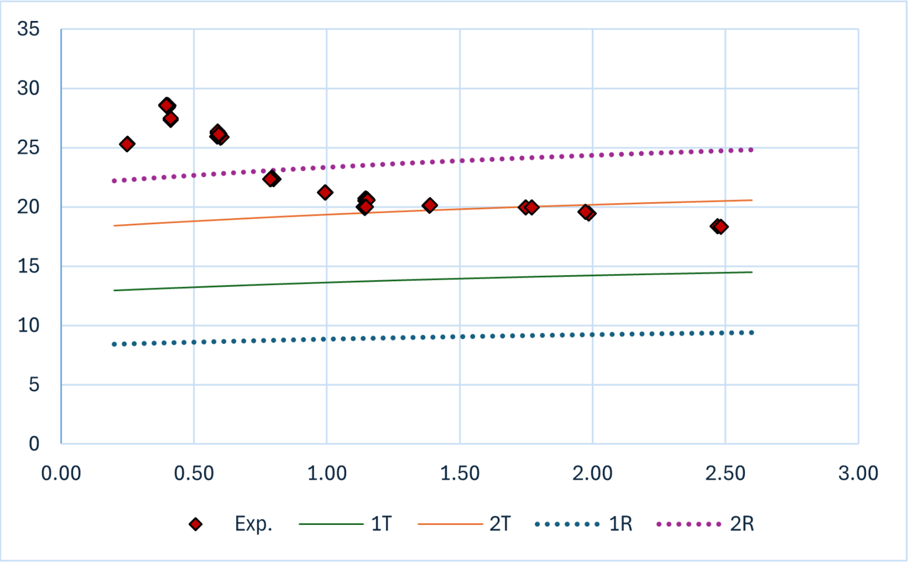

Figure 4.38: T = 500 K, 25 mm RDE, CH_4.

§4.1.7.3 25 mm: CH_4-O_2

Similar to the 10 mm methane case, the 25 mm RDE temperature sweep included the incoming propellant temperatures of T = 300 K, 500 K, 800 K and 1200 K. This is shown in Figs. 4.37–4.40. As is consistent in the temperature sweep results, initial temperatures at or below 800 K both underestimate the modal frequencies and are placed too close together; above T = 1000 K, however, the results differ. For the 25 mm engine,

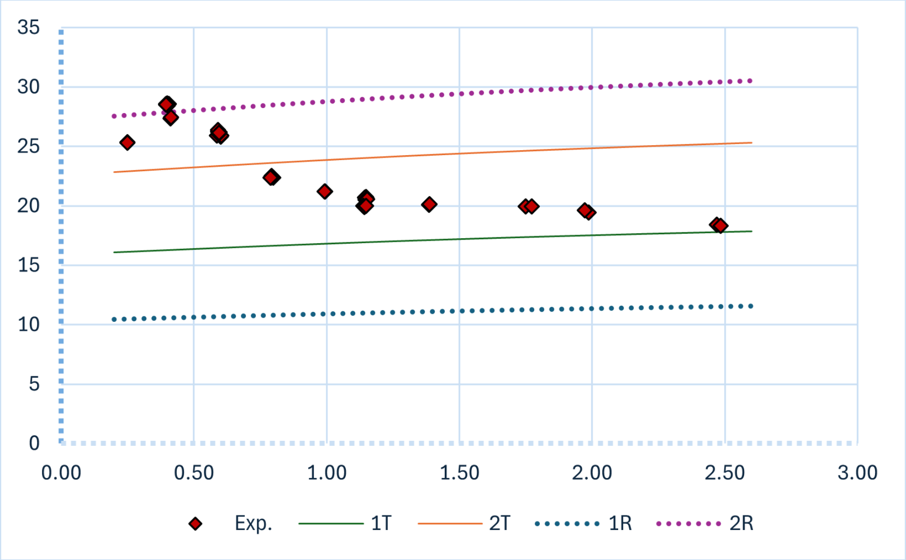

Figure 4.39: $T = 800$ K, 25 mm RDE, CH_4.

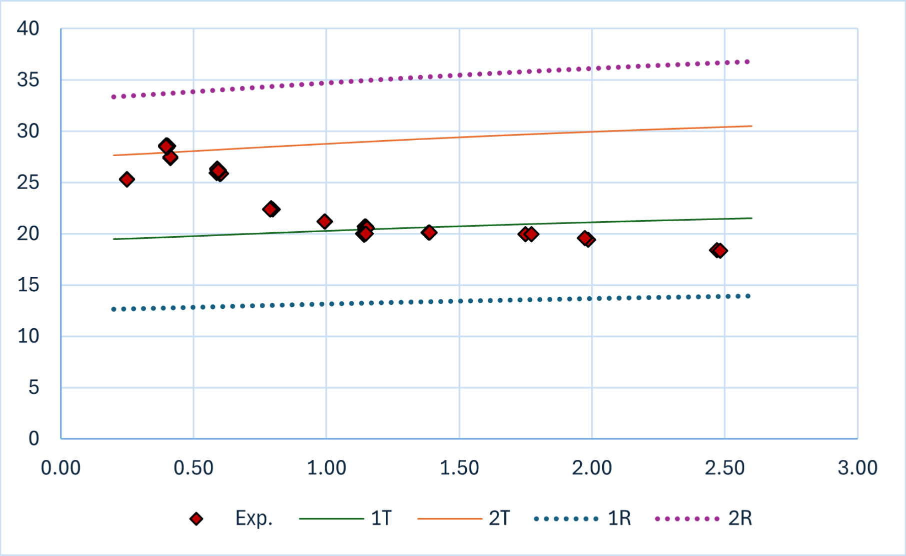

Figure 4.40: $T = 1200$ K, 25 mm RDE, CH_4.

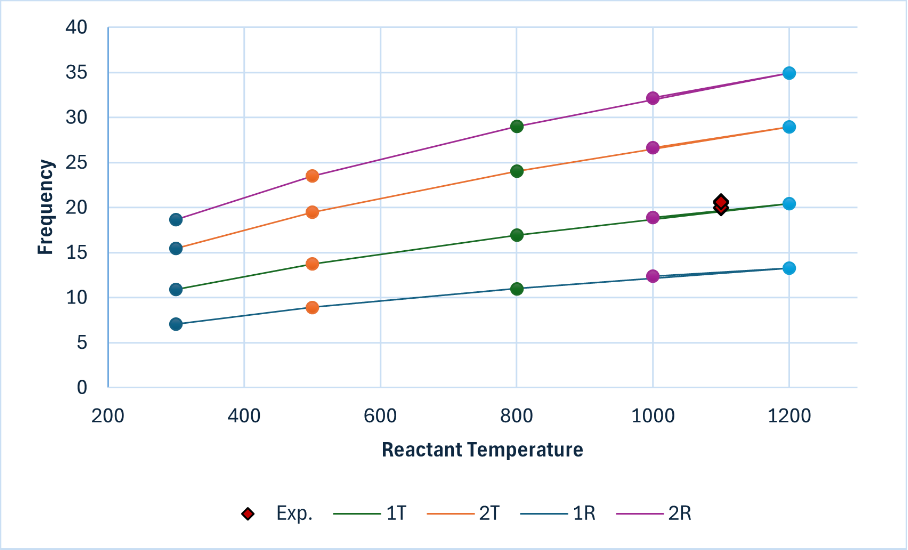

Figure 4.41: $\phi = 1.15$, 25 mm RDE, CH_4. Experimental data points are plotted at $T = 1100$ K for easier visualization.

at $T = 1200$ K the predicted frequencies may be a better match to the experimental data than the $T = 1000$ K plot (Fig. 4.13). More work is needed to fully investigate that question.

Fig. 4.41 shows the increase in modal frequency at fixed equivalence ratio, $\phi = 1.15$; just as in the 10 mm RDE with CH_4-O_2, experimental data points are plotted on the $T = 1100$ K vertical line to distinguish the experimental points from the modal prediction.

§4.2 Acoustic Analysis in Annular RDEs

The results in this section use the annular code based on Eq. 3.21, for the annular cases as listed in Table 3.4. As in the hollow case, the 10 mm RDE with the 2 mm gap was run on both H_2-O_2 and CH_4-O_2 while the 25 mm engine was run on CH_4-O_2 only for all annular gap widths.

The 25 mm annular engine saw counter-rotating waves for two of the three gap

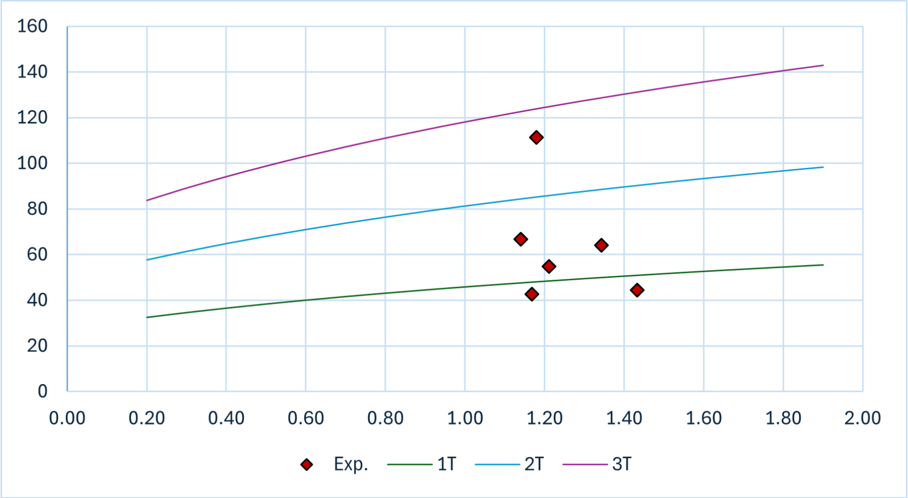

Figure 4.42: Annular 10 mm RDE run with H_2 fuel; experimental data vs. predicted transverse modes.

widths considered below. Where applicable, the counter-rotating waves are graphed as experimental data points in addition to the graphs of transverse modes with experimental data.

§4.2.1 10 mm RDE: 2 mm Gap

As noted in Sec. §3.1.2, the experimental data for the 2 mm gap in the 10 mm RDE was limited due to the erosion of the cores during testing. Nonetheless, the predicted frequencies along with the experimental data for the 10 mm annular runs with both hydrogen and methane propellants are shown in Figs. 4.42 and 4.43, respectively.

Figs. 4.42 and 4.43 highlight the difference in ideal gas behavior in RDEs, namely that methane is a less volatile fuel that tends toward steady running while the high volatility of hydrogen leads to less predictable experimental results. It can clearly be seen that the core erosion in hydrogen runs lead to a widening of the annular gap, which affected overall engine frequency. This seems to have lead toward higher average run frequencies while maintaining the tangential spin of the detonation wave.

It is interesting that although not all runs presented here showed clear detonation

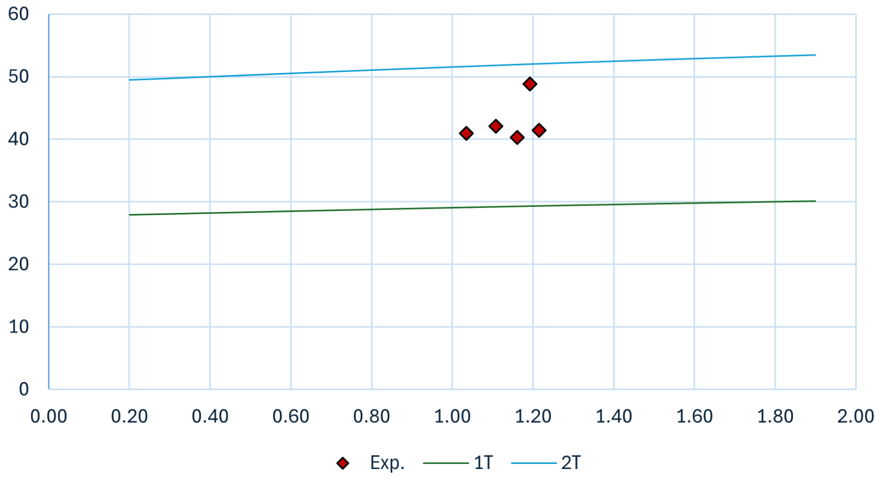

Figure 4.43: Annular 10 mm RDE run with CH_4 fuel; experimental data vs. predicted transverse modes.

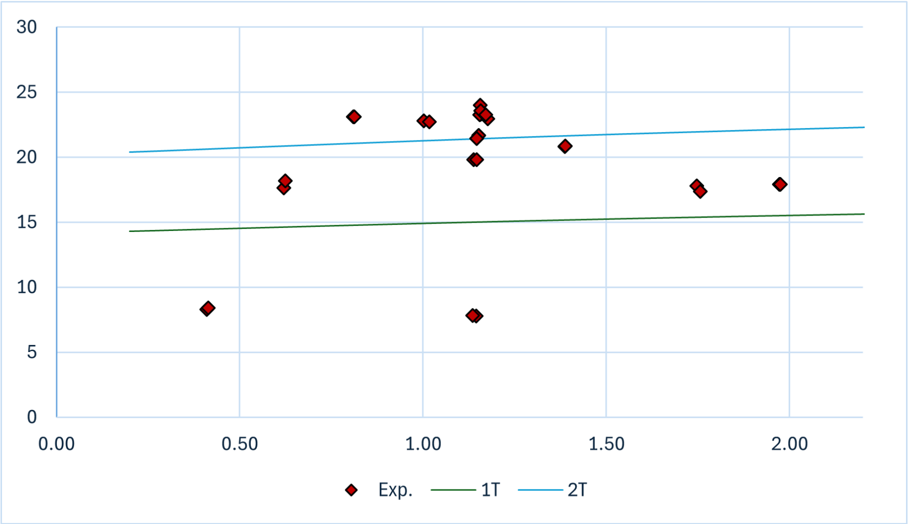

Figure 4.44: 25 mm, 3 mm gap: experimental data vs. predicted tangential modes at $T = 1000$ K, $p = 3$ bar over a range of ϕ.

waves in the video data, the frequencies that were recorded fall squarely in the detonation wave range as predicted by the code and based on the experimental data frequency ranges in the 10 mm hollow engine.

§4.2.2 25 mm: 3 mm Gap

The spin frequency vs. equivalence ratio data shown in Fig. 4.44 are located close to the 2T line, similar to how the CH_4 25 mm hollow configuration demonstrated close proximity

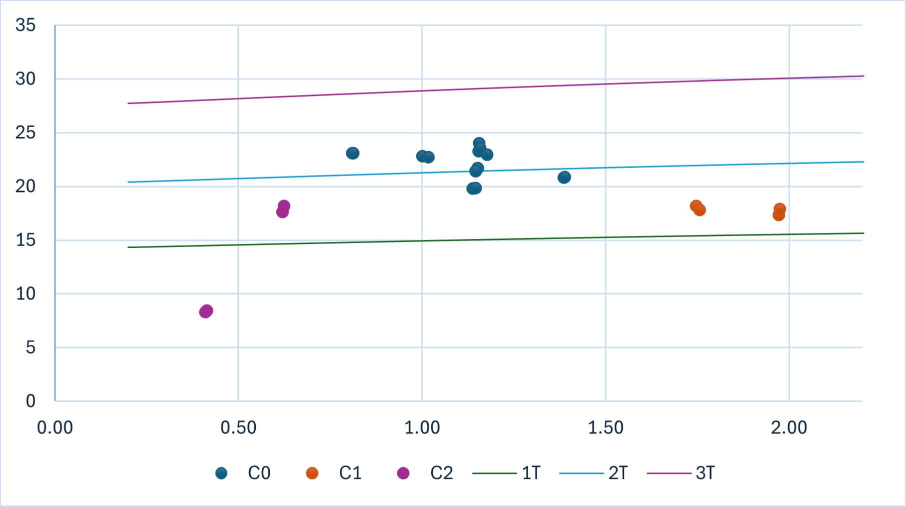

Figure 4.45: 25 mm RDE, 3 mm gap: counter-rotating wave data vs. transverse modes. No counter-wave is shown in group C0, one counter-wave is shown in group C1, and weak counter-waves are shown in group C2.

to the 1T line (Fig. 4.24). One difference lies in the comparative placement of the arch at low ϕ and the decline and plateau of data points at higher ϕ. In the hollow configuration, the peak of the arch was located at about $\phi = 0.50$, while with a 3 mm annular gap, the peak is located at about $\phi = 0.80$.

The 3 mm gap saw counter-rotating waves at more and slightly different engine conditions than the wider 25 mm gaps tested. The counter-rotating waves were weakly visible at low ϕ, but much stronger at high ϕ; this is in contrast to the 5 mm annular gap case, which saw counter-rotating waves only near stoichiometric conditions ($\phi \approx 1$). The experimental data are plotted again in Fig. 4.45 with the use of color to distinguish between the following three cases:

- 1-wave without counter-rotating wave (C0, blue)
- 1-wave with a strong counter-rotating wave (C1, orange)
- 1-wave with a weak counter-rotating wave (C2, purple)

It is suggestive that both the C1 and C2 groups hover at frequencies partway between

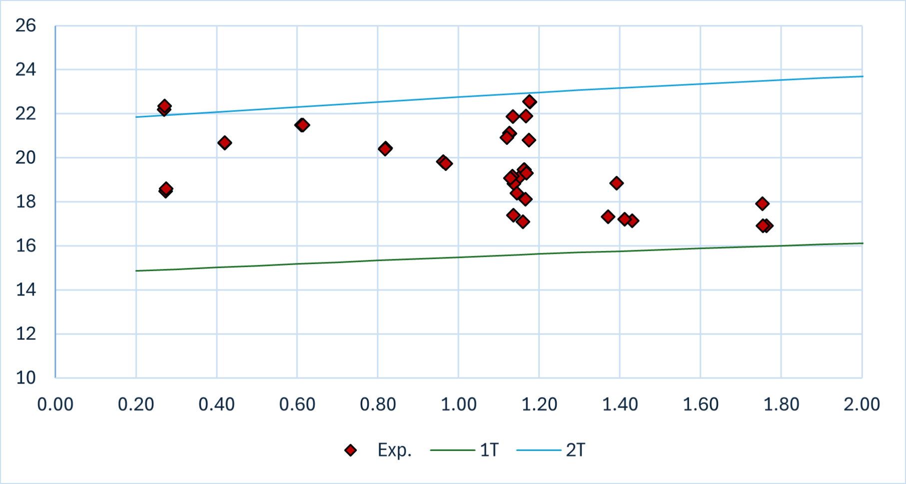

Figure 4.46: 25 mm, 5 mm gap: experimental data vs. predicted tangential modes at $T = 1000$ K, $p = 3$ bar over a range of ϕ.

the 1T and 2T modes, while the steady-state, counter-wave-less C0 group is found at the 2T frequency line. This points to the 1T mode acting as the base multiple in annular engines, rather than the 1R mode as found in the hollow configurations. The presence of the counter-rotating wave may act as a stabilizer, allowing operation at otherwise low mass fluxes (seen in the lowest-frequency data point), since as noted by Bluemner, tangential modes have double eigenvalues and can exist at 90° angles to each other: see Sec. §3.2.2 and specifically Fig. 3.17).

§4.2.3 25 mm: 5 mm Gap

The experimental data vs. tangential modes is plotted in Fig. 4.46, while Fig. **??** highlights cases with and without counter-rotating waves as groups C1 and C0, respectively. As mentioned in the previous section, counter-rotating waves were seen near stochiometric conditions, with no clear distinctions between weak or strong counter-rotating waves as in the previous case.

Fig. 4.48 shows the experimental data color-coded with counter-rotating wave data and with mass flux labels. While it is not exclusively true, the C1 group (one counter-rotating

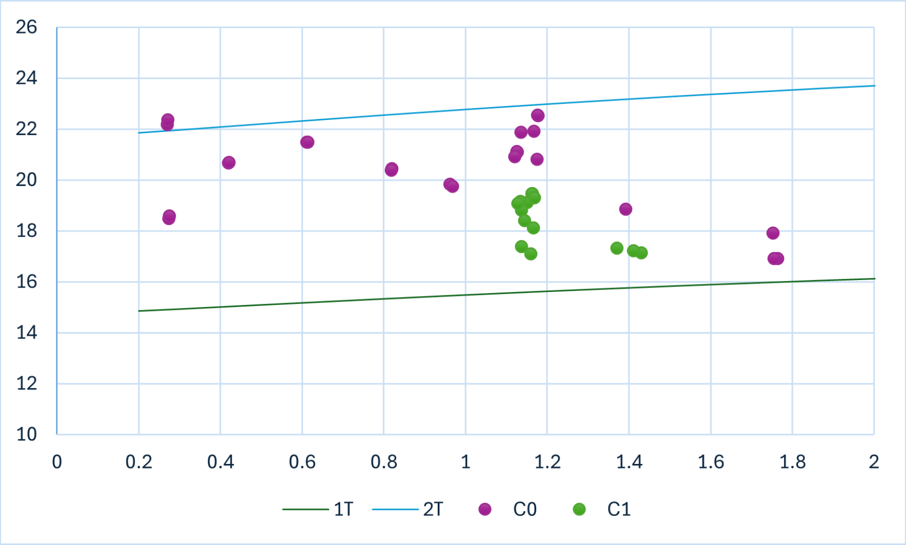

Figure 4.47: 25 mm, 5 mm gap: counter-rotating wave data vs. transverse modes. No counter-wave is shown as group C0, one counter-rotating wave is shown as group C1.

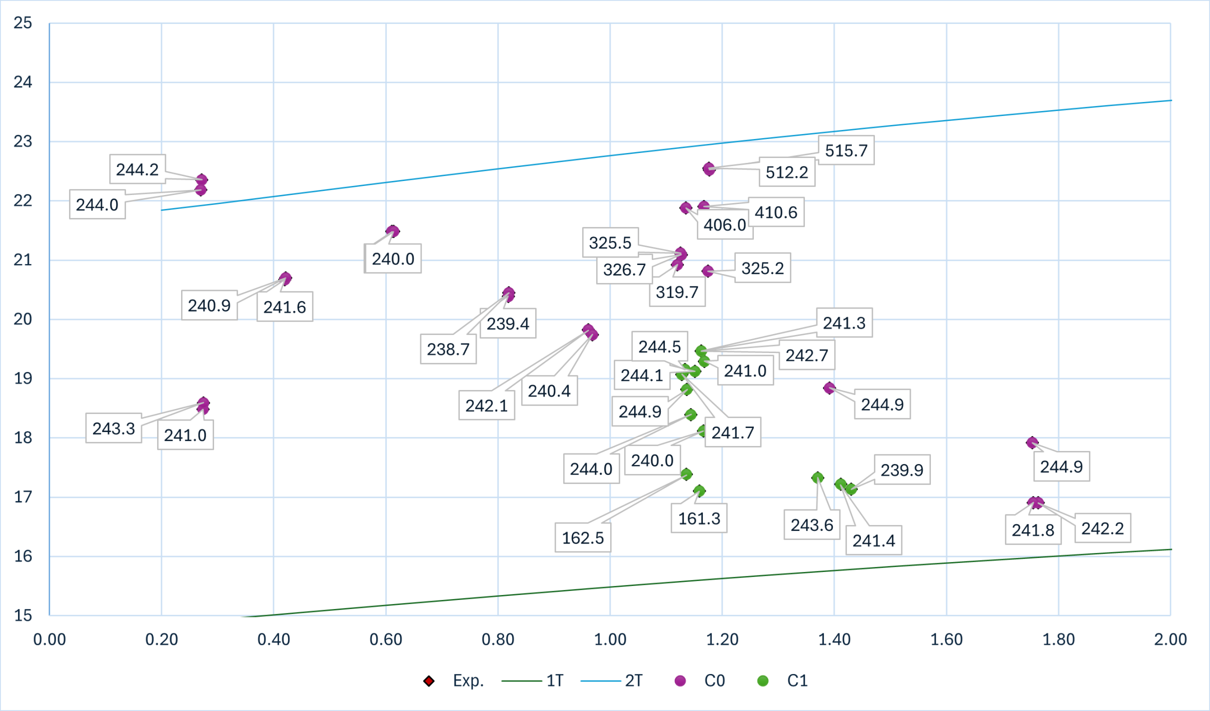

Figure 4.48: 25 mm, 5 mm gap: experimental data vs. transverse modes labeled with mass flux (values are in units of kg/(m$^2\cdot$ s) and color-coded by counter-rotating wave data (per Fig. 4.46). Zoomed-in view.

wave) is primarily composed of the low-mass-flux data points, while the C0 group generally had higher mass fluxes.

In particular, the data points around $\phi \approx 1.15$ were part of a sweep across mass flux, ranging from ψ = 160–516 kg/(m$^2\cdot$ s). It is also generally observed that at lower mass flux, experimental frequencies decreased, showing that frequencies vary directly with mass flux. This provides a straightforward mechanism for how increasing mass flux can promote wave bifurcation into steady, high-frequency, multi-wave modes.

Finally, it is seen that at steady mass flux values, here seen at $\psi \approx 240$ kg/(m$^2\cdot$ s), an arch is formed with a peak at about $\phi = 0.60$; see Figs. 4.24 and 4.45. This suggests an equivalence ratio-frequency correlation in methane with the highest frequency peak forming between $\phi \approx 0.80 - 0.50$, with higher ϕ values in smaller gap widths. The peak frequency appears to be a a fractional multiple of the base frequency, the 1R mode in hollow engines and the 1T mode in annular engines, so that above the peak frequency is found at $f = 1.5\times$ 1T.

If this is true, it should be expected that data obtained for the 25 mm RDE with a 5 mm gap and equivalence ratios $2 \leq \phi \leq 3$ would fall approximately in line with the predicted 1T line, as seen in Fig. 4.24.

§4.2.4 25 mm: 7 mm Gap

Alone among the 25 mm CH_4-O_2 results, the 7 mm gap annular configuration did not appear to exhibit an arch at low equivalence ratio. As seen on Fig. 4.49, however, the experimental data for this case is relatively sparse. The data around $\phi = 1$ appear to exhibit a decrease and plateau as seen in the hollow 25 mm case, but more data points are needed to explore the dynamics of the 7 mm gap in particular.

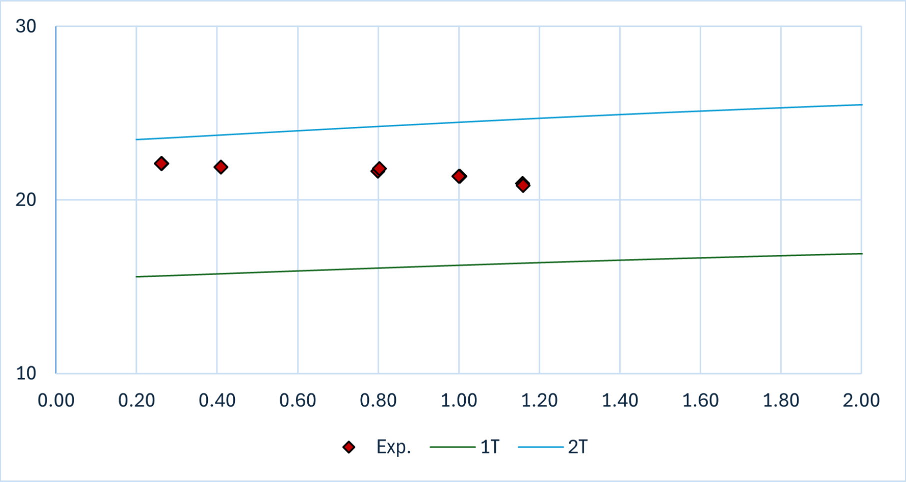

Figure 4.49: 25 mm, 7 mm gap: experimental data vs. predicted tangential modes at $T = 1000$ K, $p = 3$ bar over a range of ϕ.

Note that for this case, no counter-rotating waves were observed over the operating conditions tested. However, that lack, and the fact that the data points hover between the 1T and 2T lines as in the 10 mm hollow CH_4-O_2 case, point to the result that RDEs with wider gap widths behave more like hollow engines than the narrower annuli cases.

§4.2.5 Discussion of Annular Mode Results

As gap width increased, the tangential mode frequencies rose by a small amount, here maybe less than 2% increase per additional 2 mm of gap width increase. However, the predicted radial and mixed transverse mode frequencies dropped substantially, with approximately a 25% decrease in mixed frequencies per 2 mm gap increase, so that the 1T1R, 2T1R, and higher mode frequencies were approximately 50% lower in the 7 mm annulus than in the 3 mm.

For comparison across tangential mode frequencies in both the annular and hollow configurations, Figs. 4.50, 4.51, and 4.52 show the predicted mode frequency behavior in each of the gap widths, across pure tangential modes 1T-13T and transverse modes 1R, 2R, 1T1R. The pure tangential modes remain at approximately the same frequency ranges,

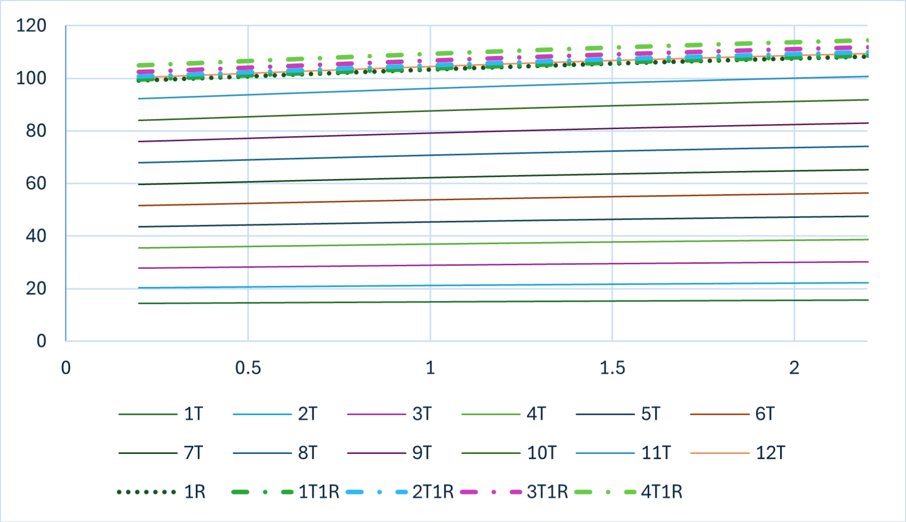

Figure 4.50: 25 mm, 3 mm gap: lowest predicted tangential modes vs. mixed transverse modes at $T = 1000$ K, $p = 3$ bar over a range of ϕ.

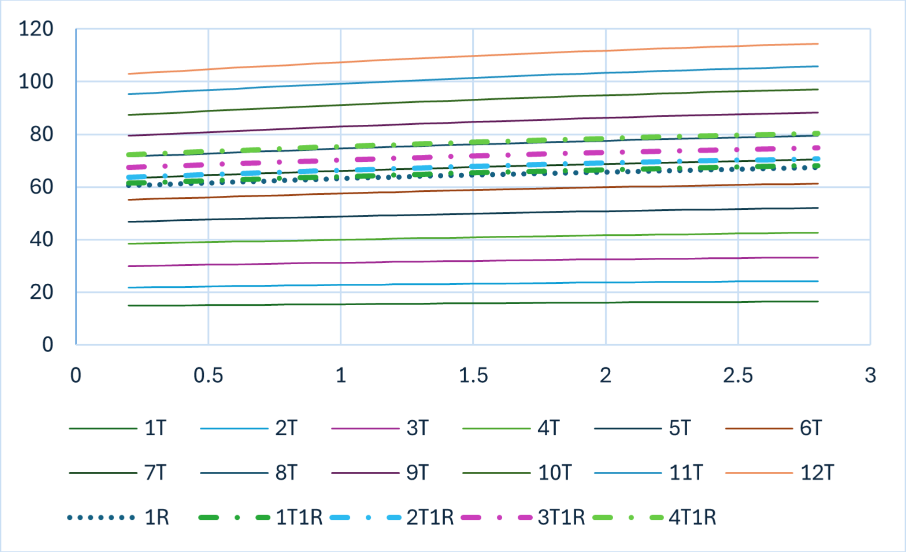

Figure 4.51: 25 mm, 5 mm gap: lowest predicted tangential modes vs. mixed transverse modes at $T = 1000$ K, $p = 3$ bar over a range of ϕ.

while the transverse waves with a radial component (1R, 2R, 1T1R) clearly decrease frequency ranges as gap width increases. Finally, to highlight the drop in radial modes, Fig. 4.53 was created with fixed values of $\phi = 1.15$ and $T = 1000$ K.

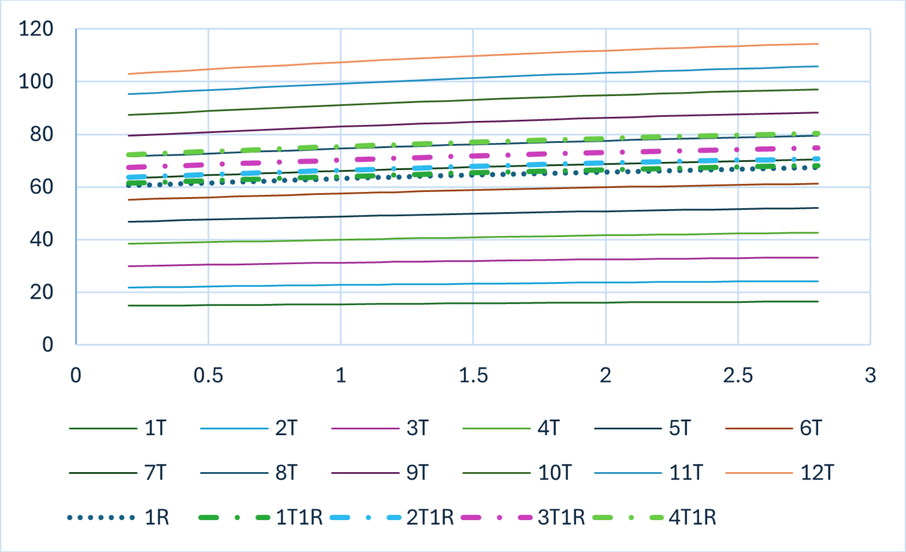

Figure 4.52: 25 mm, 7 mm gap: lowest predicted tangential modes vs. mixed transverse modes at $T = 1000$ K, $p = 3$ bar over a range of ϕ.

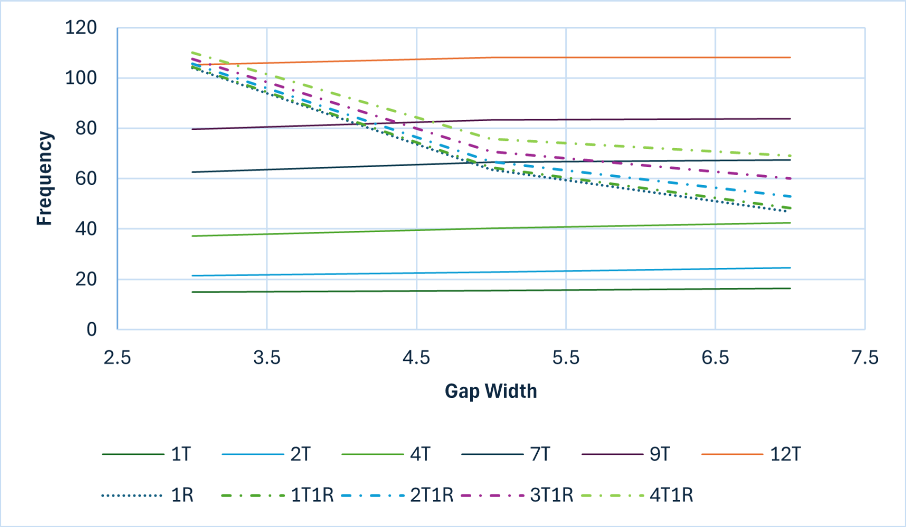

Figure 4.53: 25 mm, annular gap comparison: predicted transverse modes at fixed $\phi = 1.15$ and $T = 1000$ K, over the annular gap widths of 3 mm, 5 mm, and 7 mm.

Chapter 5

Overview and Conclusion

This chapter contains the thesis conclusion, including a summary and discussion of the analysis results. Recommendations for future work are given with concluding remarks in the final section.

Using the method defined in Section §3.2.2, MATLAB scripts were created to compute the acoustic analysis for the annular and hollow configurations separately, while Excel was used to handle and process the analytical and experimental data [8, **?**]. Expected wave spin frequencies were calculated across a range of equivalence ratios and compared with experimental data to validate the frequency results. Simulated engine frequencies (that is, values for f_{mnq}) were obtained per engine size, gap size (for the annular cases), propellant combination, ϕ and the associated reactant propellant sound speed. As noted by Bennewitz et al. in the multi-lab scaling paper, wave count increases with increased mass flux (just as Koch found)[66]. However, it may also increase with fuel-rich conditions, where $\phi \geq 1.15$ [27, 66]. While the data has not yet been normalized for the variances in mass flux, it's possible higher mass flux may be the reason for operating frequencies to increase more slowly than predicted with higher ϕ, causing the mismatch in experimental slope increase over ϕ and predicted velocity-equivalence ratio curve slope.

§5.1 Summary of Findings

The calculated frequencies closely matched the experimental frequency determination for a small range of equivalence ratio, but clearly did not show a strong dependence on ϕ as predicted by the code results. There are three possible hypothesized reasons for the mismatch in the results. The first is that mass flux has not been taken into account at all. For instance, on CH_4 in the 25.4 mm engine at $\phi = 1.15$, mass flux was varied from 75-525 kg/($m^2\cdot$ s), but for mass fluxes greater than 245 kg/($m^2\cdot$ s), the engine appeared to revert to deflagration. The discrepancy in wave speed may simply show that we have not taken into account the varying mass fluxes of the data. However, higher mass flux is primarily associated with changes to and from multiple wave operation (as shown on the charted figures), and has previously not been directly associated with spin speed at varying mass fluxes [66].

The second is that the detonation speeds and frequencies may not be accurate due to miscalculation of the leading shock wave from the recorded imaging data. In particular, H_2-O_2 is a low-luminosity reaction, so the actual shock wave front can be difficult to determine visually. A new method for extracting the operating frequencies from recorded video data is under development, with the help of the undergraduate lab members, that relies on bis-spectral mode decomposition (BMD), to be used in tandem with the FFT post-processing already in use. This method may allow for more accurate wave frequency and spin data collection from the high-speed camera on hydrogen-fuel runs.

Similarly but more importantly, the average wave frequencies are recorded using both piezoelectric sensors and high-speed video; the wave speeds are then calculated from the engine frequencies. However, while the engine frequencies recorded by the camera are within 1% [13] of the corresponding highest frequency recorded in the piezoelectric data, the piezoelectric sensors also captured lower frequencies than could be visibly matched with video data, in the form of pressure-driven power spikes (Sec. §4.1.4 contains more discussion on the processed spectrograms). For example, in one cases with $w = 2$, the low-frequency power fluxes which corresponded to the lower frequencies shown on the spectrogram matched precisely the predicted frequencies for the 1T and 2T modes, even though the highest recorded frequency (from video and sensor data) was above the predicted 2T frequency. This points to an underlying phenomenon, especially in cases of higher mass flux and thus wave counts $w \geq 2$, where the acoustics in RDEs are controlled by the incoming propellant — rather than the detonation wave itself or the detonation wave products — and then contribute to or hinder the steadiness of the detonation wave via integer and fractional multiples of the 0th, 1T, 2T, etc. modes. This hypothesis is not unlike the propellant-wave dependency found by Koch, and clearly explains why the runs that successfully produced detonation wave operation (as opposed to deflagrative or unsteady operation) remain less affected by increasing or decreasing equivalence ratio, since the steady operation would then be achieved only with multiple underlying harmonics that enable steady propagation of the detonation wave despite the inherently unsteady nature of the detonation phenomenon. This would be especially visible in the stable methane compared to the volatile hydrogen.

More research must be done in order to confirm the latter hypothesis. Currently, methods to extract all power spikes (not just the highest one) from a given dataset of runs that successfully produced detonation wave operation and compile them all as engine operating frequencies in the same file have not been developed, making this a time-intensive manual process. However, comparison with the extensive database using all engine operating frequencies would be able to prove or disprove the hypothesis of harmonic operation, given the analysis so far completed by this work.

§5.2 Discussion of Findings

On further research, what was initially mistaken as an unimportant mode and mislabeled was found to be the 1R mode and an integer or fractional multiple of the remaining predicted modes in the hollow RDE configurations. Similarly, in the annular RDEs it was found that the 1T mode, rather than the 1R mode, serves as a multiple of later transverse modes. Since solutions of acoustic modes may be combined in superposition, this effectively means that the 1R and 1T modes, respectively, may act as the fundamental frequencies enabling tangential detonation waves to propagate through RDEs. This would be especially important in the transient detonation wave behavior during the initial start-up sequence of the RDE, since the fundamental frequencies would allow or disallow steady-state detonation wave behavior depending on how well the fundamental frequencies were established at the beginning of the test sequence.

To go into more detail, the empirical experimental evidence shows what appears to be stable operating modes in RDEs with average detonation wave frequencies above the expected values of the resonance modes. However, since the frequency model given by Eqs. 3.20 and 3.21 is well-matched for certain segments of the data, such as the 2-wave case in the 10 mm hollow RDE with H_2-O_2 propellant and the fuel-rich data in the 25 mm hollow RDE with CH_4-O_2 propellant, it is concluded that the model is correct. The natural conclusion is therefore that there exist underlying frequencies that allow stabilization of the RDE at frequencies slightly above the expected values. With this in mind, the data were re-analyzed with the postulation that the 1R mode, which simply states there is a pressure gradient between the center and the outer radius of the hollow RDE, is of more importance than at first glance. If so, the the calculated results would show proof of that relationship.

In hollow engines, the 1R mode was shown to be a harmonic multiplier of the pure tangential as well as mixed transverse modes. This is logical result, because the radial mode in hollow RDEs acts to compress propellant toward the middle of the empty cylinder and rarify the circumference of the combustor. This promotes tangential detonation wave spin around the lower-pressure circumferential region and discourages unburned propellant drifting into the center of the RDE where the detonation waves typically lose strength and revert to less-ideal deflagration.

For annular engines, it was found that unlike for the hollow engines, the 1R mode was not a base multiplier for the pure tangential modes, which is to say it was not important for sustaining detonation wave propagation. However, the 1R mode frequencies were within a small percentage of the 1T1R modes, or in other words, there was no radial mode occurrence in the annular engines without multiples of tangential modes also present in the engine. Hence it is concluded that in annular engines, the 1T mode serves as the "base multiplier" frequency underlying detonation, while in hollow engines, the 1R mode serves the function of the "base multiplier" as a necessary condition of sustaining tangential modes without the benefit of a solid core.

The longitudinal mode was not studied here, although it is an active area of research. Interestingly, it was shown by Sato et al., that for shorter combustors, detonation consistently failed to start due to the higher frequencies required to achieve detonation. Conversely, longer combustors produce detonation waves with operating frequencies that are lower, and thus detonation more easily achievable [49]. Sato's research supports the finding of this work that the combustor characteristics such as length or gap width affect how high the RDE operating frequencies are predicted to be, with shorter combustor lengths, smaller diameters, and smaller gap widths promoting higher frequencies. Additionally, Sato's work points to multiple underlying pressure waves that overlap to encourage steady propagation of detonation waves at harmonic intervals of acoustic pressure wave cycles, just as this work found base multiples underlying the steady-state detonation wave operation.

§5.3 Recommendations for Future Research

The acoustic analysis has implications for RDE performance, since it is as imperative to control the dominant frequency modes in RDEs as it is in turbine engines. However, many of the wide-band passive damping controls used in deflagration engines are not suitable for use in RDEs, due to the RDE's high-frequency temperature and pressure fluctuations as well as the necessity of promoting certain fluctuations to allow the detonation wave to propagate [6]. However, one example of such controls that can be used in RDEs is to ensure smooth flow along the upstream flow lines.

In this analysis, the sound speed a was assumed to be the average across the chamber inlet and exhaust exit, though as Anand and Gutmark noted in their comprehensive review [24], there is likely a considerable radial discrepancy in detonation wave speed between the outer edge of the chamber and the inner edge (for annular) or center (for hollow) of the gap [34, 53, 54]. This discrepancy will result in uneven sound speed across the radius of the engine, so the above analysis cannot be assumed to encompass all relevant physics across the combustor exit, even if it captures the basics of the process. One additional result of interest from these studies [34, 53, 54] is that the radius of curvature has a significant effect on the stability of the detonation wave. For acetylene-oxygen, the critical radius of curvature r_i normalized by detonation cell width λ fell between $14 \leq r_i/\lambda \leq 23$, with the example of $r_i = 20$ mm, $\lambda = 0.71$ mm presented as a typical case [34]. More work on stabilization of detonation waves, including matching a wide range of propellant types to their corresponding optimal radii of curvature, remains to be done.

Realistically, it is quite likely that the wave velocity at the inner wall is nonzero, which is inconsistent with the chosen boundary conditions of $u_{wall} = 0$; similarly, exhaust velocity, which is set to zero for the purposes of this analysis, is nonzero during engine operation. However, to the latter point the purpose of Eqs. 3.20, 3.21, 3.22 is to obtain the cavity natural resonance frequencies at the approximate sound speed of reactant propellant in the RDE. These acoustic frequencies can then be interpreted to gain further understanding of the complex physics boosting or detracting from the operation of RDEs in steady-state. However, the simplified analysis presented here does not account for any acoustically significant divots or cavities (such as instrumentation ports) along the cylindrical cavity space. For a fuller accounting of all the inner cavity details, including wall surface effects not based on the assumption of perfectly smooth, perfectly rigid walls and adiabatic boundaries, the creation of a detailed CAD model in an FEA- or FEM-based modeling software is recommended to continue this work. Such modeling could also investigate implementing an inhomogeneous wave equation rather than the assumed homogeneous equation this work is based upon.

Using simulation software, additional acoustic analysis could be performed to further the work of this study. A range of boundary conditions could be investigated with using a software such as ANSYS, COMSOL [7] or the open-source platform FEniCSx. More accurate 3D acoustical analysis can be used to identify experiment design parameter changes that would increase engine efficiency. For example, calibrating the engine, injectors and mass flux/mass flow rates to promote tangential modes and dampen radial modes in both annular and hollow RDEs is likely to boost specific impulse and thrust production, as in comparative studies of annular vs. hollow performance [14, 68, 87].

Other specific future work could include utilizing instrumentation on hollow RDEs that has previously only been used for annular: see Journell [88] or Athmanathan et al. for unique instrumentation techniques, specifically chemiluminescence and hydroxyl planar laser-induced fluorescence (PLIF) [46, 89] imaging. Alternatively, image processing techniques such as dynamic mode decomposition could be set up following similar techniques as Bohon et al. to reconstruct the full spectrum of active modes and frequencies of operating RDEs from the UW RDE laboratory database of video data [90].

As this and other recent studies discussed in this paper highlight, experimental work continues to make progress in typifying and understanding detonation wave phenomena in RDEs. That said, due to the multitudinous complex interactions within the wave and its components (discussed in more detail in Section §3.2), experimental results are not typically generalizable to future work unless the original experiment design is closely replicated. As an example, Nakayama et al. showed the radius of curvature has a significant effect on the stability of the detonation wave. For acetylene-oxygen in a curved rectangular section, the critical radius of curvature r_i normalized by detonation cell width λ fell between $14 \leq r_i/\lambda \leq 23$, with the example of $r_i = 20$ mm, $\lambda = 0.71$ mm presented as a typical case [34]. The complexities of detonation wave dynamics spell an inability to directly translate these results into models with any one parameter too unlike the experiment conducted above. Nonetheless, it has served as the inspiration for such innovative studies such as that performed by Oda, et al. as they investigated the properties of detonation waves in a curved (hollow) RDE [91]. This study found wave spin frequencies for the 17.5 mm curved RDE run with C_2H_4-O_2 (ethylene-oxygen) to be about 35 kHz, which is within the same range for the $w = 1$ resonance mode as the results computed here for CH_4-O_2 and H_2-O_2.

For another example, Anand and Gutmark noted in their comprehensive review [24] that there is a considerable radial discrepancy between the detonation wave speed at the outer edges of the chamber compared to the inner edge (for annular) or center (for hollow) of the gap [34, 53, 54]. This discrepancy results in uneven sound speed across the radius of the engine at the exit, making accurate calculations of the expected product sound speed a_{CJ} more difficult, as well as producing large areas of subsonic exhaust from the typical assumption of supersonic exhaust produced by the pressure gain cycle inherent in RDEs. Such deviations from the existing simplified theory make it extremely difficult to encompass all relevant physics across the combustor exit. Furthermore, phenomena such as the short list highlighted above exhibit both local interactions as well as nonlinear engine-level coupling [24]. Determining pertinent variable ranges for each RDE configuration, internal flow rate dynamics, and propellant type is prohibitively difficult due to the 3D multi-part nature of detonation waves, while the high temperature and pressure gradients in the combustion chamber severely limit the available instrumentation and data collection options. Ideally, this present work will serve as another step toward fully understanding the interior RDE dynamics and designing future iterations with full cognizance of the many parameters involved.

This discussion highlights the 3D nature of RDEs and the need for better experimental characterization methods within the combustion chamber. Further research on the complex interactions of the multivaried components of detonation waves and the related instability types continues with the help of 3D simulation abilities such as the open source package openFOAM, demonstrated by Rong et al. [11] and others of his colleagues at Peking University [42]. Finally, although the goal is to incorporate RDEs into use cases such as thrust boosters for turbine rocket engines, as noted in Section §2.1, much more work is needed with specific use case conditions in order to achieve that goal.

§5.4 Conclusion

In conclusion, this thesis carried out acoustic analysis of small-scale RDEs with outer diameters of 10 mm and 25, in both hollow and annular configurations. The analysis showed that radial modes are enhanced for wider annular gap widths and hollow engines, whereas thinner annular gap widths promoted tangential modes and counter-rotating waves. The predicted resonance modes and frequencies in small-scale RDEs were compared with recent experimental data and an interesting feature of CH_4-O_2 in the 25 mm RDE was found at low ϕ.

An analysis of the previously unpublished heated fuel data in the 10 mm RDE has been conducted, with the result that although the CH_4-O_2 propellant mixture was previously thought to deflagrate in the unheated case below $\phi < 1.15$ and in the heated case below $\phi < 1.0$, the experimental pressure frequencies validate the presence of detonation waves at a wide range of equivalence ratios as seen in the recorded experimental frequencies.

Finally, recommendations have been given in Sec. §5.3 to further the work of developing RDEs as a practical use technology.

Bibliography

[1] D'Urso, S., "Pratt & Whitney Successfully Tests Rotating Detonation Engine," March 2025.

[2] Hernandez-McCloskey, J., Teasley, T. W., Petty, D. M., Reutlinger, S. A., and Pineda, D. I., "Calorimeter Heat Flux Trends in NASA's Subscale Rotating Detonation Rocket Engine," *AIAA SCITECH 2025 Forum*, American Institute of Aeronautics and Astronautics, Orlando, FL, Jan. 2025.

[3] "NASA Validates Revolutionary Propulsion Design for Deep Space Missions - NASA," Jan. 2023, Section: Marshall Space Flight Center.

[4] "NASA's 3D-printed Rotating Detonation Rocket Engine Test a Success - NASA," Dec. 2023, Running Time: 41 Section: Marshall Space Flight Center.

[5] Goto, K., Matsuoka, K., Matsuyama, K., Kawasaki, A., Watanabe, H., Itouyama, N., Ishihara, K., Buyakofu, V., Noda, T., Kasahara, J., Matsuo, A., Funaki, I., Nakata, D., Uchiumi, M., Habu, H., Takeuchi, S., Arakawa, S., Masuda, J., Maehara, K., Nakao, T., and Yamada, K., "Space Flight Demonstration of Rotating Detonation Engine Using Sounding Rocket S-520-31," *Journal of Spacecraft and Rockets*, Vol. 60, No. 1, Jan. 2023, pp. 273–285.

[6] Pritschau, T., Karnam, A., and Gutmark, E., "Characterizing acoustic modes in a hollow rotating detonation combustor," *Combustion and Flame*, Vol. 275, May 2025, pp. 114057.

[7] "COMSOL Multiphysics®, v. 6.3," 2024, (Windows) COMSOL AB, Stockholm, Sweden www.comsol.com.

[8] "MATLAB Version: 24.2.0.2712019 (R2024b)," 2024, (Windows) The MathWorks, Inc. Natick, Massachusetts, United States https://www.mathworks.com.

[9] "Microsoft Excel," 2018, https://office.microsoft.com/excel.

[10] Braun, J., Sousa, J., and Paniagua, G., "Numerical Assessment of the Convective Heat Transfer in Rotating Detonation Combustors Using a Reduced-Order Model," *Applied Sciences*, Vol. 8, No. 6, May 2018, pp. 893.

[11] Rong, G., Cheng, M., Sheng, Z., Liu, X., and Wang, J., "Investigation of counter-rotating shock wave phenomenon and instability mechanisms of rotating detonation engine with hollow combustor and Laval nozzle," *International Journal of Hydrogen Energy*, Vol. 47, No. 54, June 2022, pp. 23019–23037.

[12] Knowlen, C., Mundt, T., and Kurosaka, M., "Experimental Results for 25-mm and 51-mm RDRE Combustors," *ICDERS*, Napoli, Italy, 2022, p. 6.

[13] Knowlen, C., Mundt, T., Roberts, Q., and Kurosaka, M., "Rotating Detonation Rocket Engine Operation in 10-mm and 25-mm Coreless Combustors," *ICDERS*, Ottowa, Canada, 2025.

[14] Durkee, K. J., Dave, R. T., Maybee, M., Cobb, G. R., Burr, J. R., and Bennewitz, J. W., "Performance Comparison of Variable Center Body Configurations for a 25

mm Rotating Detonation Rocket Engine," *AIAA SCITECH 2025 Forum*, American Institute of Aeronautics and Astronautics, Orlando, FL, Jan. 2025.

[15] Bennewitz, J. W., Bigler, B. R., Hargus, W. A., Danczyk, S. A., and Smith, R. D., "Characterization of Detonation Wave Propagation in a Rotating Detonation Rocket Engine using Direct High-Speed Imaging," *2018 Joint Propulsion Conference*, American Institute of Aeronautics and Astronautics, Cincinnati, Ohio, July 2018.

[16] Schwer, D. A. and Johnson, R. F., "Performance of Centerbody-less Rotating Detonation Combustors for an RDE Concept," *AIAA Propulsion and Energy 2021 Forum*, American Institute of Aeronautics and Astronautics, VIRTUAL EVENT, Aug. 2021.

[17] Bykovskii, F. A., Mitrofanov, V. V., and Vedernikov, E. F., "Continuous detonation combustion of fuel-air mixtures," *Combustion, Explosion, and Shock Waves*, Vol. 33, No. 3, 1997, pp. 10.

[18] Renshaw-Whitman, C., Mi, X., Higgins, A. J., and Kiyanda, C. B., "An Explanatory Model for the Multi-Wave Dynamics in Rotating Detonation Engines," *ICDERS*, Napoli, Italy, 2022, p. 6.

[19] Ye-Tao, S. and Jian-Ping, W., "Three Dimensional Simulation of Rotating Detonation Engine without Inner Wall," *ICDERS*, Irvine, CA, 2011.

[20] Dechert, J. R., Polanka, M. D., Schauer, F. R., Schumaker, S. A., Sell, B., and Fotia, M. L., "Development of a Small Scale Rotating Detonation Engine," *AIAA Scitech 2020 Forum*, American Institute of Aeronautics and Astronautics, Orlando, FL, Jan. 2020.

[21] Mundt, T. J., Chang, L., Ikeda, M., Menn, D., Knowlen, C., and Kurosaka, M., "Annular Gap Width Variation in 25-mm Rotating Detonation Rocket Engine," *AIAA SCITECH 2023 Forum*, American Institute of Aeronautics and Astronautics, National Harbor, MD & Online, Jan. 2023.

[22] Knowlen, C., Mundt, T. J., Roberts, Q., Hamza, A., Menn, D., and Kurosaka, M., "Operating Characteristics of a 10-mm Rotating Detonation Rocket Engine," *AIAA SCITECH 2024 Forum*, American Institute of Aeronautics and Astronautics, Orlando, FL, Jan. 2024.

[23] Zhang, Y., Ma, J. Z., Sheng, Z., Rong, G., Shen, D., Wang, J., and Wu, K., "Experimental research on the Performance of Hollow and Annular Rotating Detonation Engines," *AIAA SCITECH 2023 Forum*, American Institute of Aeronautics and Astronautics, National Harbor, MD & Online, Jan. 2023, ISSN: 2023-1105.

[24] Anand, V. and Gutmark, E., "Rotating detonation combustors and their similarities to rocket instabilities," *Progress in Energy and Combustion Science*, Vol. 73, July 2019, pp. 182–234.

[25] Zeldovich, Y. B., "To the Question of Energy Use of Detonation Combustion," *Journal of Propulsion and Power*, Vol. 22, No. 3, May 2006, pp. 588–592.

[26] NICHOLLS, J. A., WILKINSON, H. R., and MORRISON, R. B., "Intermittent Detonation as a Thrust-Producing Mechanism," *Jet propulsion*, Vol. 27, No. 5, 1957, pp. 534–541.

[27] Bennewitz, J. W., Burr, J. R., Bigler, B. R., Burke, R. F., Lemcherfi, A., Mundt, T., Rezzag, T., Plaehn, E. W., Sosa, J., Walters, I. V., Schumaker, S. A., Ahmed, K. A., Slabaugh, C. D., Knowlen, C., and Hargus, W. A., "Experimental validation of

rotating detonation for rocket propulsion," *Scientific Reports*, Vol. 13, No. 1, Aug. 2023, pp. 14204.

[28] Rathod, D. S. and Meadows, J., "On the Challenges of Integrating a Rotating Detonation Combustor With an Industrial Gas Turbine and Important Design Considerations for Row-1 Blades," *Journal of Engineering for Gas Turbines and Power*, Vol. 146, No. 121009, Aug. 2024.

[29] Heiser, W. H. and Pratt, D. T., "Thermodynamic Cycle Analysis of Pulse Detonation Engines," *Journal of Propulsion and Power*, Vol. 18, No. 1, Jan. 2002, pp. 68–76.

[30] Lu, F. K. and Braun, E. M., "Rotating Detonation Wave Propulsion: Experimental Challenges, Modeling, and Engine Concepts," *Journal of Propulsion and Power*, Vol. 30, No. 5, 2014, pp. 1125–1142, Publisher: American Institute of Aeronautics and Astronautics _eprint: https://doi.org/10.2514/1.B34802.

[31] Blümner, R., *Operating Mode Dynamics in Rotating Detonation Combustors*, Ph.D., Technische Universitaet Berlin (Germany), Germany, 2020, ISBN: 9798522953072.

[32] Harrje, D. T., "Liquid propellant rocket combustion instability," Jan. 1972, NTRS Author Affiliations: NASA Headquarters NTRS Report/Patent Number: NASA-SP-194 NTRS Document ID: 19720026079 NTRS Research Center: Legacy CDMS (CDMS).

[33] Zheng, C. and Taki, S., "Numerical study of the usage of an ignition tube for successful starting of the ram accelerator," *36th AIAA/ASME/SAE/ASEE Joint Propulsion Conference and Exhibit*, American Institute of Aeronautics and Astronautics, Las Vegas,NV, 2000, AIAA 2000-3237.

[34] Nakayama, H., Moriya, T., Kasahara, J., Matsuo, A., and Funaki, I., "Front Shock Behavior of Stable Detonation Waves Propagating Through Rectangular Cross-section Curved Channels," *50th AIAA Aerospace Sciences Meeting including the New Horizons Forum and Aerospace Exposition*, American Institute of Aeronautics and Astronautics, Nashville, Tennessee, Jan. 2012.

[35] Voytsekhovskiy, B. V., "Stationary Detonation. USSR," *Doklady Akademii Nauk USSR*, Vol. 129, No. 6, 1959, pp. 1254–1256.

[36] Bykovskii, F. A., Zhdan, S. A., and Vedernikov, E. F., "Continuous Spin Detonations," *Journal of Propulsion and Power*, Vol. 22, No. 6, 2006, pp. 1204–1216.

[37] Paxson, D. E., "Preliminary Computational Assessment of Disk Rotating Detonation Engine Configurations," *AIAA Scitech 2020 Forum*, American Institute of Aeronautics and Astronautics, Orlando, FL, Jan. 2020.

[38] Batista, A., Kickliter, T., Ross, M., Harvazinski, M. E., and Paulson, E. J., "Computational Study of Chamber Wall Thermal Effects and Heat Flux in a Rotating Detonation Rocket Engine," *AIAA SCITECH 2024 Forum*, American Institute of Aeronautics and Astronautics, Orlando, FL, Jan. 2024.

[39] Stoddard, W., St. George, A. C., Driscoll, R. B., Anand, V., and Gutmark, E. J., "Experimental Validation of Expanded Centerbodiless RDE Design," *54th AIAA Aerospace Sciences Meeting*, American Institute of Aeronautics and Astronautics, San Diego, California, USA, Jan. 2016.

[40] Anand, V., St. George, A. C., and Gutmark, E. J., "Hollow Rotating Detonation Combustor," *54th AIAA Aerospace Sciences Meeting*, American Institute of Aeronautics and Astronautics, San Diego, California, USA, Jan. 2016.

[41] Bennewitz, J. W., Bigler, B. R., Pilgram, J. J., and Hargus, W. A., "MODAL TRANSITIONS IN ROTATING DETONATION ROCKET ENGINES," *International Journal of Energetic Materials and Chemical Propulsion*, Vol. 18, No. 2, 2019, pp. 91–109.

[42] Hou, Y., Cheng, M., Sheng, Z., and Wang, J., "Unsteady conjugate heat transfer simulation of wall heat loads for rotating detonation combustor," *International Journal of Heat and Mass Transfer*, Vol. 221, April 2024, pp. 125081.

[43] Zhang, H., Liu, W., and Liu, S., "Research on H2/Air rotating detonation in the hollow chamber with double injection," *International Journal of Hydrogen Energy*, Vol. 46, No. 44, June 2021, pp. 23067–23074.

[44] Sun, J., Zhou, J., Liu, S., Lin, Z., and Lin, W., "Plume flowfield and propulsive performance analysis of a rotating detonation engine," *Aerospace Science and Technology*, Vol. 81, Oct. 2018, pp. 383–393.

[45] Ishii, K., Kurata, W., Kawana, H., Ohno, K., and Ikema, D., "Effects of Combustor Size on Behavior of Rotating Detonation Waves," *ICDERS*, Beijing, China, 2019, p. 6.

[46] Pike, J., "Nagoya University collaborates with Purdue to unlock the power of rotating detonation engines," 2022.

[47] Sawada, S., Itouyama, N., Matsuoka, K., Kasahara, J., Braun, J., Paniagua, G., Kawasaki, A., Higashino, K., Matsuo, A., and Funaki, I., "Direction Control of Rotating Detonation Waves with Helical Combustion Chambers," *Journal of Propulsion and Power*, Vol. 41, No. 2, March 2025, pp. 164–177.

[48] Sato, T., Nakata, K., Ishihara, K., Itouyama, N., Matsuoka, K., Kasahara, J., Kawasaki, A., Nakata, D., Eguchi, H., Uchiumi, M., Matsuo, A., and Funaki, I., "Combustion Structure of a Cylindrical Rotating Detonation Engine with Liquid Ethanol and Nitrous Oxide," *Combustion and Flame*, Vol. 264, June 2024, pp. 113443.

[49] Sato, T., Nakata, K., Sawada, S., Suzuki, Y., Kudo, Y., Nakajima, K., Itouyama, N., Matsuoka, K., Kasahara, J., Kawasaki, A., Namera, M., Eguchi, H., Nakata, D., Uchiumi, M., Matsuo, A., Funaki, I., and Tanno, H., "Operating Characteristics of Cylindrical Rotating Detonation Engines Using Liquid Ethanol and Liquid Nitrous Oxide," *AIAA SCITECH 2024 Forum*, American Institute of Aeronautics and Astronautics, Orlando, FL, Jan. 2024.

[50] Ishihara, K., Yoneyama, K., Sato, T., Watanabe, H., Itouyama, N., Kawasaki, A., Matsuoka, K., Kasahara, J., Matsuo, A., and Funaki, I., "Visualization and Performance Evaluation of a Liquid-Ethanol Cylindrical Rotating Detonation Combustor," *TRANSACTIONS OF THE JAPAN SOCIETY FOR AERONAUTICAL AND SPACE SCIENCES*, Vol. 66, No. 2, 2023, pp. 46–58.

[51] Liu, S.-J., Huang, S.-Y., Peng, H.-Y., and Yuan, X.-Q., "Characteristics of methane-air continuous rotating detonation wave in hollow chambers with different diameters," *Acta Astronautica*, Vol. 183, June 2021, pp. 1–10.

[52] Xu, H., Wang, F., and Weng, C., "Investigation on H2/O2 rocket rotating detonation engine with annular and hollow combustors," *Aerospace Science and Technology*, Vol. 159, April 2025, pp. 109981.

[53] Nakayama, H., Moriya, T., Kasahara, J., Matsuo, A., Sasamoto, Y., and Funaki, I., "Stable detonation wave propagation in rectangular-cross-section curved channels,"

Combustion and Flame, Vol. 159, No. 2, Feb. 2012, pp. 859–869.

[54] Pan, Z., Fan, B., Zhang, X., Gui, M., and Dong, G., “Wavelet pattern and self-sustained mechanism of gaseous detonation rotating in a coaxial cylinder,” *Combustion and Flame*, Vol. 158, No. 11, Nov. 2011, pp. 2220–2228.

[55] Goto, K., Ota, K., Kawasaki, A., Itouyama, N., Watanabe, H., Matsuoka, K., Kasahara, J., Matsuo, A., Funaki, I., and Kawashima, H., “Cylindrical Rotating Detonation Engine with Propellant Injection Cooling,” *Journal of Propulsion and Power*, Vol. 38, No. 3, May 2022, pp. 410–420.

[56] Heath, J. D., *Generating Detonation Waves in an Annulus via Phased Adiabatic Shocks*, Master’s thesis, University of Washington, Seattle, WA, 2015.

[57] Boening, J. A., Wheeler, E. A., Heath, J. D., Koch, J. V., Mattick, A. T., Breidenthal, R. E., Knowlen, C., and Kurosaka, M., “Rotating Detonation Engine Using a Wave Generator and Controlled Mixing,” *Journal of Propulsion and Power*, Vol. 34, No. 6, Nov. 2018, pp. 1364–1375.

[58] Wheeler, E. A., *Experimental Investigation of Throatless Supersonic Exhaust Velocity in a Rotating Detonation Engine*, Master’s thesis, University of Washington, Seattle, WA, 2017.

[59] Koch, J., *Nonlinear Dynamics of Rotating Detonation Engines*, PhD, University of Washington, Seattle, WA, 2019.

[60] Mendez, D., *Turbulent Methane Oxygen CFD Thermal Effects on Rotating Detonation Engine*, Master’s thesis, University of Washington, Seattle, WA, 2019.

[61] Washington, M., Koch, J., Kurosaka, M., and Knowlen, C., "Radial Injector Mixing Effects on Detonation Zone Position in Rotating Detonation Engine," *AIAA Propulsion and Energy 2019 Forum*, American Institute of Aeronautics and Astronautics, Indianapolis, IN, Aug. 2019.

[62] Mundt, T., *Geometric Scaling of Cylindrical Rotating Detonation Rocket Engine Combustors*, PhD, University of Washington, Seattle, WA, 2023.

[63] Roberts, Q. W., "Investigation of Pre-Ignition Propellant Mixing in Rotating Detonation Rocket Engine," *2023 Regional Student Conferences*, American Institute of Aeronautics and Astronautics, University at Buffalo, Buffalo, New York, United States of America, Jan. 2023.

[64] Hamza, A., *Investigation of an Innovative Injector for Rotating Detonation Rocket Engines*, Master's thesis, University of Washington, Seattle, WA, 2024.

[65] Roberts, Q. and Knowlen, C., "Pre-Ignition Propellant Mixing in Small Scale Rotating Detonation Rocket Engines," *AIAA SCITECH 2024 Forum*, American Institute of Aeronautics and Astronautics, Orlando, FL, Jan. 2024.

[66] Koch, J., *Nonlinear Dynamics of Rotating Detonation Waves*, PhD, University of Washington, Seattle, WA, 2019.

[67] Knowlen, C., Mundt, T., and Kurosaka, M., "Experimental results for 25-mm and 51-mm rotating detonation rocket engine combustors," *Shock Waves*, Vol. 33, No. 3, April 2023, pp. 237–252.

[68] Burr, J. R. and Paulson, E., "Thermodynamic Performance Results for Rotating Detonation Rocket Engine with Distributed Heat Addition using Cantera," *AIAA*

Propulsion and Energy 2021 Forum, American Institute of Aeronautics and Astronautics, VIRTUAL EVENT, Aug. 2021.

[69] Higgins, A., “Steady One-Dimensional Detonations,” *Shock Waves Science and Technology Library, Vol. 6*, edited by F. Zhang, Springer Berlin Heidelberg, Berlin, Heidelberg, 2012, pp. 33–105.

[70] Sasoh, A., *Compressible Fluid Dynamics and Shock Waves*, Springer Singapore, Singapore, 2020.

[71] Crocker, M. J., *Handbook of Acoustics*, John Wiley & Sons, 1997.

[72] Berg, R. R., “Acoustics - Sound Waves, Ultrasound, Vibration,” *Encyclopedia Britannica*, 2019.

[73] Sliphorst, M., *High Frequency Combustion Instabilities of LOx-CH4 Spray Flames in Rocket Engine Combustion Chambers*, PhD, Delft Technical University, Amsterdam, Netherlands, 2011, ISBN: 978-90-5335-384-4.

[74] Wang, H. and Williams, K., “VIBRATIONAL MODES OF THICK CYLINDERS OF FINITE LENGTH,” *Journal of Sound and Vibration*, Vol. 191, No. 5, April 1996, pp. 955–971.

[75] Shimokuri, D., Shiraga, Y., Ishii, K., Toh, H., and Ishizuka, S., “An experimental study on the high frequency oscillatory combustion in tubular flame burners,” *Combustion and Flame*, Vol. 161, No. 8, Aug. 2014, pp. 2025–2037.

[76] Bluemner, R., Gutmark, E. J., Paschereit, C. O., and Bohon, M. D., “Stabilization mechanisms of longitudinal pulsations in rotating detonation combustors,” *Proceedings of the Combustion Institute*, Vol. 38, No. 3, Jan. 2021, pp. 3797–3806.

[77] Barrère, M., *Rocket propulsion*, Elsevier Publishing Company, 1960, tex.lccn: 59008941.

[78] Dowling, A. P. and Stow, S. R., "Acoustic Analysis of Gas Turbine Combustors," *Journal of Propulsion and Power*, Vol. 19, No. 5, Sept. 2003, pp. 751–764.

[79] Kim, J. and Soedel, W., "General formulation of four pole parameters for three-dimensional cavities utilizing modal expansion, with special attention to the annular cylinder," *Journal of Sound and Vibration*, Vol. 129, No. 2, March 1989, pp. 237–254.

[80] Philip M. Morse Ph. D. & Herman Feshbach, P. D., *Methods of Theoretical Physics*, Vol. Part II of *International Series in Pure and Applied Physics*, McGraw-Hill Book Company, Inc., May 1953.

[81] Keller, J. J., "Thermoacoustic oscillations in combustion chambers of gas turbines," *AIAA journal*, Vol. 33, No. 12, 1995, pp. 2280–2287.

[82] Levine, H. and Schwinger, J., "On the Radiation of Sound from an Unflanged Circular Pipe," *Physical Review*, Vol. 73, No. 4, Feb. 1948, pp. 383–406.

[83] Crocker, M. J. and Arenas, G. P., *Engineering Acoustics - Google Books*, Wiley, 2021.

[84] McBride, B. J. and Gordon, S., "Computer Program for Calculation of Complex Chemical Equilibrium Compositions and Applications Part II. Users Manual and Program Description," Tech. Rep. Reference Publication NASA-RP-1311-P2, NASA, Cleveland, Ohio, 1996.

[85] Gordon, S. and McBride, B. J., "Computer Program for Calculation of Complex Chemical Equilibrium Compositions and Applications Part I. Analysis," Tech. Rep. Reference Publication NASA-RP-1311, NASA, Cleveland, Ohio, 1994.

[86] Lemmon, E., Bell, I., Huber, M., and McLinden, M., "{NIST Standard Reference Database 23: Reference Fluid Thermodynamic and Transport Properties-REFPROP, Version 10.0, National Institute of Standards and Technology}," 2018, https://doi.org/10.18434/T4/1502528.

[87] Cobb, G. R., Durkee, K. J., Burr, J. R., and Bennewitz, J. W., "Thermodynamic Power Cycle Analysis in Actively Cooled Rotating Detonation Rocket Engines," *AIAA SCITECH 2025 Forum*, American Institute of Aeronautics and Astronautics, Orlando, FL, Jan. 2025.

[88] Journell, C. L., Gejji, R. M., Walters, I. V., Lemcherfi, A. I., Slabaugh, C. D., and Stout, J. B., "High-Speed Diagnostics in a Natural Gas–Air Rotating Detonation Engine," *Journal of Propulsion and Power*, Vol. 36, No. 4, July 2020, pp. 498–507.

[89] Athmanathan, V., Braun, J., Ayers, Z. M., Fugger, C. A., Webb, A. M., Slipchenko, M. N., Paniagua, G., Roy, S., and Meyer, T. R., "On the effects of reactant stratification and wall curvature in non-premixed rotating detonation combustors," *Combustion and Flame*, Vol. 240, June 2022, pp. 112013.

[90] Bohon, M. D., Orchini, A., Bluemner, R., Paschereit, C. O., and Gutmark, E. J., "Dynamic mode decomposition analysis of rotating detonation waves," *Shock Waves*, Vol. 31, No. 7, Oct. 2021, pp. 637–649.

[91] Oda, Y., Sawada, S., Itouyama, N., Matsuoka, K., Kasahara, J., Kawasaki, A., Matsuo, A., and Funaki, I., "Wave-converging pressure increase in curved cylindrical rotating detonation combustors," *Proceedings of the Combustion Institute*, Vol. 40, No. 1-4, 2024, pp. 105735.